Adsorption Sites of Metal Atoms on MgO Thin Films and Rotational Quantum State Spectroscopy of Adsorbed H$_2$

PAR

Edgar FERNANDES

Um velhote bem me disse algum dia: "Estuda bem, meu filho."
— Joachim Fernandes

Dedicado ao meus pais, Maria-Isabel e Americo, meu mano Rafael,
e minha querida Loeva Thalia Elea.

Remerciements

Pour mener à bien ce travail de thèse, j'ai pu compter sur le soutien, le conseil, l'aide et la présence d'une myriade de personnes, tant sur le plan technique que scientifique, administratif et moral. Je tiens par ces quelques lignes à les remercier le plus chaleureusement.

J'adresse mes premiers remerciements au professeur Harald Brune, m'ayant permis d'effectuer ce travail de thèse au sein de son laboratoire. Le cadre de travail étant idéal pour faire une recherche de qualité.
Je remercie de même le comité d'experts, Martin Sterrer, Mario Rocca et Alfredo Pasquarello pour la critique scientifique de ce travail de thèse, ainsi que le président du jury, Romuald Houdré, qui s'est chargé de superviser, en présence des experts, le déroulement de l'examen oral.

La personne m'ayant le plus apporté durant ce travail de doctorat, et cela sur tous les plans, est sans aucun doute François Patthey qui m'a côtoyé quotidiennement, me guidant dans mes réflexions, m'apprenant les plus subtils détails à propos de la microscopie à effet tunnel, et bien m'a fait part d'une pléthore de qualités humaines. Marina Pivetta a aussi eu une place importante depuis que je la connais. Étant mon mentor pendant mon projet de master, elle a ensuite été d'une présence quasi-quotidienne me permettant de toujours trouver quelqu'un à qui me référer tant sur le plan scientifique que personnel. J'aimerais faire part de ma reconnaissance pour ce qui m'a été apporté par ces deux personnes formidables.
Je voudrais aussi remercier Fabio Donati qui a eu la patience de m'apprendre à mettre en forme le discours scientifique en vue de le partager à la communauté. Il m'a aussi beaucoup appris sur son sujet de prédilection, le magnétisme à l'échelle atomique, sujet sur lequel je n'étais pas entièrement familier.

L'ensemble des collaborateurs et amis restant du Laboratoire des Nanostructures en Surface ont quotidiennement agrémenté mes journées, Darius, Jean-Guillaume, Tobias, Maximilian, Romana, Aparajita, Fabian, Giulia, Quentin, Alberto, Dimitris, Stephan, Wolfgang, Stefano, Ze, Chongqi, Hamed, Simone, Katharina, Luca, Christian et Nicolas. Nous avons toujours pu débattre de sujets non-professionnels lors des pauses café et autres sorties communes.
J'adresse mes chaleureux remerciements à tout le personnel technique et administratif pour leur support absolument essentiel dans certaines tâches quotidiennes, contribuant à rendre la vie facile et agréable. Chantal Roulin ainsi que Carole Pascalon se sont toujours montrées

Résumé

Ce travail de thèse de doctorat se penche sur deux sujets relatifs à la science des surfaces. Nous utiliserons pour cela deux techniques, la microscopie à effet tunnel à balayage ainsi que sa dérivée, la spectroscopie à effet tunnel, toutes deux conduites aux très basses températures (5 K). Pour premier sujet, nous nous intéresserons aux propriétés spectroscopiques de fines couches d'hydrogène (H_2), physisorbées à la surface de substrats métalliques, ainsi qu'à son premier isotope, le deutérium (D_2). Nous serons en mesure de caractériser le premier état d'excitation quantique des modes de rotation du H_2 (D_2) et cela sur une variété de substrats métalliques. L'idée étant de conduire ce type de mesures sur une *unique* molécule, nous chercherons donc à les isoler les unes des autres. Pour cela nous tâcherons de construire de petits îlots de Xe, physisorbés à la surface du substrat métallique, pour ensuite l'exposer au gaz de H_2 (D_2). Dans l'hypothèse où les îlots sont d'aire relativement faible, ils ne pourront accueillir qu'une seule molécule et nous pourrons ainsi effectuer la spectroscopie de manière certaine sur une unique molécule d'hydrogène (deutérium). Dans cette optique nous observerons premièrement l'excitation de leur modes quantiques de rotations sur de larges îlots de Xe, indiquant que l'idée est viable. Toutefois, force est de constater qu'en présence de molécules de H_2 (ou de D_2), les îlots de Xe d'aire susceptible de nous intéresser sont instables, c'est-à-dire qu'il n'est pas possible d'obtenir d'images de l'îlot par microscopie à effet tunnel sans en déplacer les constituants.

Comme second sujet, nous nous pencherons sur la détermination des sites d'adsorption d'éléments métalliques sur une surface d'oxyde de magnésium [MgO(100)]. Cette dernière est construite sous forme de couches minces sur un cristal d'argent Ag(100) par dépôt physique en phase gazeuse. Afin d'identifier les positions de l'atome de magnésium dans les couches de MgO, nous intégrons de très faibles quantités de calcium durant la croissance de la couche, supposé remplacer quelques atomes de Mg dans le réseau ionique. En évaporant ultérieurement des atomes de Ho sur ce substrat, et en comparant leur position à la surface à celle des protubérances dues aux atomes de Ca, nous déterminerons que les atomes de Ho reposent sur deux sites différents. Le premier est sur l'oxygène alors que le second est sur un site *pont*, à mi-chemin entre deux atomes de O (ou de Mg) de la couche de MgO. L'abondance de population de ces deux sites diffère selon l'épaisseur de la couche de MgO. Pour une couche monoatomique, les atomes de Ho sont distribués selon l'abondance des deux sites dans le réseau, c'est-à-dire $1/3$ sur des O et $2/3$ sur des sites ponts. Pour une épaisseur de MgO de deux couches atomiques, les sites O sont presque exclusivement peuplés.

Résumé

Nous nous sommes essayés à manipuler les atomes de Ho avec la pointe du microscope. Par ce biais, il est possible de créer une nouvelle espèce atomique, étant adsorbée sur le site Mg du réseau. Cette possibilité avait correctement été prédite par des calculs théoriques, et ce précédemment à nos essais de manipulations expérimentaux.

Naturellement, nous présentons les sites d'adsorption pour d'autres espèces atomiques. Les atomes de dysprosium, ainsi que d'erbium, s'adsorbent sur des sites O et ponts. Leur abondance est toutefois dépendante de l'épaisseur de la couche de MgO ainsi que de l'espèce métallique. Les atomes d'or peuplent presque exclusivement des sites pont. Le cobalt, ainsi que le fer, s'adsorbent exclusivement sur un site O, et ce indépendamment de l'épaisseur de la couche de MgO, dans les limites mesurées. Finalement les atomes de terbium ont la possibilité de peupler chacun des trois sites atomiques identifiés, c'est-à-dire O, pont et Mg.

Pour troisième et dernier sujet développé, nous montrerons que la température du substrat, pendant l'évaporation du Ho, est un paramètre affectant de manière non-négligeable l'abondance des deux espèces atomiques identifiées à la surface. Par exemple, à la surface de couches biatomiques de MgO, pour une température du substrat supérieure à 30 K, nous n'identifions que des atomes de Ho peuplant le site pont. Cette observation, en opposition complète aux observations d'échantillons préparés à 10 K, est comprise comme l'action d'entropie qui serait capable de changer l'énergie de chacun des sites O et pont. Afin d'expliquer ce changement d'abondance, nous présenterons un modèle thermodynamique, invoquant une source d'entropie. Nous finirons par présenter quelle part d'entropie nous pouvons expliquer, ce qui ne sera toutefois pas suffisant pour expliquer l'observation.

Mots clefs : Microscopie à effet tunnel à balayage, adsorption d'hydrogène, hydrogène moléculaire et isotopes, spin et spin isobarique (isospin), spectroscopie d'états quantiques de rotation, chemisorption et adsorption en surface, site d'adsorption, couches ultraminces, couches d'oxyde de magnésium, diffusion thermique, thermodynamique.

Abstract

The work presented in this thesis covers two different topics of surface science, both investigated with the scanning tunneling miscroscopy and spectroscopy at low temperatures (mostly 5 K). With the first topic, we will be interested in the spectroscopic properties of physisorbed H_2 layers, and of its isotope D_2, on metallic samples. The first rotational quantumstate transition for H_2 (D_2) will be characterized on a variety of metallic substrates. In order to isolate one physisorbed molecule from the surface, we grow Xe islands before to the H_2 (D_2) exposure. Reducing the Xe island size to support only one molecule would allow for probing rotational quantumstate at the individual molecule level. We show that the rotational spectroscopy of H_2 (D_2) on Xe islands is still feasible. We nevertheless also conclude that this method is not viable to isolate a H_2 (D_2) molecule as small Xe islands are unstable in their presence.

The second topic of this thesis deals with the adsorption of metallic atoms on thin MgO(100) films grown on Ag(100) substrate. We use Ca-doping of the MgO layer to identify the Mg lattice positions. Subsequent adsorption of Ho allows the determination of their adsorption site, on top of the O and on the bridge site, halfway between two O (Mg) lattice positions. The abundance of the population over these sites differs with the MgO thickness. On the MgO monolayer, the Ho adatoms are distributed following the abundance of these sites, *i.e.*, $1/3$ and $2/3$, respectively. On the MgO bilayer, almost exclusively O site is populated.

Manipulation of the Ho adatoms permits to create a new species, adsorbing on the Mg site. This was correctly predicted by DFT that ensures that it is the most favorable adsorption configuration for Ho on the MgO monolayer, in agreement with the experiment.

Adsorption sites for others metal atoms have further been measured. Dy and Er adsorb on the bridge and O lattice site, with abundances depending upon the atomic species and the MgO thickness. Au adsorbs almost exclusively on bridge sites. Fe and Co populate uniquely the O site, independently of the MgO thickness, while Tb adsorbs on all the three sites, *i.e.*, O, bridge and Mg.

Abundance of the O and bridge site occupation by Ho adatoms following the substrate temperature during the evaporation, as well as the thermal stability of these against diffusion, were also investigated. We find that the two Ho species are not identically stable against thermal diffusion. The O site becomes unstable for a temperature between 58 K and 77 K, while for the bridge one we had to heat above 125 K. This results by a hopping to the bridge site of all the Ho adatoms adsorbing on O between 58 K and 77 K.

Abstract

Additionally, we show that evaporation of Ho on the MgO bilayer held at 30 K gives rise to adsorption on almost uniquely bridge sites, at total variance to what is found for lower temperature ($\approx$ 10 K). We interpret this result as the action of the entropy which changes the free energy of the two types of adsorption site as the temperature grows. We will approach the problem with a thermodynamical model, which includes an entropic part, needed to explain the observations. Ideas for source of entropy are given, but are still not enough to cover the reported value.

Key words: Low temperature scanning tunneling microscope (LT-STM), hydrogen adsorption, molecular hydrogen and isotopes, spin and isobaric spin (isospin), rotational quantumstate spectroscopy, surface chemisorption and adsorption, adsorption site, ultrathin films, magnesium oxide layers, thermal diffusion, thermodynamics.

Contents

Contents

List of Figures

List of Tables

Introduction

The world of the quantum mechanics is really strange compared to what one experiences everyday. One of the first postulates of the classical physics that does not hold anymore in the quantum world is the *locality* of the physical objects. Indeed, the description of any particle, the electron for example, is made using a wavefunction which provides the *probability density* of finding the particle at some place in the space. Therefore in the picture of quantum mechanics, one uses to say that this electron can be at any spacial location where its wavefunction is non-zero. Nevertheless, the wavefunction follows a strictly deterministic law of motion: it obeys the Schrödinger equation [1].

The tunnel effect is an example of the reality of the quantum mechanics. This effect allows for particles, or small objects that are well described by a wave function, to overcome a potential energy barrier, while in classical mechanics this situation can never be found. Experimental manufacture of a device exhibiting tunnel effect can be achieved with metal-insulator-metal junctions. If the insulator is thin enough, the two metallic electrodes are close enough and the electrons of one electrode can tunnel into the second, and *vice versa*. The presence of a bias between the two electrodes will generate a net tunneling current trough the junction [2]. This kind of effect is a problem for the industry of semiconductors. Indeed, central processing units are based on transistors, whose operational properties rely on their capacity to let electric current flow according to a gate voltage. Miniaturization made the insulating material under the gate electrode very thin and tunneling of the electrons through the insulator to the gate is a problem as it increases the energy consumption of the transistor, and generates calculation errors. But one can also benefit of this physical effect, and researchers have not waited too long to set up experiments actively using the tunnel effect. Indeed, in 1968, Lambe and Jaklevic demonstrated that the vibrational spectra of molecules could be measured in metal-insulator-metal (MIM) junctions, opening a new field for the study of inelastic electron tunneling [2, 3], *i.e.*, the tunneling electrons loose energy *inside* the barrier, where classically their presence is forbidden, by exciting, for example, vibrational mode of impurity molecules. In parallel new techniques appeared to measure at the atomic level the surface of metal substrates: the field ion microscope [4–6]. It consists of a tip electrode, held at a high potential, in region filled with a low partial pressure of He. Gas atoms approaching the tip get ionized and the positive ions get repelled by the important electric field. A phosphor screen permits to image the surface of the tip, as regions of higher intensity correspond to spikes on the tip, where the electric field is much higher than in the surrounding. This kind of instrument

1

allows to image the surface of the tip down to the atomic level and was early used to visualize diffusion of atoms and to determine the adsorption site of strongly bound elements on metal surfaces [4, 7]. Nevertheless, even if the image of the tip is taken in the real space, the experimental results need to be processed to get the real arrangements at the surface of the visualized tip atoms. In addition, this technique provides no information on the surface topography as the result of the experiment is a projected image of the surface.

The *Topografiner* is a sort of mixture of the previous two techniques [8–10]. It consists of a sharp tip, separated from a second electrode, the sample, by a vacuum gap. But, contrary to the MIM systems which were using bias of the order of the Volt, the Topografiner uses voltages up to 300 V, and the tip-sample separation is from the micrometer range to the millimeter one. Providing piezoelectric elements allowing for the tip to move in the three spatial directions, the Topografiner was designed to measure the microtopography at surface of metallic substrates. At that point, the tip was scanned all over the sample with a servo loop adjusting the tip-sample distance in order to maintain the current between the tip and the sample constant. This is where the big difference between MIM and the Topografiner arises: The current flowing through the tip and the sample, across the vacuum space, *is not* a tunneling current. It is an emission current, ruled by the Fowler-Nordheim equation [6, 11]. The Topografiner was an instrument capable of investigating metallic surfaces among multiple orders of lateral and vertical dimensions, but it lacks of the capability to "see" atoms.

A big step in surface science was made possible when Gert Binning and Heinrich Rohrer achieved the setup of the *Scanning Tunneling Microscope* (STM) [12–15]. Their instrument developed, this is later that they got aware of the existence of the Topografiner [16]. Actually the working principle of the STM has much in common with the Topografiner, apart from the fact that STM does not use very thin and sharp tips (which have shown to be mechanically unstable) and that the tip is brought very close to the sample (tip-sample separation is of the order of Ångströms).

Scanning tunneling microscopy opened a new era in surface science physics. Not only topography at the atomic level is possible, but also spectroscopy. This lead to a rapid production of theoretical works [17–23] proposing explanations on how and why this instrument works, reviewed by T. E. Feuchtwang and P. H. Cutler [24]. But the story does not end there as the STM is capable of moving atoms at the atomic level of control [25, 26], used for vibrational spectroscopy on single molecules [27, 28] and able to see the quantum nature of the electrons of a metal [29, 30]. Atomic resolution on substrates and adatoms is very often obtained with the STM, sometimes giving rise to complications in the interpretation because adsorbates on surfaces can appear as depressions in STM images, even though they are topographic protuberances at the surface [31–33]. Side techniques were developed to achieve ultra-high lateral resolution which made possible even to visualize the detail of molecules [34], or also to get magnetic contrast with a spin-polarized tip [35, 36]. Recently the STM was even used to manipulate the spin moment of single Ho atoms [37] and electron paramagnetic resonance was furthermore achieved at the atomic level, on a single atom, with the STM [38]. The STM allows for very large possibilities of investigation in surface science and is therefore an instrument of predilection.

This thesis provides three more examples where the STM is used to get deeper in understanding of adsorbates at surfaces. Chapter 2 will present an investigation where the rotational quantumstates of the H_2 and D_2 molecule is probed with scanning tunneling spectroscopy. We will show that for H_2, or D_2, adsorbed on metal surfaces, the quantumstates of the rotational modes of the molecule are very close, not to say exactly, the ones for the free molecule. The aim of this chapter is to present a tentative way to probe these rotational quantumstates *for one molecule*. This task is challenging because due to the very light mass of H_2, even that of D_2, diffusion of the molecule occurs even for substrates held at 5 K. The idea we will develop is to try to physisorb these H_2 molecules on very small Xe islands which could support ultimately only one H_2 molecule. That would provide the capability to even probe the rotational quantumstates of homoatomic molecules, with unprecedented spatial resolution, with the STM. As we will show, the rotational quantumstates and the nuclear spin configuration are interdependants. This allows, for the STM, to probe the nuclear spin configuration of homonuclear biatomic molecules.

Chapter 3 presents how to determine the adsorption sites of various metal atoms on thin MgO films. For weakly bound species, as it is the case for adsorption of metal species on insulator compared to adsorption on metal substrate, one cannot use the field ion microscope to determine the adsorption site of the adsorbed species. The capability of the STM to resolve even the atoms of the substrate would be indicated for this task. Nevertheless for substrates made of two chemical species as NaCl, MgO, etc... one cannot straightforwardly interpret the atomic contrast. In this chapter we will use Ca doping of the MgO, which acts as markers for the Mg lattice sites of the MgO, to determine the adsorption site of Ho adatoms, and many more metal elements. We will show that the probed transition metal atoms (Fe, Co) adsorb on top of O, that lanthanide elements adsorb mostly on O and bridge site (halfway between two O sites) and that Au adsorbs quite uniquely on bridge site, at variance with what globally reports the actual literature. The method developed here is quite general, thus applicable to a large variety of systems of ionic thin films grown on metal substrates.

Chapter 4 presents the statistics of adsorption of the Ho on O and bridge sites as a function of the deposition temperature. On metal substrates, it is rather accepted that at liquid helium temperature, the mobility of any atom adsorbing on the substrate is zero [39, 40], *i.e.*, the impinging atom adsorbs on the site it falls on. On surfaces of thin insulator films, this picture can change, as we report evidences for transient mobility of Ho adatoms on MgO, still without any ability to quantify it. But it appears that not all the possible adsorption sites are populated for different substrate temperatures during the evaporation of the metal atoms, even more that disappearance of one of the two adsorption sites occurs at much lower temperature than the one at which the Ho adatoms can diffuse on the MgO. We will try to explain the results with a thermodynamical model, from which we will learn that, in this picture, we lack of entropy sources to satisfactorily explain the observations.

1 Scanning Tunneling Miscroscope

The scanning tunneling microscope (STM) allows for imaging the surface of conducting samples, up to the atomic scale. This is an instrument of predilection for surface science, where it has been used for manipulation and probe of single atoms. In this chapter we will rapidly review this experimental technique, used all along this thesis. For more details, the reader is redirected to the textbook of C. Julian Chen [41], or the more recent book of Bert Voigtländer [42] which covers a large field related to the scanning probe techniques, including the STM, from the technical point up to the most theoretical aspects of this technique.

1.1 Principle of Scanning Tunneling Microscopy

Scanning tunneling microscopy is based on a well-known quantum mechanical effect, the tunnel effect. As we go to lower and lower dimension of physical objects, the nature is no longer described by particles, nor waves, but are better described by a probability density wave $\Psi(z)$[1] which provides the probability density of finding an object (proton, electron, ...) in a defined region of the space. This probability wavefunctions obeys the Schrödinger equation [1], which states, for a particle in a potential $U(z)$:

$$-\frac{\hbar^2}{2m}\nabla^2\Psi(z) + U(z)\Psi(z) = \epsilon\Psi(z), \tag{1.1}$$

where m stands for the mass of the particle and ϵ is a value of energy that the system can take. Let us take the example of electron contained in a metallic electrode. The maximum of energy an electron of the metal can have corresponds to the Fermi energy, taken as the energy reference. In the vacuum region, the potential $U(z)$ would be $U(z) = \phi \geq E_F$, with ϕ the work function of the metallic electrode, while in the metallic region we have $U(z) \leq E_F$. Classically, this means that the electrons are trapped in the metal, and cannot in any condition be located in the vacuum region. But in light of quantum mechanics, this image does not hold anymore.

---

[1]We describe here the problem in the form of one-dimensional model for sake of simplicity, although the concepts are extendable to the three-dimensional case.

(a)

Feedback amplifier

Δz-value

Tip

I_t

Sample

V_t

Current amplifier

Preset current

Computer

y-scan

x-scan

(b)

Tip

Height reference

Δz

I_t

V_t

d

Sample

(c)

ϕ_{tip}

Tunnel barrier

ϕ_{sample}

I_t

ϵ

eV_t

Tip

d

Sample

Energy scale
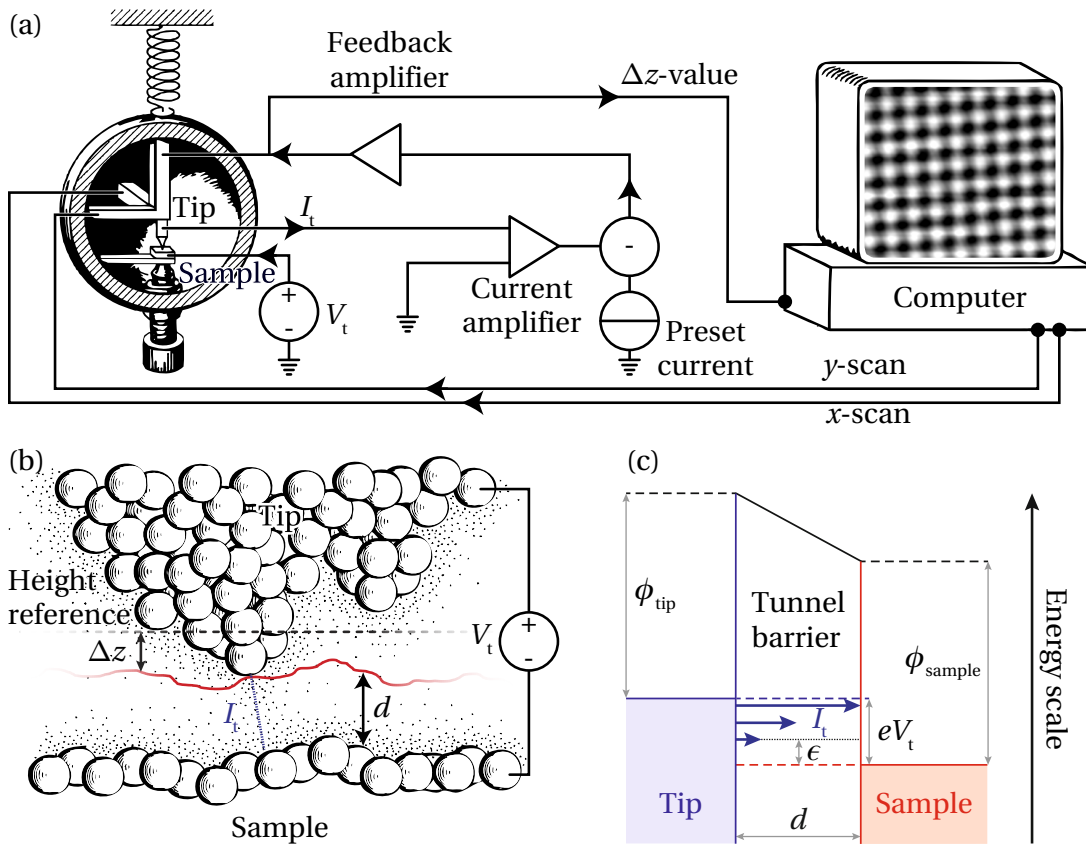
Figure 1.1 – Operational principle of the scanning tunneling microscope. (a) A tip is attached to three piezoelectric units that can move the tip in the three spacial directions. The computer drives the x and y-scan piezos while the z-piezo has its height adjusted to keep the tunnel current I_t equal to the preset value, in presence of the bias V_t. The tip to sample distance is then constant and one reads the signal put on the z-piezo to get the topographic information. Example for the Ag(100) surface is reported on the computer screen. (b) Close up of a realistic tip-surface junction. Due to the exponential dependance of the tunnel current with the tip-sample distance, almost uniquely the apex-atom of the tip will contribute to the tunnel current I_t. (c) Schematics of the energies within the junction. In absence of the bias V_t the Fermi energies of the two electrodes are aligned. The bias pushes downward by the amount eV_t the energy levels of the sample. In this situation, electrons residing in the occupied states of the tip can tunnel into the unoccupied states of the sample. Image (a), (b) and (c) were adapted with permission from [41], [16] and [42], respectively.

The solution to the Schrödinger equation for the step potential holds:

$$\Psi(z) = \Psi(0)e^{\iota k z} \tag{1.2}$$

with k a constant depending only on the electron energy and on the barrier characteristics: $k = \frac{\sqrt{2m(\epsilon - U)}}{\hbar}$. In the metal ($z \leq 0$), k is real and the electron is described by a standing wave with unitary modulus, while in the classically forbidden region ($z > 0$), k is complex and the probability density wave decays exponentially. Physically this means that the farther away we are from the metallic substrate, the smaller the chance to find the electron there, while in the metallic sample we find it anywhere. The exponential constant is given by the factor k directly related to the barrier height ($\epsilon - U$).

Now, by approaching a second metallic electrode (made of the same metal as the first one, to simplify) close to the first one, the evanescent probability density wave $\Psi(z)$ in the vacuum will encounter the second metal interface and the shape of $\Psi(z)$ in the second electrode will be again a plane wave. We interpret that as the following: For very small separation between the two metal plates, an electron belonging to the first metal plate has non-zero probability to be located in the second metal plate. Naturally, the system of concern is symmetric and thus this applies also for the electrons of the second plate which have finite probability to be located in the first plate. This can be seen as two electronic currents, named after *tunneling current*, taking place trough the vacuum region, in both directions with a zero resultant. To get a net tunneling current one could for instance apply an electric bias V_t on one of the two electrodes. This will shift all the electronic energy levels of the electrode where the bias is applied by the value of $-eV_t$ and thus insert an asymmetry in the tunnel junction (see Fig. 1.1(c) for a scheme of the situation).

The tunneling current is directly related to the properties of the vacuum region. For example, in the case of interest and with realistic work functions ϕ for metals, of the order of few electron-Volts[2], the tunneling current follows [11, 12]:

$$I_t \propto \frac{V_t}{\Delta z} e^{-A\sqrt{\phi}d}, \tag{1.3}$$

where the constant $A \sim 1.025 \sqrt{\text{eV}\text{Å}^{-2}}$ and d is the separation between the two metal plates. The tunneling current decreases exponentially with increasing vacuum gap, and is therefore very sensitive to it. Indeed, for each change of d of 1 Å and with realistic values of ϕ, I_t changes by roughly one order of magnitude. The STM takes advantage of this dependence to achieve high microscopy resolution in the vertical dimension.

To get a STM, one needs just one little additional step:

1. Replace the first electrode with the conductive sample and the second one with a metallic tip;

2. Provide possibility to move the tip over the sample with, for example, three piezoelectric units (one for each spacial direction);

---

[2]The electron-Volt, abbreviated eV, is an unit of energy ($1\ \text{eV} = 1.602 \cdot 10^{-19}$ J).

3. Provide a servo-controller that regulates the tunneling current I_t, relatively to a reference, thus regulates the z-piezo extension Δz;

4. Connect the readout of the value Δz to a computer in order to generate a map of the Δz values as a function of the tip position over the sample.

The schematics of a STM instrument is reported in the Fig. 1.1. It consists of a metallic tip that can be brought close to the sample surface [Fig. 1.1(a)]. A set of three piezo scanners allows to move the tip in the three spacial directions, controlled by a computer. We record the extension of the vertical piezo scanner Δz, adjusted to keep I_t constant (constant current mode). The close-up of the tunnel junction is shown in Fig. 1.1(b), indicating that only the atom at the tip apex contributes to the tunnel current. In the operational mode reported, the value d is adjusted to maintain the tunneling current constant. Then, the map of Δz as a function of the (x, y) position of the tip over the sample has something to do with the topography and the electronic structure of the sample. To get a taste of that, one has to invoke theories explaining in more details the way the tunneling current takes place between the tip and the sample. The different theoretical interpretation and explanation of the STM have grown with the development of the technique and have been reviewed by T. E. Feuchtwang and P. H. Cutler [24]. The starting point is to describe the wavefunction of the electrons with a set of base functions named *the orbitals* $\varphi_{i,m}$, (orthogonal within all of them). The total Hamlitonian of the system is assumed to be separable into two components H_1 and H_2, and that the region where the Hamiltonian changes lies somewhere inside the barrier. The Golden Rule expression for the elastic tunneling current holds [24]:

$$
\begin{aligned}
I_t(V_t, T) = \left(\frac{2\pi}{\hbar} 2e \right) \sum_{m,n} \left| M_{(tip,m),(sample,n)} \right|^2 &\left\{ f\left(\epsilon_{(tip,m)} \right) \left[1 - f\left(\epsilon_{(sample,n)} \right) \right] \right. \\
&\left. - \left[1 - f\left(\epsilon_{(tip,m)} \right) \right] f\left(\epsilon_{(sample,n)} \right) \right\} \delta\left(\epsilon_{(tip,m)} - \epsilon_{(sample,n)} + eV_t \right).
\end{aligned}
$$

(1.4)

Here, the energies $\epsilon_{(\cdot,\cdot)}$ are referred to the Fermi energy of the tip, or sample, respectively and the function $f(\cdot)$ holds for the Fermi-Dirac fermionic distribution $f(\epsilon) = \left[1 + \exp\left(\frac{\epsilon}{k_B T} \right) \right]^{-1}$, with k_B the Boltzmann constant and T the temperature of the system. V_t is the bias applied to the tunnel junction, no bias means no net tunneling current. Parts of the physics of the system is carried by the matrix $\left| M_{(tip,m),(sample,n)} \right|$ which describes how the electrons of the tip and the sample are coupled across the tunnel barrier. One of the possible approaches to calculate M is that of Bardeen who expressed the overlap of the wavefunctions for the left and right part of the tunnel junction in the basis of the particle orbitals $\varphi_{i,m}$ [24, 43]. J. Tersoff and D. R. Hamann calculated the matrix element [17, 18] for the specific shape of spherical tip and flat sample. The tunneling current is then expressed as follow [22, 44]:

$$
I_t \propto \int_0^{eV_t} d\epsilon \, \rho_{\text{tip}} \left(\epsilon - eV_t \right) \rho_{\text{sample}} \left(\mathbf{r}_{\text{tip}}; \epsilon \right) \left[f_{\text{tip}} \left(\epsilon - eV_t \right) - f_{\text{sample}} \left(\epsilon \right) \right],
$$

(1.5)

with $\rho_{(\cdot)}(\mathbf{r}, \epsilon)$ describes the density of states of the tip or of the sample, according to the subscript, at the eventual location $\mathbf{r}$ in the space and at the energy ϵ. The tunneling current

is directly related with how the electrons of an occupied state in the tip (case of $V_t > 0$) can tunnel into the unoccupied states of the sample *at the position of the center of the tip apex* $\mathbf{r}_{tip}$. In this picture, the effect of the barrier is not clearly seen. The idea is that the density of states (DOS) of the sample *inside the barrier at the location* $\mathbf{r}_{tip}$ is something related to the DOS of the sample *inside the sample* [22]:

$$\rho_{\text{sample}}\left(\mathbf{r}_{\text{tip}}; E\right) \propto \rho_{\text{sample}}(E) e^{-2d\sqrt{2(\phi-\epsilon)+eV_t}}, \tag{1.6}$$

with d the physical distance separating the tip and the sample. With this formulation we recover the exponential dependance of the tunneling current with the barrier height and the distance to the sample's surface d. In the constant current mode, the vertical information recorded corresponds to the surface of constant integrated DOS between the Fermi energy and the energy eV_t corresponding to the applied bias V_t. For metallic samples, usually the DOS is flat enough, at least around the Fermi level, and thus the quantity d is directly related to the topography of the sample's surface [20, 21, 23]. One has nevertheless to pay attention with this interpretation. STM images of insulating thin layers, or adsorbates, or of anything that has a clearly different DOS function than the supporting metal surface [25, 26, 28–33, 45, see also STM images of chapters 2 and 3] will also have an influence and interpretation of STM images could not be so straightforward. In such a situation the change in tunneling current would not originate from the surface corrugation, but from the local change in the ρ_{sample} quantity. But this is the strongest capability of the STM, accessing topographic and electronic information of the sample with one instrument. One has nevertheless to pay attention sometimes as discrimination between these two facets could raise up some complications. We will confront to some of them in chapter 3.

1.2   Spectroscopy with the STM

We have seen that the tunneling current I_t, for the tip at a distance d from the sample's surface, is directly related to to the density of states of the sample. Thus, the STM should have capabilities to investigate the local density of states. Assuming a constant density of states of the tip ρ_{tip}, and small bias voltages V_t, we can establish [46]:

$$\frac{\mathrm{d}I_t}{\mathrm{d}V_t} \propto \rho_{\text{tip}} \rho_{\text{sample}}(eV_t). \tag{1.7}$$

This is clearly one motivation to conduct spectroscopic measurements with the STM, one can have the possibility (at least in ideal cases) to access locally to the DOS of the sample. One had not to wait until the appearance of the STM to use tunneling spectroscopy. Vibrational spectroscopy of molecules were already conducted in the past in metal-vacuum-metal junctions [2, 3]. What the STM additionally provides is the locality of this kind of measurement. Scanning tunneling spectroscopy (STS) is thus able to perform for example vibrational spectroscopy on individual molecules [28, 47], spin excitation of individual magnetic moments [48], rotational spectroscopy of light molecules [49, 50], and this list is clearly not exhaustive. STS

somewhat measures the conductance of the tunnel junction. Thus any physical process that induce a change in the conductance of the tunnel junction can in principle be measured. Usually the tunnel current I_t is very noisy, thus the numerical computation of the derivative $\mathrm{d}I_t/\mathrm{d}V_t$ is very inefficient. The better would be to have the possibility to access directly this quantity with the experiment. The lock-In measurement technique permits to make it feasible.

1.2.1 The Lock-In technique

The Lock-In technique allows the user to measure small signals in a noisy environment. This is made possible through adding to the signal of interest a small modulation of well-known and temporally stable frequency [42]. Thus for the STS one would add a small modulation, with amplitude V_{mod} and pulsation ω_{mod}, to the bias voltage with frequency high enough insuring that the STM tip-piezo will not respond to this modulation (when the feedback is active). To see how to recover the DOS, we decompose the tunnel current in a Taylor series [46]:

$$
I_t = \underbrace{\int_0^{eV_t} \rho_{\mathrm{sample}}(E)\mathrm{d}E}_{\propto I_t} + \underbrace{\rho_{\mathrm{sample}}(eV_t)\,eV_{\mathrm{mod}}\sin(\omega_{\mathrm{mod}}t)}_{\propto \frac{\mathrm{d}I_t}{\mathrm{d}V_t}}
$$
$$
+ \underbrace{\frac{\mathrm{d}\rho_{\mathrm{sample}}(eV_t)}{\mathrm{d}V_t}}_{\frac{\mathrm{d}^2 I_t}{\mathrm{d}V_t^2}} \frac{(eV_{\mathrm{mod}})^2}{2}\sin^2(\omega_{\mathrm{mod}}t) + \dots
$$

Now, if we multiply the current I_t with a sine function with pulsation ω_{mod}, all the terms in the Taylor expansion will be zero in average apart of the term oscillating at pulsation ω_{mod}. The level of the resulting DC signal is proportional to the first derivative of the tunneling current, *i.e.*, the differential conductance $\mathrm{d}I_t/\mathrm{d}V_t$. The advantage with this technique is that we can access higher derivatives of the current. For example, one will multiply the modulated signal with the first harmonic of the fundamental modulation to get the second derivative of the tunneling current.
In the following we will present the two mostly used spectroscopic modes.

1.2.2 dI/dV spectroscopy with regulation feedback inactive

The first STS mode, mostly referred as $\mathrm{d}I/\mathrm{d}V$ in the following, is made with the feedback loop open (inactive). Instructions are:

- Place the STM tip above the region to perform the spectroscopic measurement;

- Open the feedback loop and superimpose the modulation signal to the STM bias;

- Ramp the bias between the two bias voltage on interest;

- At the end of the bias ramp, close the feedback and the scanning measurements can start again.

With this mode we will take all the spectra of the chapter 2. We will be able to identify the rotational mode of H_2 and D_2 molecules adsorbing on various substrates due to the characteristic of the spectra. If the change in conductance appears at symmetric bias around $V_t = 0$ V, then the process probed is independent of the polarity of the junction. Such processes have chances to be excitations of the sample. In this case the excitation process can be described following the ideas of the references [2, 3]. The excitation opens a new channel to tunnel through. The electron tunneling process is inelastic because the electron will loose energy in the barrier. This is evidenced by an increase of the differential conductance. Note that in some situations, the excitation effect in the conductance can take much complex shapes, as reported in [51, 52].

1.2.3 dI/dV spectroscopy with regulation feedback active

The second mode used for STS, usually referred as field emission resonance (FER) spectroscopy, is operated with the feedback loop closed (active). We use it, in this thesis, to discriminate between different layer thicknesses of insulating material grown on a metal substrate. For that we:

- Place the STM tip above the region of interest;

- Ramp the bias between the two voltages of interest;

- Recover the measurement of the sample.

With this mode, the feedback loop is still active. Thus the bias ramp cannot pass through null bias otherwise we crash the tip on the sample (and thus on the region of interest). Indeed, the tip-sample separation is adjusted according to the setpoint current, and if I_t is zero, then the value d is also zero.
FER spectroscopy permits to have access to Coulombian electronic states inside the barrier. These permits to get information on the surface states and work function of the sample [53, 54]. In the normal operation, one does not need to have the real values of these quantities, FER spectroscopy is generally used, at least in this thesis, to discriminate different regions of the substrate. Indeed, the energy location of these field emission resonance will be a function of the local work function of the substrate. Thus changes in the FER spectra can be traced back to changes in ϕ.

1.3 Conclusion

The techniques that will be used for the studies presented in the chapters 2, 3 and 4 is the scanning tunneling microscopy and spectroscopy. It gives access to the electronic structure of the sample and also for atomically resolved images of the surface, whose topography can usually be interpreted. Spectroscopy using the STM permits to investigate inelastic processes

taking place in the junction. This will be extensively used to study the rotational quantum state of H_2 and D_2 molecules adsorbed on metallic substrates.

The versatility of the STM allows for multiple improvements. For example one can use magnetic tips, and have a magnetic contrast of the surface. By using spin-polarized currents one could investigate the magnetic moment orientation of single atoms adsorbed on surfaces [35, 36]. More recently electron paramagnetic resonance was achieved with the STM [37,38], allowing for unprecedented energy resolution *and* less disturbance of the sample during the measurement.

No doubt that the scanning tunneling microscopy is an instrument of choice for the field of surface science.

2 Physisorbed hydrogen and deuterium on metal substrates

This chapter summarizes results obtained on the study of H_2 and D_2 on metallic surfaces. We start by giving a taste of how extended is the experimental and theoretical knowledge of systems dealing with molecular hydrogen or deuterium molecules, and its implication in everyday life and astrophysics. We follow with the state-of-the-art knowledge of physisorbed H_2 and D_2 on metallic surfaces, as well as on samples of a monolayer of graphene or hexagonal-BN grown on metallic substrates. Focus will be given to studies using scanning tunneling microscopy.

2.1 Introduction

The hydrogen molecule, simple as it is, has a big importance in many fields such as astrophysics, energy storage and also for surface physics fundamental research. The major part of the Universe is hydrogen, we find it in the stars but also between the stars in the interstellar gas. On Earth it has some technological importance as it is used as fuel, for example, for space shuttles, but also for mobility such in fuel cells. Nevertheless, transport of hydrogen in the liquid form encounters a huge problem, the ortho- to para- conversion catalysis, that can be understood only in the light of quantum mechanics.

In the beginning of 20th century there were some problems in explaining the experimental data, obtained by Eucken in 1912, con cerning the rotational specific heat for molecular hydrogen, see Fig. 2.1. The available models describing the specific heat were the Planck-Einstein [56] and the Nernst-Lindemann [55] ones, and were not able to describe the rotational specific heat of hydrogen, see the two model curves in Fig. 2.1. From elementary physics, we learn that each degree of freedom provides $1/2R$ [61] to the specific heat of a compound and, at sufficiently high temperatures, rotations of diatomic molecules (modeled as a rigid rotor) contribute to a total value of $1R$ to the specific heat, for 3D rotations. At low temperature the experiment shows that the rotational specific heat tends to zero and this is well explained by the quantum theory. Nevertheless some discrepancies arise when one tries to explain the rotational specific heat for temperatures between these two limiting cases, see again the Fig. 2.1. The problem
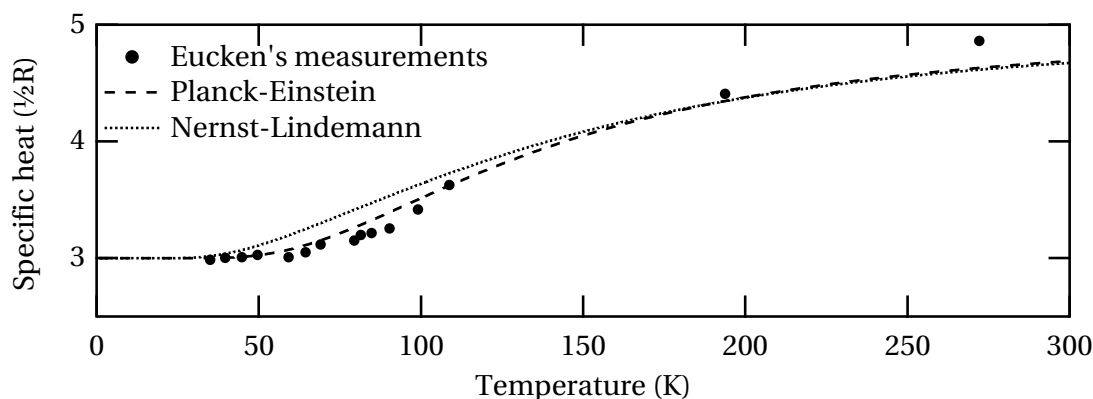
Figure 2.1 – Contribution of the rotational modes to the total specific heat of the hydrogen. Nernst-Lindemann curve formula is given in reference [55]. Figure adapted from reference [56], retrieved from Biodiversity Heritage Library [57].
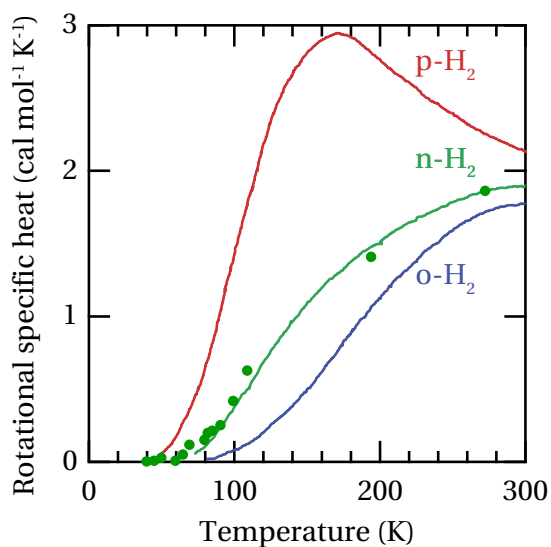
Figure 2.2 – Rotational specific heat for o-H_2 (blue) and p-H_2 (red) as a function of the absolute temperature. Round markers (n-H_2) are the rotational specific heat measurements done by Eucken, extracted from [56], and the green curve corresponds to the result of Denninson's model [58, 59]. Adapted with permission from [60].

was solved, to some extent, by David M. Dennison when he assumed that hydrogen could be described with two components, called H_2 modifications [58, 59], hereafter referred to ortho-H_2 (o-H_2) and para-H_2 (p-H_2). The change he introduced was twofold. He described the hydrogen molecule with an associated rotational wavefunction which can be symmetric (even J) or antisymmetric (odd J), with J the quantum number representing the rotational mode. In addition, he assumed that the transition between symmetric and antisymmetric rotational states of the molecule is very slow such that the hydrogen could be described as composed by two different gases, *i.e.*, modifications of J values can only occur between even (or odd) ones. His conclusions were that if there were three times more molecules with anti-symmetric rotational state in comparison to the symmetric counterpart, then he could explain the experimental results. For each hydrogen modification, he could calculate the associated specific heat, reported on the Fig. 2.2.

These conclusions have a huge impact from the physical point of view, because quantum mechanics links the rotational wavefunction with the nuclei one and constraining the rotational wavefunction to symmetric or antisymmetric one will also imply the symmetry of the nuclei wavefunction. This can be used to get insight into the isospin configuration of the nuclei.

In the light of modern quantum mechanics, we describe the hydrogen (and the deuterium) molecule using a wavefunction composed of four parts:

- Ψ_e, describing the two electrons of the molecule;

- Ψ_{rot}, describing the rotational quantum state of the two nuclei;

- Ψ_{Ispin}, describing the isospin configuration of the two nuclei;

- Ψ_{vib}, describing the vibration of the two nuclei with respect to each other.

We apply the Pauli principle twice: one to the electronic wavefunction Ψ_e, and one for the nuclear wavefunction $\Psi_{nuclear} = \Psi_{rot}\Psi_{Ispin}\Psi_{vib}$. For the H_2 (D_2) molecule, the electronic part is always antisymmetric with respect to the exchange of the two electrons [62, 63]. Concerning the nuclear part, it has to be antisymmetric (symmetric) with respect to the exchange of the two nuclei of H_2 (D_2). Indeed, the nuclei of a H_2 molecule is made of two protons, each fermions, while the nuclei of D_2 is composed by two deuteron[1], a boson. From these considerations, we can explicit all the configurations of the symmetry the different components of $\Psi_{nuclear}$ can assume with respect to the antisymmetry of $\Psi_{nuclear}$, and we report them in Tab. 2.1.

We learn from Tab. 2.1 that if the symmetry of Ψ_{rot} is 1, then the isospin of the two nuclei of the H_2 molecule must be anti-aligned, thus associated with a -1 symmetry of Ψ_{Ispin}, which defines the p-H_2 modification for H_2. Similar conclusions permit to identify the o-H_2, p-D_2 and o-D_2 molecular modifications. The description of the Ψ_{Ispin} wavefunction will then be a function of the total nuclear spin. For the H_2 molecule, the total nuclear isospin I can be

---

[1]The deuteron is the nuclei of the deuterium atom, first isotope of the hydrogen. It is formed by the assembly of one proton with one neutron.

	Ψ_{rot}	Ψ_{Ispin}	Ψ_{vib}	Total (Ψ_{nuclear})	Name
H_2	−1	1	1	−1	o-H_2
	1	−1	1	−1	p-H_2
D_2	1	1	1	1	p-D_2
	−1	−1	1	1	o-D_2

Table 2.1 – Symmetry (±1) of the different parts of the nuclear wave function Ψ_{nuclear} with respect to the exchange of the two nuclei of the molecule. The symmetry Ψ_{rot} and Ψ_{Ispin} are interdependent in order to satisfy the symmetry of Ψ_{nuclear}.

described as the combination of two spin $1/2$ from the protons, then $I = 1$ or 0. The former give rise to a triplet configuration of the nuclei whose isospins are aligned, and thus with $\Psi_{\text{Ispin}}^{H_2}$ symmetric (o-H_2), while the latter produces a singlet with anti-aligned nuclear spins and $\Psi_{\text{Ispin}}^{H_2}$ is antisymmetric (p-H_2). The same considerations hold for D_2. Each nuclei of the D_2 molecule possesses a spin 1. Combination of these two spins can be described by a total spin associated to the nuclei of $I = 2, 1$ or 0. For even I, we have $\Psi_{\text{Ispin}}^{D_2}$ symmetric (p-D_2) and for odd I, $\Psi_{\text{Ispin}}^{D_2}$ is antisymmetric (o-D_2).

From the experimental observations, and as assumed by Dennison [58, 59], the transition between para- and ortho- modifications of H_2 or D_2 is negligible and then normal hydrogen (n-H_2) is composed by a p-H_2 and an o-H_2 fraction in standard conditions. Each of the hydrogen modifications do not exhibit identical rotational spectrum; even rotational numbers J are always associated with the p-H_2 where odd J are strictly connected with o-H_2. This remark provides a direct way to test the nuclear spin configuration of the molecule only by looking at its rotational spectra. Indeed, the energies of rotation for a rigid rotor are described by $E_{\text{rot}} = BJ(J+1)$, where $B = \dfrac{\hbar^2}{2\mathscr{I}}$ is the rotational constant of the considered molecule, with $B = 7.36$ meV and 3.71 meV for H_2 and D_2, respectively [60]. Note that B only depends on the mass and the geometry of the molecule, as it inversely proportional to the moment of inertia $\mathscr{I}$ of the molecule.

The rotational energies E_{rot} associated with the rotational quantum number J are reported in Fig. 2.3 for both H_2 and D_2. Energies associated with the D_2 molecule are half of the values for H_2, due to the inverse linear scaling of B with the mass (included in the moment of inertia).

We have seen that the H_2 gas, as well as the D_2 one, has to be described as a mixture of two independent gases each with some particularities: The p-H_2 has a singlet nuclear configuration and is associated with even J values of the rotational quantum number. The counterpart associated with the triplet nuclear configuration, the o-H_2, has odd J values. The conversion between the para- and the ortho- modifications of hydrogen requires a realignment of the nuclear spins. But, in the gas phase, coupling of the nuclear spins with the electrons is so small that no conversion is observed [62]. Therefore, when cooling normal hydrogen down to cryogenic temperatures, the o-H_2 stays in a rotational excited quantumstate of the

E_{rot} (meV)

$J = 3$ 87.4
      (44.3)

72.7
(36.9)

43.9 $J = 2$
(22.2)

14.7
$J = 1$ (7.4)

0     $J = 0$
(0)   para-H$_2$ ortho-H$_2$
      (ortho-D$_2$)   (para-D$_2$)

Figure 2.3 – Rotational energies E_{rot} of a 3D rotor as a function of the rotational quantum number J for the H$_2$ and D$_2$ molecules. The zero energy is taken for $J = 0$. In blue are given the energies for the first rotational excitation of o-H$_2$ and p-D$_2$. Adapted with permission from reference [62].

molecule with $J = 1$, and when a molecule undergoes the ortho-para conversion, an energy of 14.7 meV is released, enough for evaporating the H$_2$ [63]. Transport of hydrogen at cryogenics temperatures needs prior otho-para conversion which can be done with a catalyst. Metallic surfaces have proven to be good catalysts for the o-H$_2$ to p-H$_2$ conversion. Processes proposed for that deal with the action of magnetic impurities and are described in references [62, 63]. Nevertheless some experiments were able to detect the signature of rotational excitations of p-H$_2$ and o-H$_2$ on metallic surfaces [64–67].

2.2 State of the art on surface-physisorbed molecular hydrogen

Surface-physisorbed molecular hydrogen (or deuterium) was investigated with many techniques, namely low energy electron diffraction (LEED), neutron diffraction (ND), high resolution electron energy loss spectroscopy (HREELS), thermal desorption (TD) and scanning tunneling microscopy. These studies are summarized in Tab. 2.2. All the studies using HREELS reported the existence of rotational quantumstate excitations of the physisorbed adlayer showing that surface-physisorbed H$_2$, HD or D$_2$ behaves as a 3D free rotor, *i.e.*, the energies measured correspond to the theoretical ones for the gas phase of the probed molecule. At variance, with the STM, rotational excitation of the molecular adlayer is reported for h-BN or graphene monolayer grown on a metal substrate [68, 69]. Except for H$_2$ (HD and D$_2$) physisorbed on Au(110) substrate [49], on any other of the investigated metal substrates [Cu(111), Ag(111), Ag(100), Au(111)] were rotational excitations for the hydrogen molecule reported. Therefore, the current literature better testifies that rotational excitation of H$_2$ with the STM is quite exceptional, where with HREELS that was common. To observe the rotational modes with the STM, Natterer *et al.* used a decoupling layer of graphene (g) or hexagonal boron-nitride (h-BN) [68, 69].

	TD	LEED	ND	HREELS	STM
Metallic surfaces	[70]			[64, 65] [66, 67]	[49, 52] [34, 71, 72]
Graphene or h-BN		[73]	[74, 75]	[76]	[68, 69]

Table 2.2 – Survey of the literature reporting surface-physisorbed H_2, HD or D_2 on two kind of substrates: bare metal surfaces and graphene or h-BN grown on metal surface.

2.2.1 Motivation

Our motivation for studying the systems of physisorbed H_2 (or D_2) layers is twofold. On the metallic substrates it seems that the rotational excitation signal for physisorbed H_2 (D_2) is absent, or at least sufficiently weak to be missed in individual STS spectra. The insertion of a decoupling layer like g or h-BN [68, 69] allows to considerably increase the signal of the rotational signature, but the systems proposed do not allow single molecule probing. Indeed, as reported by Natterer *et al.* [68], it seems that the rotational spectra is the result of multiple molecules excitation (60 ± 30 objects) and not from an unique H_2 (or D_2) molecule. We are therefore interested in the question whether one could probe the rotational excitations of a single molecule. Indeed, if yes, one could use STS as a very local probe capable of identifying every single physisorbed molecule as p- or o-H_2, thus achieving unprecedented spatial resolution in distinguishing molecular objects identical from the chemical point of view. All the concepts presented are valid for diatomic homonuclear molecules, thus in principle this opens a route to investigate the isospin configuration of such surface-physisorbed molecules. The idea to possibly answer this question deals with the use of a noble-gas decoupling layer on metal substrates. We used Xe, but Ne, Kr or Ar could also be used alternatively. The idea is the following: as the decoupling layer facilitates the observation of the rotational excitations of the physisorbed molecule, then using the Xe gas permit to tune the lateral size of the physisorbed islands. By varying the exposition time of the sample to the Xe gas, one can create islands whose size can range from the single Xe-atom to a complete Xe layer physisorbed on the metal surface. To probe the rotational excitation of less and less H_2 (D_2) molecules, one has just to decrease the island size down to the one that would hold one unique H_2 molecule on it. Naturally, this is an hypothesis and experiments should be carried out to test the idea.
Many combinations of systems were tried, but we present here a logical ensemble of measurement that are strong enough to exhibit the rotational excitation of the H_2 and D_2 molecules. We show that rotational excitations can be probed with the STM on a variety of metal substrates, thus suggesting that it is rather a general feature. We also discuss why the literature failed in observing that previously.

Results are presented as follow. We will first describe the physisorption of hydrogen on metallic substrates. When these systems are characterized, we present the results where we include

	Ar^+ sputtering	Annealing
Ag(100)		
Ag(111)	500 eV, 10 µA/cm^2	800 K
Cu(100)		
Ni(111)	1500 eV, 10 µA/cm^2	1100 K

Table 2.3 – Conditions used during the cleaning of the metallic samples prior to exposure to Xe, H_2 or D_2 gases.

the intermediate Xe decoupling layer. Next we move to results for D_2 physisorbed on metal surfaces and finally for D_2/Xe/metal systems. An overall discussion concludes this chapter.

2.3 Experimental results for H_2 physisorbed on metal substrates and on Xe islands

We present here the results for H_2 and D_2 physisorbed on metallic substrates, as well as on metal-supported Xe islands. As we are interested on the rotational spectroscopy of each molecule's modification (o- and p-H_2 and D_2), accent will be put on the spectra taken for each presented system. Rotational excitations are clearly observed on various metal substrates. Effectiveness of the action of Xe as a decoupling layer is more debatable.

The metal substrates were prepared with cycles of Ar^+ sputtering with subsequent annealing, using the parameters reported in Tab. 2.3. After that, the sample is transferred in the cold (T_{STM} = 5 K) STM and let cool down for a night. Xe and H_2 (D_2) were physisorbed on the substrate by exposing the sample to a partial pressure of the gas of interest. For that we filled the STM chamber with the gas ($p = 10^{-7}$ to 10^{-6} mbar) and the STM doors were open. The physisorption of the gas occurs readily with the sample at an approximate temperature of 10 K, sufficiently low for the hydrogen (deuterium) to stick on it. The dose of gas is measured in unit of Langmir (L), with 1 L corresponding to a gas exposure of one second under a partial pressure of 10^{-6} mbar.

2.3.1   Physisorption of H_2 on metal substrates

Physisorption of H_2 on Ag(100)

Physisorption of molecular hydrogen on the surface of the Ag(100) crystal is reported in Fig. 2.4(a). The molecular resolution on the physisorbed layer reveals the moiré pattern originating from the mismatch between the square lattice of the substrate and the hexagonal lattice of the H_2 layer. The black depressions are attributed to defects on the bare Ag(100) substrate as the longer objects seem to be oriented along two perpendicular directions, in agreement with the two equivalent [100] directions of the Ag(100) substrate. Fast Fourier transform (FFT)

of the STM image in Fig. 2.4(a) is shown in the inset, with the six spots clearly confirming the hexagonal symmetry of the physisorbed H_2 layer.

The lattice parameter of the H_2 layer is extracted from the autocorrelation image shown in Fig. 2.4(b). The mean spacing between the protrusions of Fig. 2.4(b) along the three directions depicted with the solid and two dashed lines yields a lattice parameter of 3.59 ± 0.09 Å, in quantitative agreement with the value of 3.40 Å for intermolecular separation for solid molecular hydrogen. Following the conclusions of Brunet *et al.* [77], the lattice constant of a physisorbed layer can vary a lot depending on how strong the intermolecular or the van der Waals interaction with the surface are. In addition, this intemolecular distance can also vary with the gas coverage. Such analysis were not conducted as the point of main interest was put on the spectroscopy of the molecules forming the adlayer. Note that the experiments have shown that in order to be able to image the individual molecules forming the adlayer, one has to create compact molecular adlayer which would prevent the molecules to move on the metal surface. This is done by controlling the gas exposure. If too little H_2 or D_2 gas is physisorbed at the metal surface, the individual molecules are free to diffuse and then this is impossible to image any molecular adlayer.

The differential conductance curve $\mathrm{d}I/\mathrm{d}V$ recorded on the H_2 adlayer is reported in Fig. 2.4(c). The data shown is the result of an average over 700 individual spectra. The errorbar for each recorded datapoint is not reported for clarity, but in average the error value for bias between -0.05 V and 0.05 V is of the order of ± 0.002, thus relatively small compared to the features observed in the data. Indeed, each spectra is recorded with a relatively high noise in comparison to the feature of interest. Averaging over many individual spectra (let say N) permits to recover, in average, the STS signal. The associated error on the mean spectra at a specific bias is $1/\sqrt{N}$ of the dispersion of the data points around the mean spectrum at the same bias.

In order to evaluate the bias at which the conductance undergoes an abrupt change, we numerically derive the $\mathrm{d}I/\mathrm{d}V$ data using the central differences algorithm, see the black points of Fig. 2.4(d). Prior to the fitting of the $\mathrm{d}^2I/\mathrm{d}V^2$ data, smoothing is applied in order to increase the numerical stability of the fit. Using an antisymmetric function around zero bias and gaussian shapes for the peaks, we obtain the red curve fit to the $\mathrm{d}^2I/\mathrm{d}V^2$ data in Fig. 2.4(d). Further integration of this fit curve is reported as the red curve in Fig. 2.4(c).

Rotational excitations of the H_2 molecules of the adlayer are clearly resolved, at an energy of 43.50 ± 0.04 meV. This is in good agreement with the theoretical value of 43.9 meV for 3D rotational modes of the free molecule, see Fig. 2.3. Moreover, the increase of the conductance due to this additional tunneling channel is of ∼ 60%, high when compared to the ∼ 20% to ∼ 50% of increase of conductance of H_2 physisorbed on thin decoupling layers like h-BN/Ni(111) [68]. This first example shows that rotational excitations of molecular hydrogen can be obtained even when physisorbed on the surface of bare metal substrates. The corresponding increase in conductance in $\mathrm{d}I/\mathrm{d}V$ signal can also be much more important than what the literature reports for H_2/Au(110) [49].

(a)

2 nm

(b)

1 nm

pm

(c)

(d)
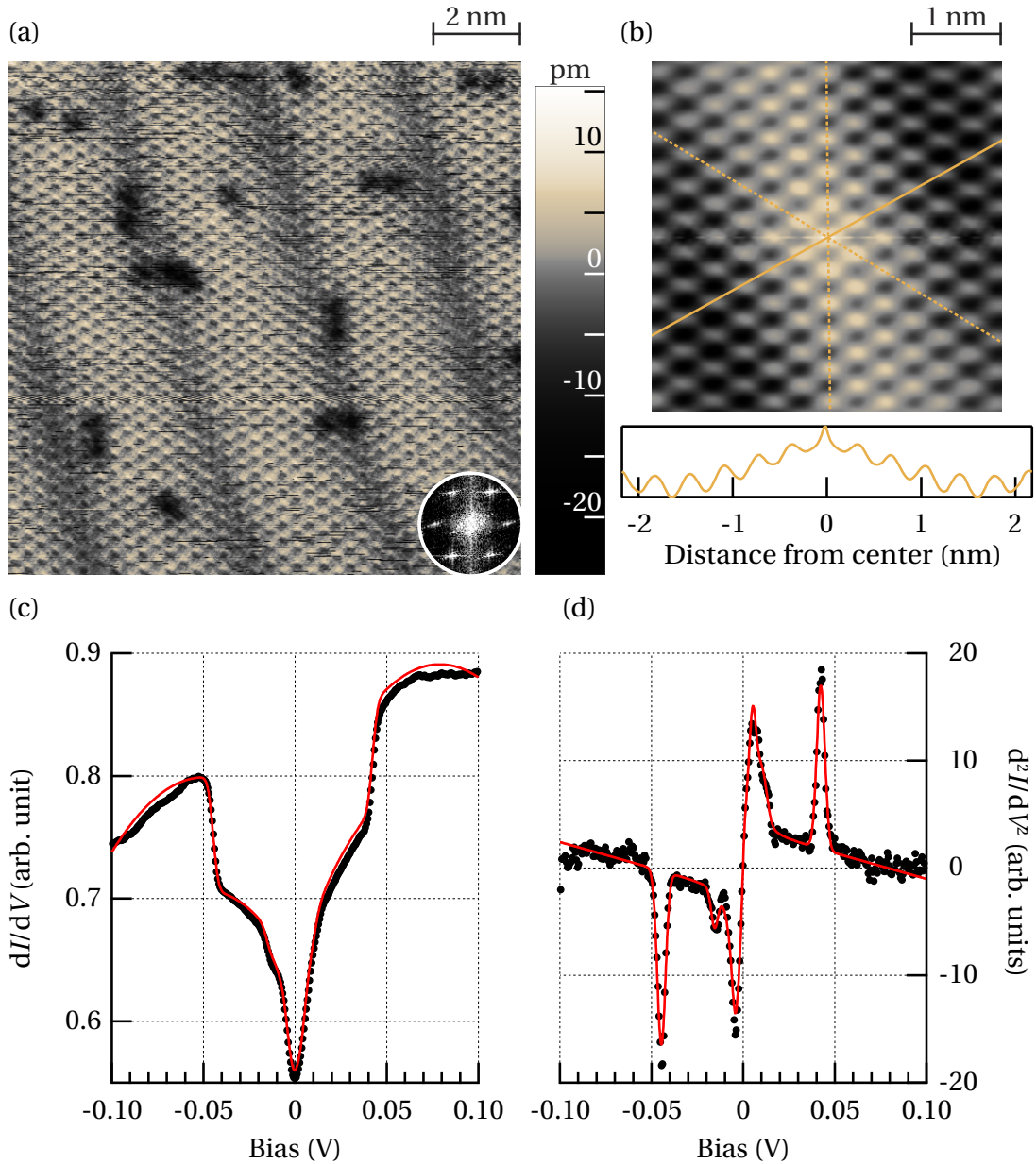
Figure 2.4 – (a) STM image of H$_2$ physisorbed on the Ag(100) (the dose was 100 L). Note that the molecular resolution allows also to observe the moiré originating from the mismatch between the square lattice of the substrate and the hexagonal lattice of the physisorbed layer ($V_t = -20$ mV, $I_t = 20$ pA, $T_{STM} = 5$ K). Inset: Fast Fourier transform of the STM image showing the hexagonal order of the physisorbed layer. (b) Autocorrelation of the STM image in (a). The profile in the lower part of (b) reports the autocorrelation along the solid orange line in the image (b), allowing for extraction of the lattice parameter of the H$_2$ layer. (c) Differential conductance dI/dV and (d) d^2I/dV^2 recorded on the system in (a). Clear conductance steps at 43.50 ± 0.04 meV evidence rotational excitation of H$_2$. The red curves are extracted from fit to the d^2I/dV^2 data. (Set-point: $V_t = -20$ mV, $I_t = 20$ pA, modulation frequency of 397 Hz with a peak-to-peak amplitude of 2 mV).

Physisorption of H_2 on Cu(100)

The second system being investigated is physisorption of H_2 on the Cu(100) substrate, reported in Fig. 2.5. It appears that molecular resolution is hard to achieve, nevertheless the STM image shows that two different orientational domains coexist on the sample. The first one is depicted with the green star, at the top-center location of the STM image; the second one with the orange star, at the middle-right of the same image. Fast Fourier transform of the image, in the inset of Fig. 2.5, confirms the assignment of two orientational domains as it exhibits two series of six bright spots, *i.e.*, the H_2 molecules in each domain adopt an hexagonal packing configuration, with an intermolecular distance of 3.7 ± 0.1 Å. Angular difference between the two orientational domains is deduced from the separation between the peaks in the FFT. Due to the low resolution on the H_2 molecules in Fig. 2.5, the associated FFT peaks are diffuse and one cannot read very precisely the angular difference. Including some uncertainty due to these diffuse peaks, we establish that the two domains are angularly separated by $30° \pm 7°$.

Differential conductance spectroscopy of H_2 physisorbed adlayer on Cu(100) is reported in Fig. 2.6(a). The black data corresponds to the spectroscopic data taken on the H_2 molecules in Fig. 2.5, while the blue one corresponds to another sample. They are averages of 547 and 1863 individual spectra, respectively. The associated error over the mean, not shown for clarity, is 0.003 and 0.005 for black and blue data, respectively. Rotational excitation are identified around ± 0.05 V bias as a slight increase in the conductance ($\sim 15\%$). The d^2I/dV^2 data in Fig. 2.6(b), obtained from numerical derivation of the dI/dV data, better shows the rotational excitation of the H_2 molecules, with the peak indicating a rotational excitation energy of 43.8 ± 0.2 meV.

Two examples of STS on H_2 molecules physisorbed on metals are reported in the literature, Li *et al.* with H_2/Au(100) [49] and Gupta *et al.* with H_2/Cu(111) [52]. We assume that Gupta *et al.* did not observe the rotational excitations of molecular hydrogen for two reasons. First, the increase of conductance appears to be very small, at least with our H_2/Cu(100) system. Integration over thousand, or at least hundred, spectra are mandatory in order to evidence a rotational excitation signature out from the noise of the individual STS spectra. The second point concerns the coverage. We physisorbed enough H_2 molecules such that molecular resolution (resolution over the individual molecules forming the adlayer) was obtained. This implies that the molecular motion is strongly reduced as we can image them. STM images of the work of Gupta *et al.* do not display such kind of resolution; on the contrary, anything but the substrate is imaged, see Fig. 1(a) of reference [52]. We assume that higher H_2 coverages and integration over many spectra would have been recommended in their experiment to exhibit the signature of rotational excitations for H_2/Cu(111).

We recall that we rather interest in probing as few as possible molecules with our STS technique, therefore we introduce in the following the results obtained for rotational excitations of H_2 physisorbed on monolayer islands of Xe on metallic substrates. The driving idea is that islands of Xe of any size could be generated simply by varying the Xe exposure time. This appears as a good route to probe single H_2 (D_2) molecule on very small Xe islands.
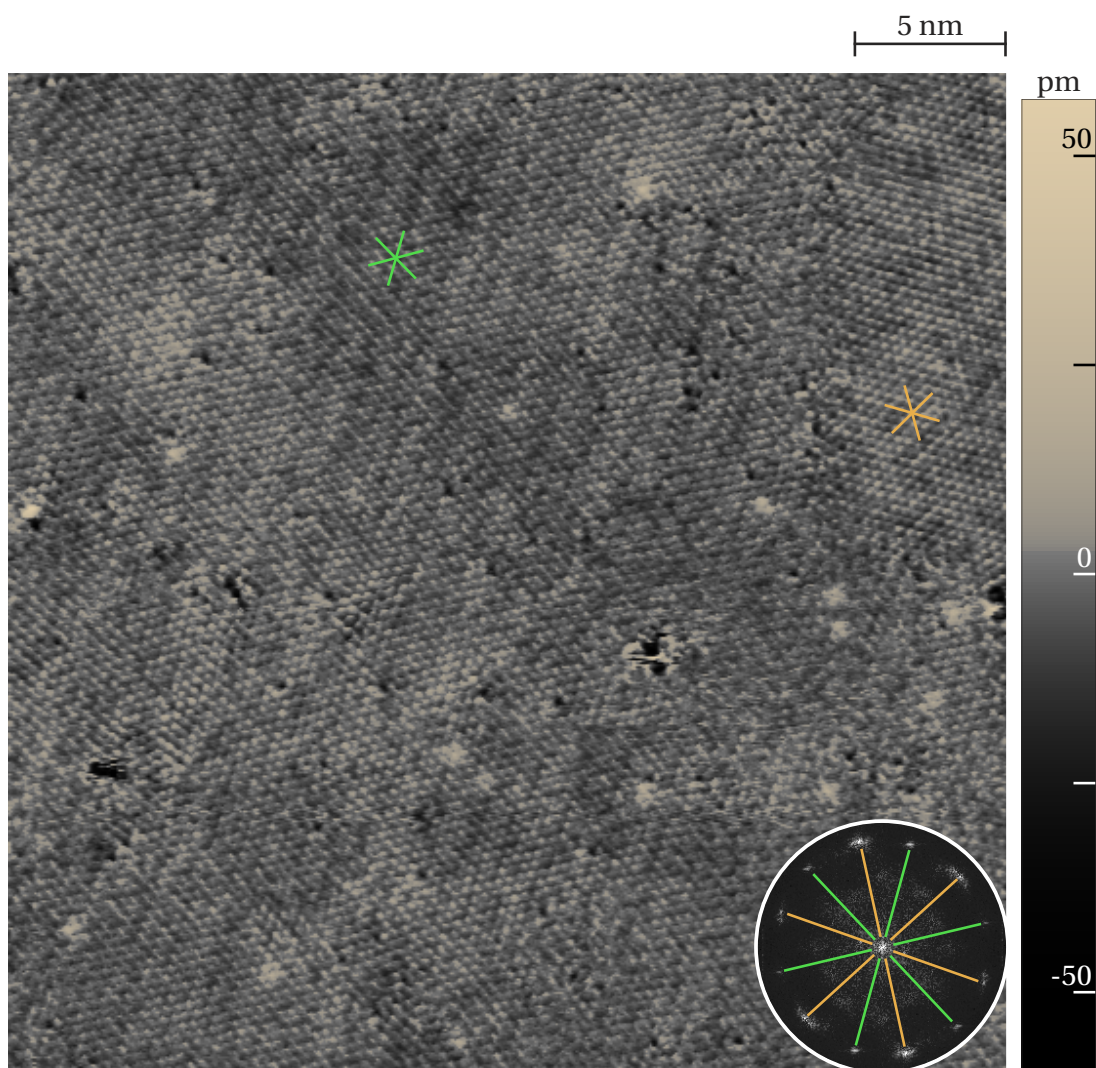
Figure 2.5 – STM image of H$_2$ physisorbed on Cu(100) substrate (dose of 150 L). No moiré is visible but the molecules assemble themselves to form domains with different alignment, depicted by the orange and green stars whose branches are aligned on the directions of the first nearest molecular neighbor. Inset: Fast Fourier transform of the image clearly identifying two orientational domains (orange and green). ($V_t = -20$ mV, $I_t = 20$ pA, $T_{STM} = 5$ K).

(a)

(b)
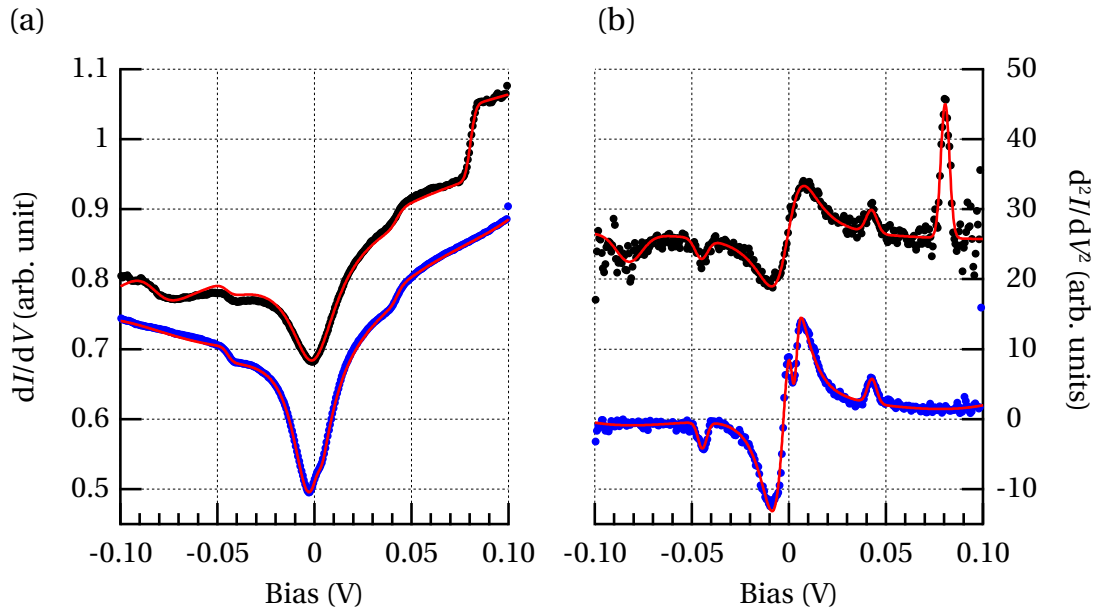
Figure 2.6 – (a) Differential conductance $\mathrm{d}I/\mathrm{d}V$ of H_2 physisorbed on Cu(100). The black and blue data points stand for two different samples. (b) $\mathrm{d}^2 I/\mathrm{d}V^2$ data obtained by numerical derivation of the data in (a). The data shown in black was measured on the H_2 adlayer presented in Fig. 2.5. Conductance steps in (a), or peaks in (b), evidence the rotational excitation of the molecular adlayer at energies of 43.8 ± 0.2 meV. Red curves in (b) are fits to the $\mathrm{d}^2 I/\mathrm{d}V^2$ data, and subsequently integrated to produce the red curves in (a). The inelastic step at 81.4 ± 0.2 meV in the black spectrum remains unidentified, as it does not appear in the data in blue. Data curves are offset for clarity. (Set-point: $V_\mathrm{t} = -20$ mV, $I_\mathrm{t} = 20$ pA, modulation frequency of 397 Hz with a peak-to-peak amplitude of 2 mV).

2.3.2 Physisorption of H$_2$ on Xe-decorated metal substrates

Noble gases are candidates as thin decoupling layers for the physisorption of H$_2$ on metal substrates due to their expected low interaction with the metallic surface. In the following we use Xe gas as decoupling layer.

Physisorption of the Xe gas on the metallic sample [Ag(111), Cu(100)] is done in the same way as for H$_2$. We fill the STM chamber with a partial pressure of Xe and dose it with the sample held at liquid helium temperature. During the gas exposure, the sample temperature raises up to 10 K. This is a sufficiently low temperature for the Xe atoms to physisorb on the metallic surface. After imaging the sample with the STM, we additionally expose the Xe/metal sample to H$_2$. We end with samples holding Xe and H$_2$ at the surface.

H$_2$ on Xe islands on Ag(111)

Figure 2.7(a) shows a typical STM image of Xe-decorated Ag(111) substrate. Terraces of Ag(111) are separated by monoatomic steps. The physisorbed Xe atoms tend to form islands connected to the Ag(111) steps. The Xe islands are usually monoatomic thick, but some are already bi-atomic thick, see for example the two levels of brightness for the island at the upper-right corner of Fig. 2.7(a). The islands are relatively stable allowing for STM imaging, as reported in Fig. 2.7(b). The Xe atoms adopt a regular hexagonal structure whose lattice constant is 4.6 ± 0.2 Å, in good agreement with the value of 4.45 Å for Xe/Pt(111) [77]. Note that the measurement parameters we had for Fig. 2.7(b) were such that the interference pattern of the electron gas of the Ag(111) surface state is resolved close to the Xe-island edge, and it follows the shape of the Xe island.

After exposure to the H$_2$ gas, the conditions of measurement were degraded, as the STM junction was usually unstable. We understand this as the effect of the H$_2$ molecules which are poorly attached to the Xe. This can also be due to the effect of the ortho- to para- conversion of the o-H$_2$ which releases energy transformed into kinetic motion of the physisorbed H$_2$ layer. Indeed, ortho-para conversion of H$_2$ takes place within a timescale a minute [66] and each o-H$_2$ which converts into p-H$_2$ release an energy of 14.7 meV, see Fig. 2.3 or reference [62]. This in an important energy that can favor the molecular mobility of the H$_2$ layer. For comparison, the energy needed to desorb molecular H$_2$ from the Ag(111) surface is about 27 meV [70]. Therefore, when scanning over the Xe islands, we loose the resolution quality obtained in Fig. 2.7 and perhaps attach hydrogen molecules to the STM tip, which are lost right after, causing the instability of the junction. In addition, molecular resolution on H$_2$ molecules was never achieved for this particular system. For both reasons we do not show any STM image of H$_2$ and Xe. Note nevertheless that they would not have different appearance than Fig. 2.7, specially if no molecular resolution is achieved.

STS spectrum over the Xe islands are obtained and shown in Fig. 2.8. The sharp transition at an energy of 43.4 ± 0.6 mV could be the signature of the rotational excitation of the H$_2$ molecules. Note nevertheless that the shape of the peaks and the associated increase in conductance do not have the standard shape following simply an increase of conductance, like what is
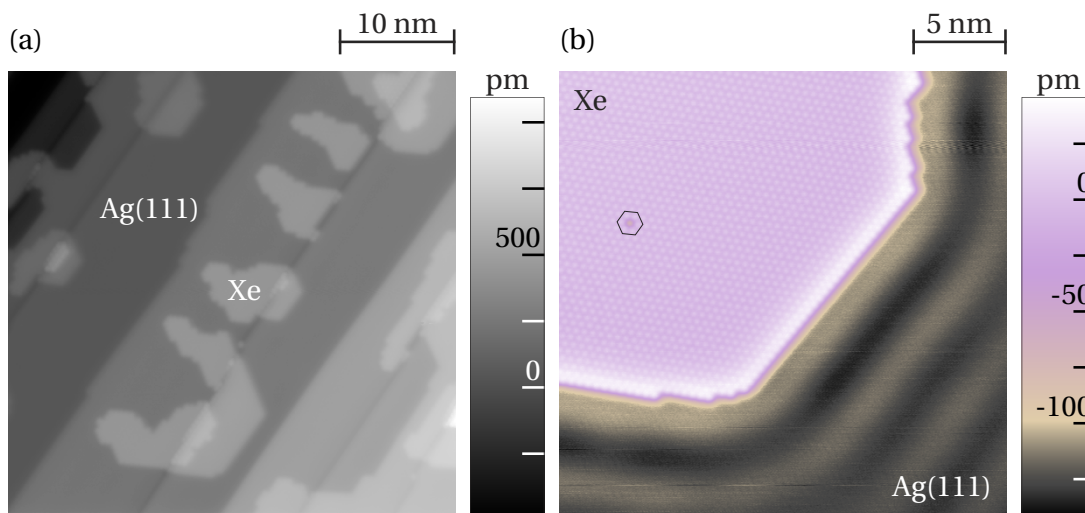
Figure 2.7 – (a) STM image of the Ag(100) surface partially covered with Xe following an exposure of 300 L. Island nucleate almost from the Ag(111) steps ($V_t = -200$ mV, $I_t = 20$ pA, $T_{STM} = 5$ K,). (b) STM image of the system in (a) with resolution on the individual Xe atoms. Note that the Ag(100) surface electron wave interference due to the presence of the Xe island is also resolved. The hole within the black hexagon is understood as a Xe vacancy. ($V_t = -20$ mV, $I_t = 20$ pA, $T_{STM} = 5$ K).

reported in Figs. 2.4 and 2.6 or the ones reported in references [68, 69]. The shape looks similar to what is reported in references [51, 52] and explained as conformation switching of the p-H_2 molecule inside the STM junction. We can consider two ways of probing whether the transitions in Fig. 2.8 are related to the rotational excitation of Xe-physisorbed H_2 molecules. The first possibility is to change the substrate, this is what we will investigate in the following section. The second possibility is to change the physisorbed species to something which does not have spectroscopic features around 44 meV, *i.e.*, change H_2 for D_2. This latter possibility is investigated in section 2.4 with the study of rotational spectroscopy of D_2.

H_2 on Xe islands on Cu(100)

In order to have some elements of comparison for the dI/dV spectra obtained at the previous section, we investigate now the spectroscopic features of H_2 physisorbed on Xe islands on Cu(100). We start by showing STM images of the substrate prior to the H_2 exposure.
Figure 2.9 shows a large-scale STM image of a Cu(100) terrace with Xe islands physisorbed on it. Black depressions on the metallic substrate are supposed to be contaminations, possibly by CO_2. The Xe islands grow forming large monoatomic-thick islands. Sometimes a second layer of Xe atoms nucleate on top of the first layer, as indicated by the arrow in the Fig. 2.9. The Xe adatoms adopt an hexagonal packing with lattice parameter of 4.4 ± 0.1 Å, very close to value of 4.6 ± 0.2 reported previously for Xe/Ag(111), and for Xe/Pt(111) [77].
We further expose the sample to H_2 gas and image it by STM. This is reported on the Fig. 2.10(a),

(a)

(b)
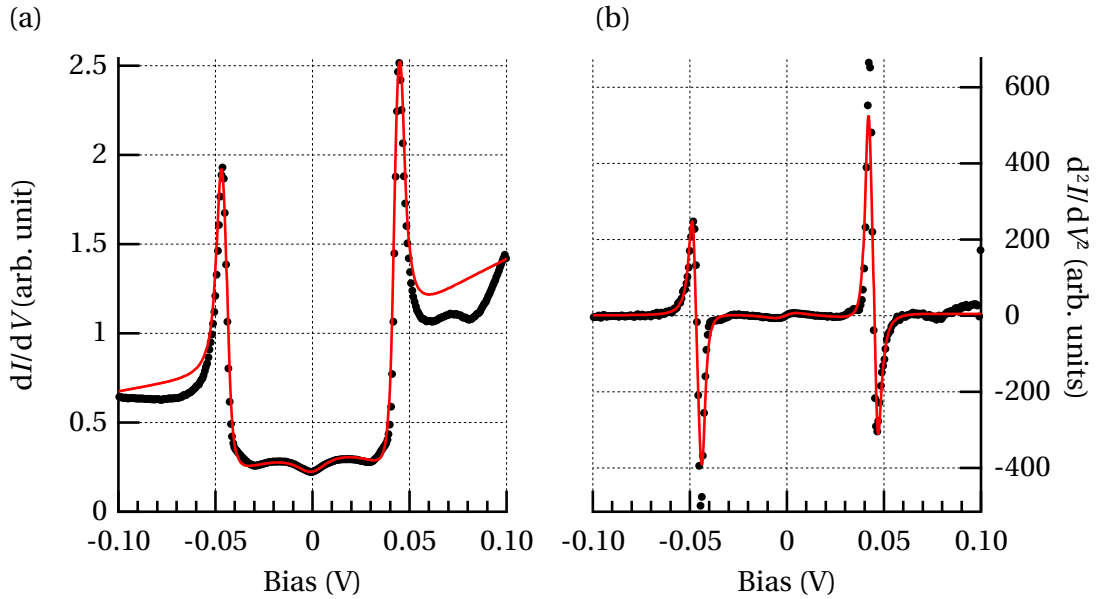
Figure 2.8 – (a) Differential conductance spectrum and (b) related d^2I/dV^2 spectrum, (b), recorded on a large Xe island physisorbed on Ag(111), after an exposure of 70 L of H_2. The data is an average of 150 individual spectra. Large peaks in the dI/dV spectrum reveals a punctual increase in the conductance for a bias of 46.0 ± 0.1 mV. (Set-point: $V_t = -20$ mV, $I_t = 20$ pA, modulation frequency of 397 Hz with a peak-to-peak amplitude of 2 mV).

where a Xe island is covered and surrounded with a H_2 layer. The H_2 molecules adopt a hexagonal packing with two different rotational domains observed, see the green and orange stars on Fig 2.10(a). Lattice parameter measured on this image for H_2 is of 3.6 ± 0.2 Å. We have seen in section 2.3.1 that the two orientation for H_2 are separated by $\sim 30°$. Here we add that, relatively to the orientation of the Xe atoms, the H_2 molecules are orientated with $+13.3° \pm 0.5°$ and $-16.5° \pm 0.5°$ in this image. Fast Fourier transform in Fig. 2.10(b) evidences the hegagonal packing of both the Xe and H_2 as well as the difference in angular orientation of their respective lattice. Note that for symmetry reasons another rotational domain for the Xe islands should exist. This can be seen from the orientation adopted by the Xe islands in Fig. 2.9.

Differential conductance spectroscopic curves are reported in Fig. 2.10(c), and the associated d^2I/dV^2 data, obtained with numerical differentiation, in Fig. 2.10(d). Black and blue spectra stand for measurements on two different samples and are averages of 280 and 650 individual spectra, respectively. At first sight the shape of the dI/dV curve can vary, possibly due to a different tip apex. We got two shapes, the black one resembling to the spectra obtained for H_2/Xe/Ag(111), see Fig. 2.8, and the blue one resembling to the shape of dI/dV curves obtained for H_2 physisorbed on metals, see Fig. 2.4 and Fig. 2.6. From the d^2I/dV^2 data, we extract the energy of 45.8 ± 0.1 mV and 44.0 ± 0.2 mV, the bias at which the black d^2I/dV^2 curve crosses 0, and at which the small peaks on the blue curve is located, respectively. From that we draw the
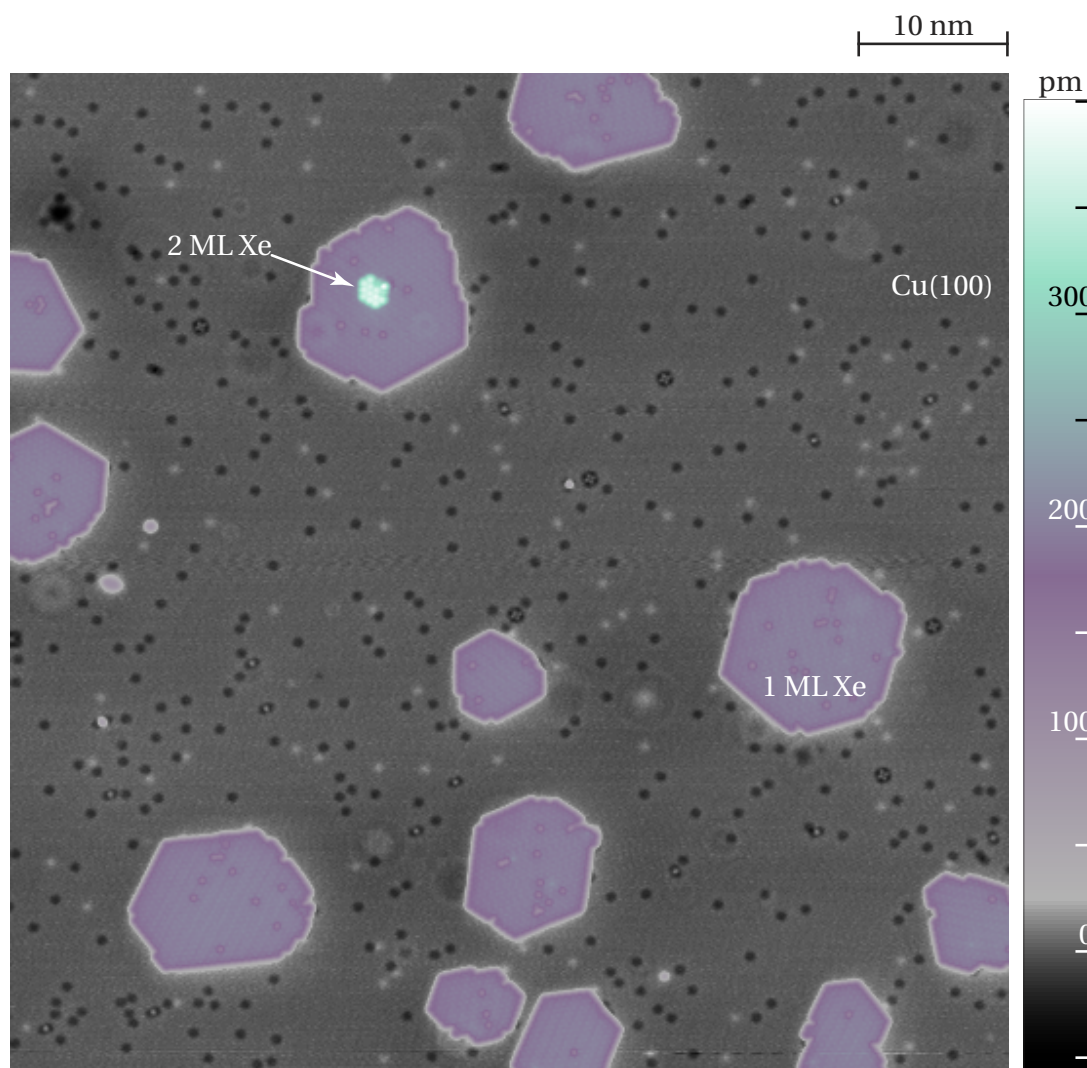
Figure 2.9 – STM image of the Cu(100) surface after exposure to 50 L of Xe. The gas atoms form islands on the copper terrace. Black depressions are attributed to contaminations of the crystal surface. Usually the height of the Xe island is of one atom thick. Occasionally a second Xe layer can nucleate on top of the first layer, labeled as "2 ML Xe" on the image. ($V_t = -50$ mV, $I_t = 20$ pA, $T_{STM} = 5$ K).

following observation. First, rotational excitations of p-H$_2$ on Xe islands is clearly observed for H$_2$/Xe/Cu(100). Second, it can happen that the p-H$_2$ rotational signature in dI/dV curves can be buried into another signal whose origin is not known, probably due at some interaction between the H$_2$ molecule and the Xe atoms (spectroscopy over the Xe/Cu(100) alone do not exhibit any conductance peak). Indeed, because of the big local increase in conductance at bias of ~ 46 mV in Fig. 2.10(c), see also the Fig. 2.8(a), one could not observe the rotational excitation signature of the p-H$_2$. The question which comes out from these observations is whether the peak in conductance at ~ 46 mV is related with the excitation of the first rotational mode of the p-H$_2$. To answer this question, one should replace the H$_2$ with D$_2$ and check if the conductance peak moves to a bias of ~ 22 mV bias.

2.3.3 Conclusions on systems with physisorbed H$_2$

Signature of the rotational excitation of the p-H$_2$ molecule was observed on metal substrates and, in the case of the Ag(100) surface, the increase of conductance due to this new tunneling channel is of ~ 60%, which is as important as what is reported for systems using a thin graphene or h-BN decoupling layer between the H$_2$ molecules and the metallic substrate [68, 69]. In addition, the use of the Xe as a decoupling layer is also possible and the rotational signature of p-H$_2$ molecules is still observed. Nevertheless, the possibility to interpret STS spectra for H$_2$/Xe/metal depends on the contingent conditions of the tunneling junction (STM tip apex, stability of the STM junction with respect to the surrounding hydrogen, ...) as sometime the dI/dV spectrum exhibits important peaks very close to the energy of the first rotational excitation energy for p-H$_2$. To learn whether this feature is related to the first rotational transition of p-H$_2$, we will replace H$_2$ with D$_2$ and renew the experiments.

2.4 Experimental results for D$_2$ physisorbed on metal substrates and on Xe islands

2.4.1 Rotational spectroscopy of physisorbed D$_2$ on metal substrates

Deuterium molecule is identical to the hydrogen one from the chemical point of view. Nevertheless, from the physical one, it is very different as the nuclei of the deuterium atom is composed of a neutron and a proton. This change of the nuclear mass of the D$_2$ molecule with respect to H$_2$, and, therefore, of the molecular mass, implies differences in the spectroscopic features we can probe with STS. The first rotational excitation transition energy for D$_2$ is of ~ 22 meV. Then, we can carry out the same experiment presented in section 2.3 and seek whether all the spectroscopic features identified as rotational excitation move to the 22 meV region. We investigated two metallic samples: Ni(111) and Cu(100).
STM images of D$_2$ physisorbed on Cu(100) surface resemble to the ones presented in section 2.3.1, *e.g.*, Fig. 2.5. Molecular resolution of D$_2$ physisorbed on Ni(111) was not obtained, this is why no STM image is shown, we present only the STS spectra for such systems.

(a)

5 nm

(c)
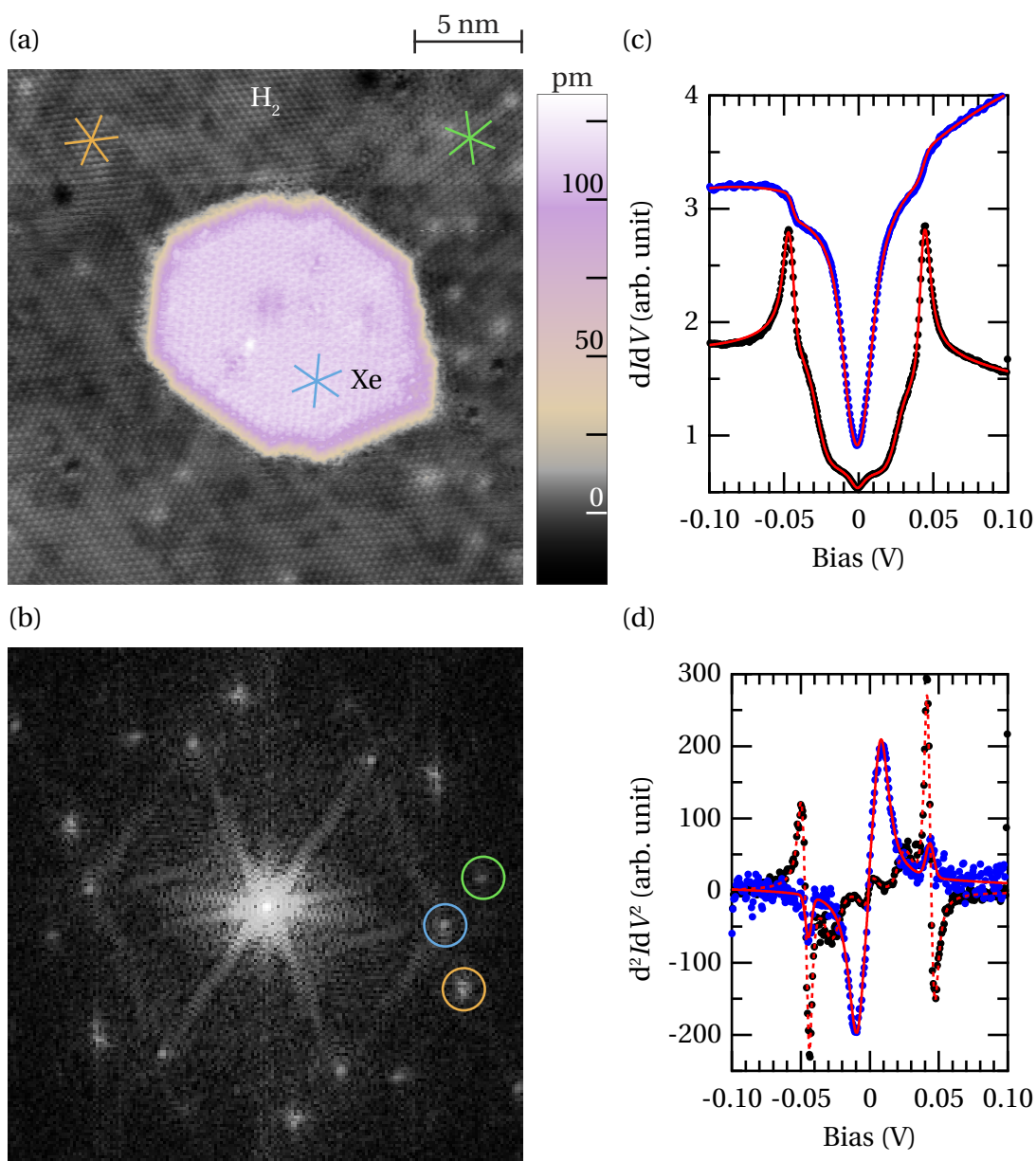
Figure 2.10 – (a) STM image of a Xe island physisorbed on Cu(100) with additional hydrogen. Note that the molecular (atomic) resolution is achieved on the H_2 (Xe) layer. Two orientational domains for H_2 are indicated by the orange and green stars. Note that their orientation differs from the one of Xe, see the blue star ($V_t = -50$ mV, $I_t = 20$ pA, $T_{STM} = 5$ K). (b) Fast Fourier transform of the STM image in (a) exhibiting the hexagonal packing of the H_2 and Xe layer. Each colored circle indicates the FFT peak describing the associated colored star in (a). (c) dI/dV spectra for two different samples obtained on a H_2-covered Xe island, and (d) corresponding d^2I/dV^2 data. The blue dI/dV (d^2I/dV^2) curve was multiplied by a factor 10 (15) and subsequently offset for clarity. (Set-point: $V_t = -20$ mV, $I_t = 20$ pA, modulation frequency of 397 Hz with a peak-to-peak amplitude of 2 mV).

Figure 2.11(a–b) presents the dI/dV and d^2I/dV^2 curves, respectively, for D$_2$ physisorbed on the Cu(100) surface. The dI/dV signal is obtained from the mean of 1548 individual spectrua, while the d^2I/dV^2 data was obtained from numerical differentiation of the dI/dV data. The small step in the differential conductance evidences the first rotational excitation for the o-D$_2$ molecule, clearly resolved in the d^2I/dV^2 data at an energy of 22.5 ± 0.1 meV.

Spectroscopy for D$_2$ physisorbed on Ni(111) surface is reported in the Fig. 2.11(c–d) for dI/dV and d^2I/dV^2 curves respectively. The dI/dV data is obtained from the mean of 11 individual spectra and displays a clearly different shape, resembling to the ones reported in the work of Halbritter *et al.* about gold-hydrogen nanojunctions [51]. We determine the bias at which the negative peaks appear by reading the bias at which the d^2I/dV^2 crosses zero, *i.e.*, 20.8 ± 0.01 mV. This energy is very close to the on expected for the first rotational excitation transition of the o-D$_2$ molecule, thus we identify it as a signature of the rotational excitation of o-D$_2$ physisorbed on Ni(111).

2.4.2 Rotational spectroscopy of physisorbed D$_2$ on Xe-decorated metal substrates

After having observed the signature of the first rotational excitation for the o-D$_2$ molecule, we want to determine whether we can observe them also for D$_2$ physisorbed on a thin Xe layer. We probed two systems, D$_2$/Xe/Ag(111) and D$_2$/Xe/Cu(100), whose results are reported in Fig. 2.12. We report in Fig. 2.12(a–b) the dI/dV and d^2I/dV^2 curves for D$_2$ physisorbed on a Xe island on Ag(100). The dI/dV data corresponds to the mean of 450 individual spectra. The rotational excitation, faintly observed in the dI/dV data, is clearly resolved in the d^2I/dV^2 curve at an energy of 22.3 ± 0.2 meV. Interestingly, the shape of the dI/dV spectra in Fig. 2.12(a) do not exhibit the peak-like feature observed for H$_2$/Xe/Ag(111), see Fig. 2.8. But this happens for the D$_2$/Xe/Cu(100) system. Indeed, Fig. 2.12(c–d) shows the dI/dV and d^2I/dV^2 data for D$_2$ physisorbed on Xe islands on Cu(100). We observe a strong step in the dI/dV data at a bias of 36.59 ± 0.04 mV. Interestingly, this corresponding to the rotational excitations of the p-D$_2$ molecule, whose theoretical energy threshold for the free molecule is of 36.9 meV. Additionally a small peak in the d^2I/dV^2 data is observed for a bias of 22.8 ± 1.8 mV, thus suggesting that the first rotational excitation of the o-D$_2$ molecules occurs also. To better show this feature, the light-blue curves of Fig. 2.12(c–d) represent the dI/dV(d^2I/dV^2) data magnified by a factor 10 (20), respectively. The peak at 22 mV in the d^2I/dV^2 data becomes visible, still much weaker than the strong peak.

2.4.3 Conclusions on systems with physisorbed D$_2$

We have seen that STS is also capable of detecting the rotational excitation signature for D$_2$ molecules physisorbed on metallic substrates and on Xe islands. Depending on the STM-tip conditions, or on other uncontrollable parameters, the dI/dV spectra can display just a simple increase in conductance at the right energy or can display a negative differential conductance shape as described in reference [51]. The data obtained is very similar to the data for H$_2$ physisorbed on metal and on Xe.
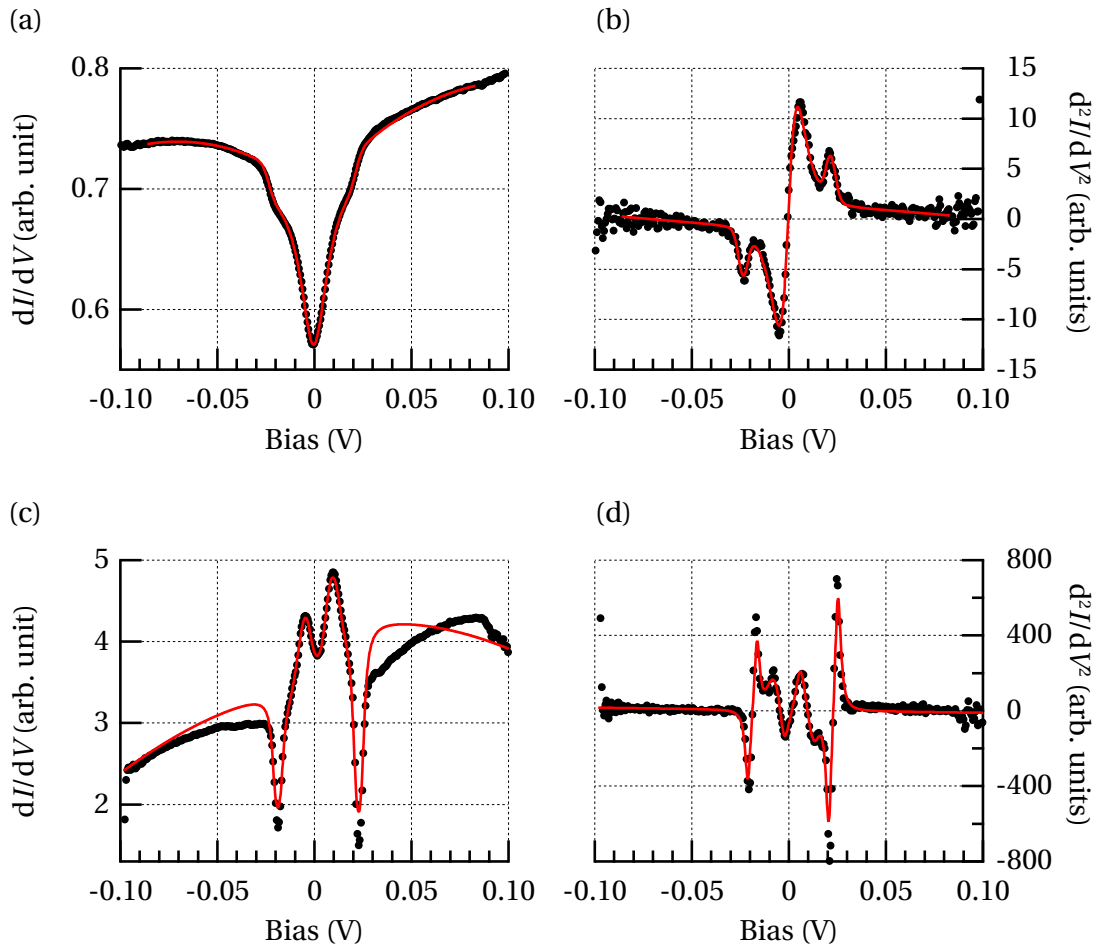
Figure 2.11 – Differential conductance spectroscopy curves for D_2 physisorbed on (a) Cu(100) and (c) Ni(111), and associated d^2I/dV^2 data in (b) and (d), respectively. First rotational excitation for o-D_2 is observed at a bias of 22.5 ± 0.1 mV for D_2/Cu(100), still better resolved in the d^2I/dV^2 spectrum. Rotational excitations of o-D_2 on the Ni(111) substrate are suspected at a lower energy of 20.8 ± 0.1 mV. The set-point conditions for both measurements are: $T_{STM} = 5$ K, $V_t = -20$ mV, $I_t = 20$ pA, modulation of 2 mV (peak-to-peak) at a frequency of 397 Hz.
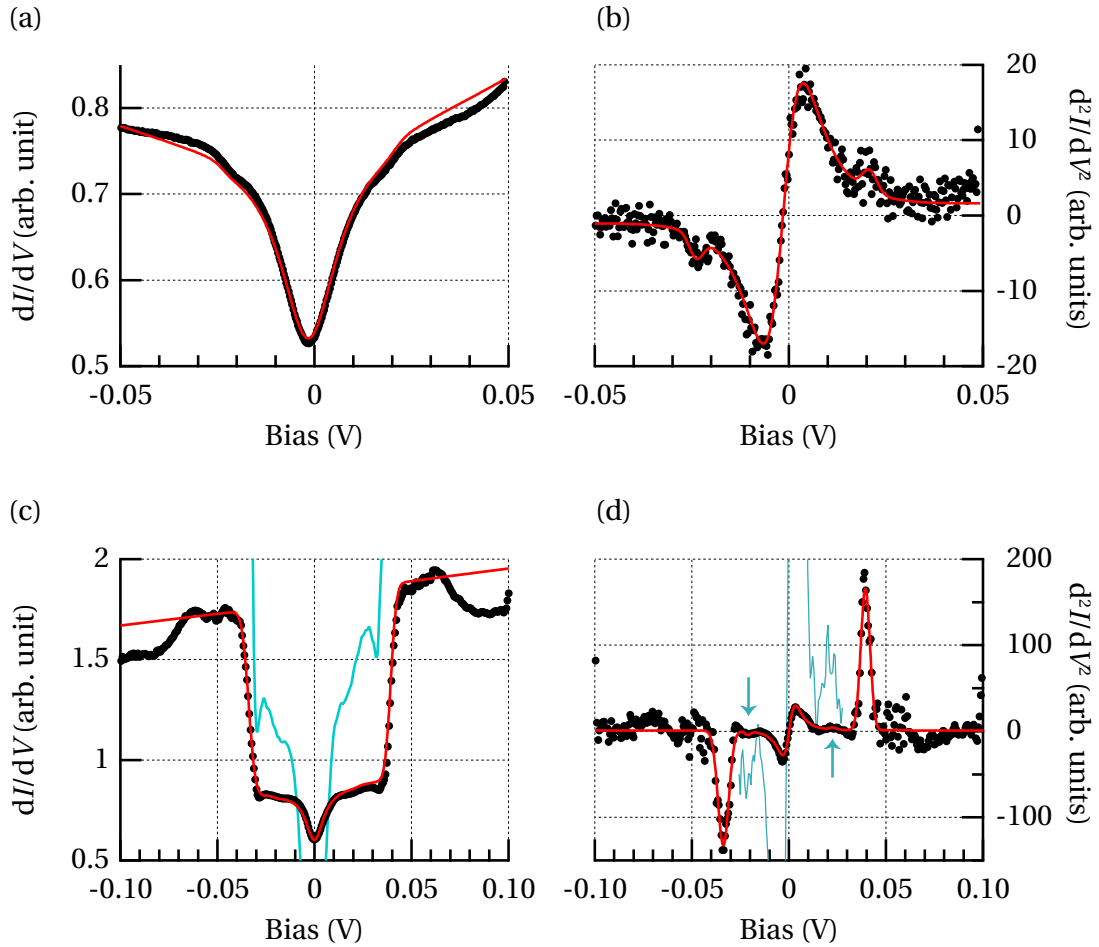
Figure 2.12 – Differential conductance spectroscopy curves for D$_2$ physisorbed on (a) Xe/Ag(111) and (c) Xe/Cu(100) (c), and associated d^2I/dV^2 data in (b) and (d), respectively. First rotational excitation transition for o-D$_2$ is observed for a bias of 22.3 ± 0.3 mV. Strong rotational excitation signal for p-D$_2$/Xe/Cu(100) occurs at an energy of 36.59 ± 0.04 meV, while the signal related to o-D$_2$/Xe/Cu(100) is scarcely visible at 22 ± 2 mV. Light blue curves in (c) [(d)] depicts the black data magnified by a factor 10 (20), for dI/dV (d^2I/dV^2), respectively, better showing the rotational excitation of o-D$_2$. Set-point conditions for both measurements: $T_{STM} = 5$ K, $V_t = -20$ mV, $I_t = 20$ pA, modulation frequency of 397 Hz with a peak-to-peak amplitude of 2 mV.

2.5 General discussion on systems of physisorbed H_2 and D_2

We have seen that rotational quantumstate excitation of H_2 (D_2) is possible on metallic substrates as well as on a decoupling Xe layer. The threshold energies obtained correspond to the ones for the free molecule. We also used Xe islands as decoupling layer. The idea is that one can grow islands of arbitrary small size down to the single atom level with, at the same time, allow for decoupling from the metal substrate the physisorbed H_2 (D_2) molecule. Though, after physisorption of H_2 (D_2), spectroscopy on such small islands was unstable on Cu(100) samples. Figure 2.13 illustrates the problem. On the very small Xe islands, spectroscopy becomes impossible as they are unstable, see the small Xe island inside the red circle of Fig. 2.13. We resign ourselves to accept that this idea was not the right one to answer the question whether one single H_2, or D_2, molecule exhibit rotational excitations with STS. Nevertheless, we understood some other aspects concerning H_2 (D_2) layers on metal, and on Xe/metal. First, rotational excitation of molecular H_2 (D_2) is clearly observed on bare metal substrates. This meets the conclusions of HREELS studies where rotational excitations were also observed on Ag and Cu substrates [64–67]. Sometimes, depending on the measurements conditions, the $\mathrm{d}I/\mathrm{d}V$ spectra exhibit a clear negative differential conductance shape. This is shown here for D_2/Ni(111), but it was also observed for others metal substrates from time to time. For now we only have the phenomenological models from the literature [51, 52] and we are not sure that they would explain what is happening in our system. Therefore, we cannot explain with certainty the variety of shapes of spectra observed.

From the rotational spectroscopy results on Xe islands physisorbed on metallic substrates we learn that the Xe can also act as a decoupling layer. We assume that the H_2 or D_2 molecules are on top of the Xe layer because the energies at which the rotational excitation occurs for H_2 and D_2 is close, or equal, to the theoretical value for 3D rigid-rotor, see Fig. 2.3, thus incompatible with constrained rotational modes for H_2 (D_2) molecules located between the metal substrate and the Xe layer. Indeed, with a reduced phase space accessible for the rotational quantum states of the molecule, rotational levels would appear at lower energies [66]. In addition we were not able to achieve nice imaging of the Xe islands in presence of physisorbed H_2 or D_2, while systems with only physisorbed Xe allows for atomic resolution on the islands. This suggests that the hydrogen is always between the STM tip and the Xe layers, thus on top of them. Unfortunately we could not use such a decoupling layer to observe the rotational excitation on one unique molecule. Because small islands of Xe are unstable in presence of H_2 (D_2), we cannot probe the rotational excitation of H_2 and D_2 on this kind of objects; stable islands would hold already around 30 H_2 or D_2 molecules, which does not help so much.
We also learnt that combination of H_2, or D_2, on Xe gives rise to big steps in the $\mathrm{d}I/\mathrm{d}V$ spectra, that should have something to do with the rotational excitations of such molecules, see Fig. 2.8(a) and Fig. 2.12(c). For the case of D_2/Xe/Cu(100) we have possibly observed for the first time the first rotational quantum state excitation of p-D_2 with STM, corresponding to the form of the molecule associated with odd-values of the rotational quantum number J.
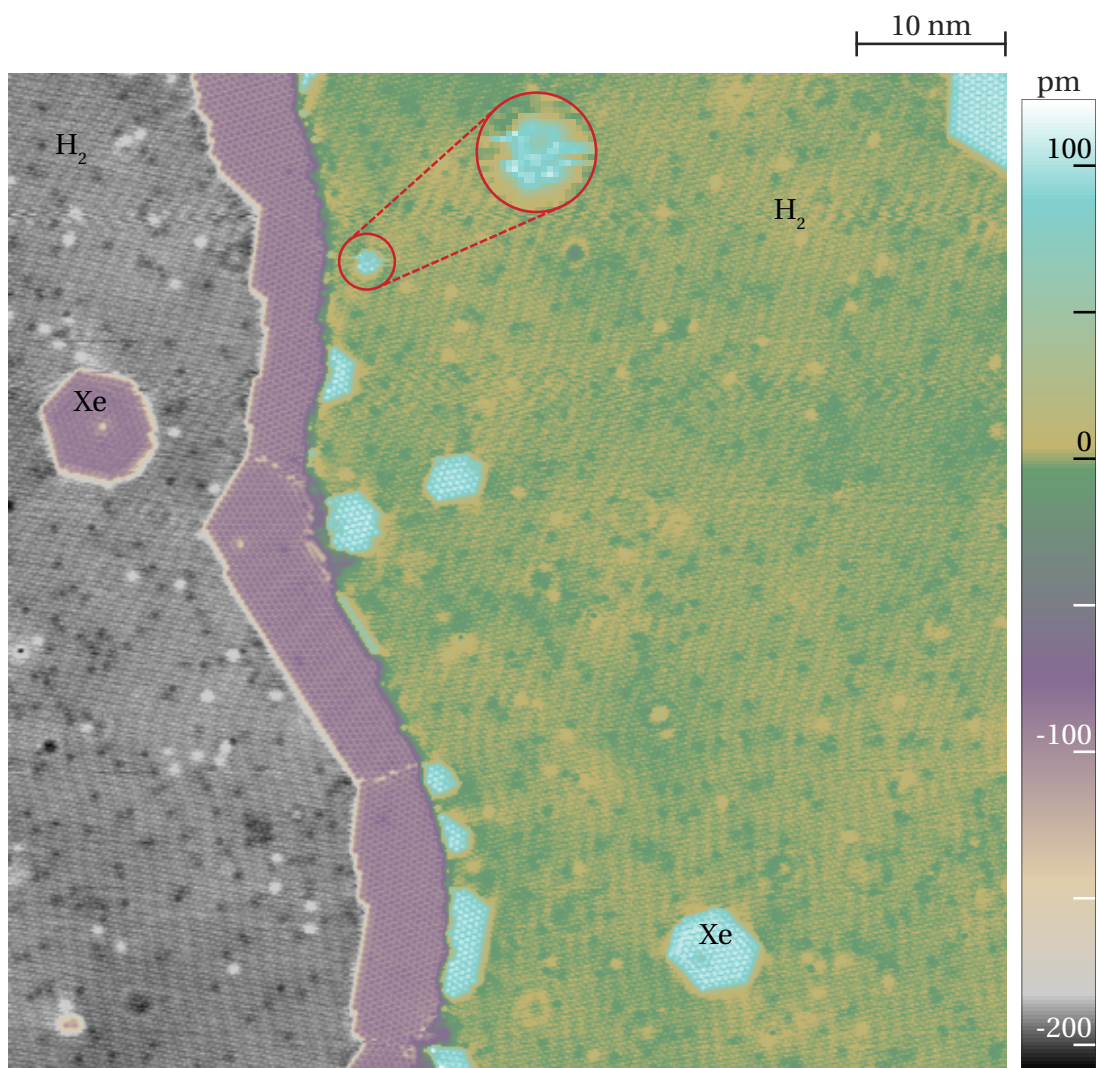
Figure 2.13 – STM image of subsequently physisorbed Xe and H_2 on Cu(100), both dose is of 50 L. Small Xe islands not connected to any step, as the one shown magnified in the red circle, are not very stable; the STM tip disturbs them by moving the Xe atoms at the rim. Left and right part of the image are separated by a Cu(100) step, at which a band layer of Xe atoms is physisorbed on the lower part ($V_t = -20$ mV, $I_t = 20$ pA, $T_{STM} = 5$ K).

2.6 Conclusion

We studied the spectroscopic properties, and partly the assembly, of H_2 and D_2 layers physisorbed on bare metallic substrates. From that we observed that the excitation of the rotational modes for p-H_2, o-D_2 and p-D_2 molecules was possible and reported the first rotational excitation energy of them, summarized on the Tab. 2.4. We were interested whether we could probe the rotational spectrum of one unique molecule with the STM and for that we wanted to use a decoupling layer tunable in lateral size. We choose Xe for that. We verified that rotational excitations of H_2 and D_2 were detectable on the Xe layers physisorbed on metal surfaces. But, by reducing the size of the islands, they became unstable in the presence of H_2 (or D_2). Even if the experiment could not answer the initial question, we learn a lot on what is possible to do with H_2 and D_2 molecules physisorbed on Xe and on metals.

There is still one open question which was not addressed in the present study, concerning the possibility of observing o-H_2 on surfaces with the STM, as it was already possibly observed for p-D_2. We would like to propose an experiment for that. When o-H_2 gets physisorbed on a metal surface, it is assumed that the ortho-para transition occurs in a timescale of minutes, as reported by Svensson and Andersson [66]. Thus observing the rotational excitation of o-H_2 on bare metal surfaces is unlikely as the timescale of spectra recoding with our STM is of the order of minutes too. The idea is to cover the whole the metal surface with the Xe atoms and subsequently expose the sample to H_2. Over the Xe atoms, the H_2 (D_2) molecules are thought to move freely with very few interaction with the metal substrate. That would be some kind of simulation of the gas-phase conditions for the H_2 (D_2) molecules, where the ortho-para transition is negligible. Then one has to record spectroscopic curves for this system and look for the signature of rotational transition for o-H_2 at ~ 73 mV. STM tip could have an influence; the tunneling electrons could also favor the ortho-para conversion, but that is science, trying and seeing!

	Substrate							
	Ag(100)		Ag(111)		Cu(100)		Ni(100)	
	Bare	Xe	Bare	Xe	Bare	Xe	Bare	Xe
H_2	43.50 ± 0.04	—	—	43.4 ± 0.6	43.8 ± 0.2	44.0 ± 0.2	—	—
D_2	—	—	—	22.3 ± 0.2	22.5 ± 0.1	22.0 ± 1.8 36.59 ± 0.04	20.8 ± 0.1	—

Table 2.4 – Summary of the different rotational excitations energy, in unit of meV, measured on various systems by means of the scanning tunneling spectroscopy.

3 Adsorption sites of individual metal adatoms on magnesium oxide thin films

This chapter will focus on the experimental method used to determine the adsorption site of metal atoms (Ho, Er, Dy, Tb, Au, Fe and Co) adsorbed on MgO thin films grown on a Ag(100) substrate. This study relies on a careful analysis of numerous STM images acquired for different systems. DFT results on the adsorption of the Ho and Au atoms on MgO were obtained by Željko Šljivančanin, with the help of his student Srdjan Stavrić, from the Vinča Institute of Nuclear Sciences at university of Belgrade. All the STM data acquired for the Dy/MgO system was measured by Marina Pivetta. Jean-Guillaume De Groot made a counting of the Dy objects, following the method that I proposed and used for all the others presented systems. With common agreement we decide to include these data in the present manuscript because they are part of a logical ensemble, and also because I contributed in the overall analysis of the Dy/MgO system.

3.1 Introduction

Single atoms on ultrathin decoupling layers have recently attracted a lot of attention because of their remarkable properties [48, 78, 79]. For example, single Fe atoms on MgO(100)/Ag(100) show very long spin-coherence times [38], and even longer spin-relaxation times [37, 80, 81]. These are prerequisite for single atom qubits. Single atoms memories are in principle feasible as it has been shown that Ho single atoms adsorbed on MgO(100)/Ag(100) show magnetic remanence [80], at least up to a temperature of 40 K, and can be read and written [37]. Single atoms adsorbed on surface can also exhibit multiple charge states [82–84] and may further catalyze chemical reaction [85]. All these remarkable properties emerge from the interaction of the adatom with the surface, which depends critically on the adsorption site. Knowing this site is therefore mandatory to understand the thermal stability, catalytic properties, charge state and, in addition, the symmetry of the crystal field which determines the lifetime of magnetic quantum states [86].

Methods to determine the adsorption site of an atom include field ion microscope, scanning probes methods like the STM or atomic force microscope (AFM), as well as theoretical calculations where density functional theory (DFT) is extensively used. Field ion microscope is

limited to strongly bound species on metal surfaces [4] and cannot therefore be applied for atomic species weakly adsorbed on oxides. Scanning probes microscopes (AFM and STM) are more versatile and much more employed to determine the adsorption site of adatoms. When possible, concomitant atomic resolved images with the adsorbate is used to determine the adsorption site of the adsorbed species. However, examples from the literature are limited to single element surfaces [33, 50, 87, 88], where the atomic resolution obtained on the substrate can be straightforwardly interpreted. Note that on the surface of ionic crystal as MgO or NaCl, one often ignores which of the two atomic sublattices is observed with atomic contrast, thus complicating the interpretation of atomically resolved images.

DFT calculations is another way to handle the problem. They can in principle determine the adsorption site of the adatom or, potentially help to interpret the origin of the atomic contrast in atomic resolved images of ionic substrate. Nevertheless one cannot blindly follow the results of DFT calculation. Excluding errors of calculation, these are naturally exact in the framework of the model used, but one has to ask itself if the model is representative for the physics we are interested to. The results will depend on some parameters which are freely chosen by the user, usually to fit the experiment. For example, DFT calculation or Au/MgO predicts different adsorption site depending on the methods used [89–91].

Determination of the adsorption site of metallic species on ionic substrate was never done with a techniques really independent from DFT calculation, this is therefore why we setup an experiment to achieve this goal. First, Ho adsorption site on MgO will be determined independently from theoretical considerations and then be used as a marker to determine the adsorption site of other metal atoms. At the end of this chapter we would know the adsorption sites for a various atomic species (Ho, Er, Dy, Tb, Au, Co and Fe) which can be further used as specific site markers for the MgO. At the same time we also provide a method applicable to determine the adsorption site of other elements on any ionic substrate.

The fundamental idea to determine the adsorption site of an adatom with the STM is the use of a marker whose position in, or on, the substrate atomic lattice is very well known. We are interested in determining the adsorption site of Ho atoms on MgO thin films. This atomic species deserves a special attention because this is the first single-adatom exhibiting magnetic bistability up to a temperature of 40 K [80]. To understand the origin of its magnetic properties, one has to know its adsorption site, which defines the crystal field the Ho adatom is subject to. Our assignment is a strong information in complement of the reported DFT calculations [80]. We decided to take Ca atoms incorporated into the MgO layers as marker. Ca is chemically similar to Mg, therefore it is expected to replace Mg atoms in the ionic compound. This is the unique hypothesis we rely on, which is acceptable from a chemical point of view.
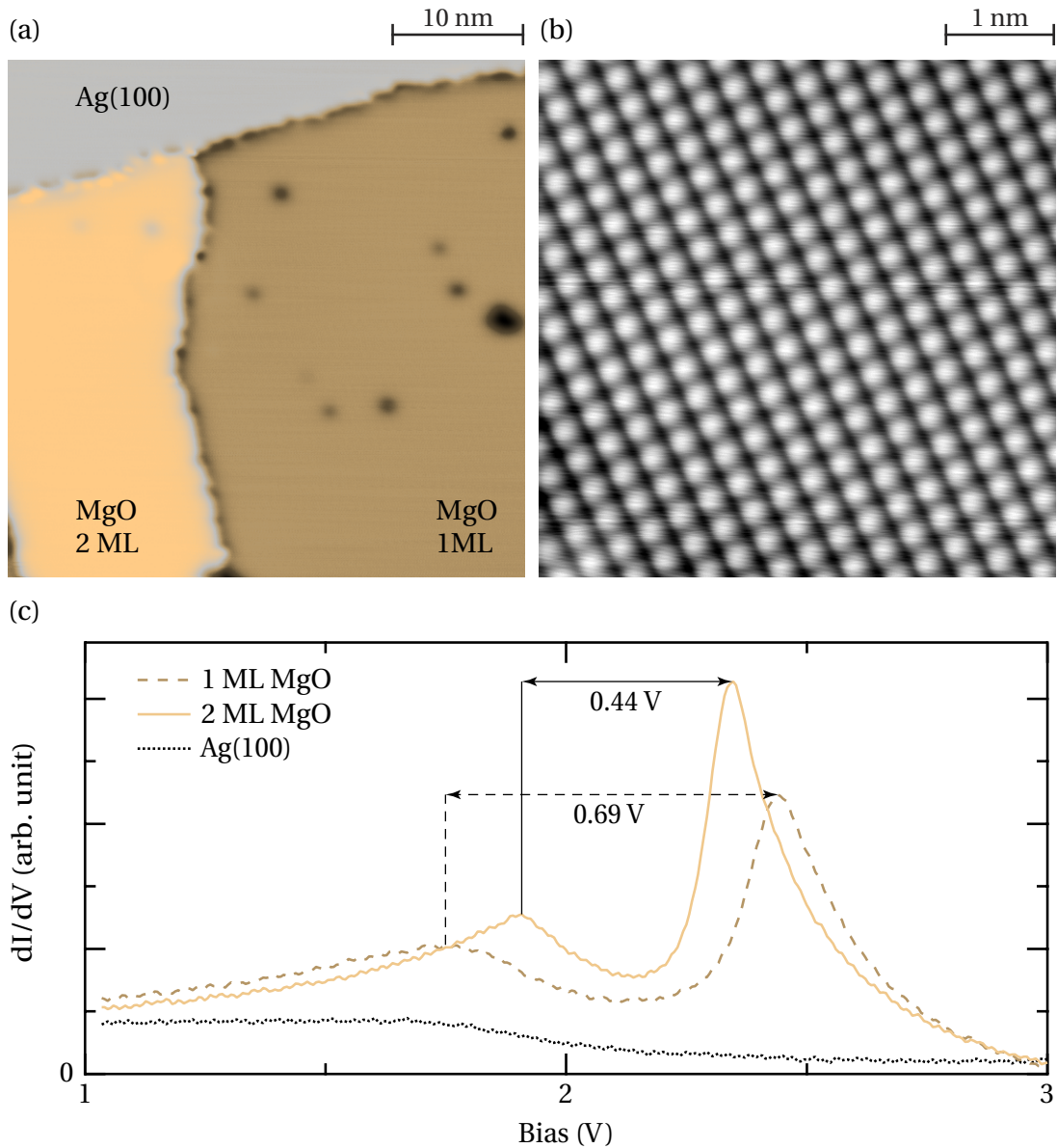
Figure 3.1 – (a) STM image of Ag(100) partially covered by MgO (V_t = 120 mV, I_t = 100 pA, T_{STM} = 5 K). Dark spots are attributed to point defects in the oxide at the interface. (b) Atomically resolved image of 2 ML MgO (V_t = −10 mV, I_t = 10 nA , T_{STM} = 5 K). (c) Field emission resonance spectra recorded above 1 and 2 ML MgO, as well as on clean Ag(100) (V_t = 120 mV, I_t = 100 pA, peak-to-peak modulation amplitude V_{mod}= 10 mV). Adapted with permission from [92].

3.2   Characterization of Ca-doped MgO thin films

For the characterization the Ca-doped MgO thin films, we need first to characterize the pristine MgO films grown on a Ag(100) substrate. The preparation procedure for MgO(100)/Ag(100) thin films consists in the cleaning of the Ag(100) crystal in ultra-high vacuum by repeated cycles of Ar$^+$ sputtering, at an energy of 800 eV and flux of 10 μA/cm^2, with subsequent anneal- ing to 770 K. The MgO thin films were grown from a Knudsen cell under a partial pressure of oxygen of 1×10^{-6} mbar and with the substrate kept at 770 K, as described by Pal *et al.* [93, 94]. After the growth of the MgO layer, special attention is given to the cooling down procedure. As we learn from the works of Pal *et al.* [93, 94], the final thickness of the MgO layers depend crucially on the speed of the cooling of the sample. To reach the room temperature, we cooled down of the sample at a speed from 25 K min^{-1} to 33 K min^{-1}. Calcium-doped MgO films were prepared by co-evaporating Ca and Mg in the same conditions, still allowing for a lower Ca flux, by adjusting the Ca-Knudsen cell temperature to obtain the desired dopant concentration.

Pristine MgO thin films grown on Ag(100) substrate are shown in Fig. 3.1(a). Regions of bare substrate coexisting with MgO islands of two thicknesses are found all over the samples. The MgO layers do not exhibit no superstructure as a moiré pattern or dislocation, providing a direct evidence for a film being uniformly and compressively stained by 3% to form a pseudo- morphic (1×1) structure on the Ag(100) substrate[1], confirming early diffraction studies [95] Since the apparent height of the MgO layers is strongly bias dependent and can be inverted with respect to the one expected from morphology [96] (thicker layers can appear with smaller apparent height than thinner ones, due to the reduced conductance of thick layers), we use FER spectroscopy to distinguish locally between the diverse MgO thickness [53]. The dI/dV spectra, shown in Fig. 3.1(c), exhibit two resonances with energy separation which depends on the MgO thickness. We calibrate the MgO thicknesses as follow: 1 ML MgO corresponds to MgO patches whose FER spectra show a separation between the two peaks of ~0.69 V. We define the 2 ML MgO thick patches as regions with FER spectra whose peak separation is of ~0.44 V. The general trend, validated for thicker MgO thicknesses, is that the thicker the MgO layer, the smaller the separation between these two extremas in the FER spectra. Note that the Ag(100) substrate does not exhibit any feature in the 1 V to 3 V energy range. This calibration [53] differs by one layer from the one used in the work of Paul *et al.* [81], where our 1 ML assignment corresponds to their 2 ML assignment. But, as we will show in the following, our method to determine the adsorption site of adatoms on MgO is independent of the calibration of monolayer used.

Atomic resolution on the MgO layers is obtained by approaching the STM tip closer to the sample surface, *i.e.*, by decreasing the bias voltage while increasing the tunneling current. This leads to atomically resolved images of the surface as shown in Fig. 3.1(b) for 2 ML MgO, where the square lattice of round protrusions reflects the symmetry of the substrate. The period of

---

[1]The lattice constante of the bulk MgO(100) is of 2.98 Å, to be compared to 2.89 Å for Ag(100).

2.90 ± 0.03 Å agrees well with the Ag(100) nearest neighbor distance of 2.89 Å. This implies that only one ionic sub-lattice (Mg or O) is resolved [53, 97], assuming that we do not image the underlying Ag surface atoms. The unique experimental fact attesting that under atomic resolved conditions the STM tip should be sensitive to the MgO surface directly relates to the tunneling current one needs to achieve such conditions. We observed that the higher the MgO thickness, the lower the tunneling current in order to get atomic resolution. If the STM would always scan the surface Ag atoms trough the MgO gap, this would require higher tunneling current as the MgO thickness is increased, contrary to our experience. The origin of the atomic protrusions is still a matter of debate [45, 98, 99] and cannot at the time be attributed neither to O nor to Mg. Nevertheless we will demonstrate that a combination of different pieces of information from experiments provides a way to establish the origin of the atomic contrast.

Ca-doped MgO films are obtained by co-evaporating Ca with Mg during the MgO growth. The idea is that the Ca atoms replace Mg in some lattice sites. These are easily imaged with STM as shown in Fig. 3.2(a). For our employed Ca-doping of the order of 0.5% practically all the Ca atoms are sufficiently far from each other to appear as individual protrusions. For the employed tunnel parameters, Ca atoms are imaged as small protrusions of 73 ± 2 pm and 61 ± 2 pm on 1 and 2 ML MgO respectively, where the uncertainties are taken as the standard deviation of the object's apparent height (88 and 50 objects respectively). Close inspection of the histogram of Fig. 3.2(b) shows that on 1 and 2 ML MgO, the apparent height of the Ca protrusions follows a similar trend, *i.e.*, a region which concentrates the majority of the data points plus a tail of objects with a slightly larger apparent height. The latter objects correspond to two or more Ca protrusions which are separated by few atomic sites only (less than five) and are not resolved as multiple protrusions.

The narrow apparent height distribution found for both MgO thicknesses indicates that all the Ca atoms are on identical sites on each MgO thickness. In addition, the very similar apparent height found for 1 and 2 ML MgO suggests that Ca occupy the same site independently of the MgO patch thickness. We attribute the slightly lower apparent height for Ca atoms on 2 ML MgO to the lower conductance on these regions, for the employed tunnel parameters. Therefore, Ca protrusions must be located at the topmost MgO layer. Surely that in the hypothesis they would be buried inside the MgO layer, they would appear with a clearly different apparent height and be located on the other lattice site, which is not corroborated by our findings. Indeed, Fig. 3.3(a) shows a magnified region of the central part of the Fig. 3.2. The overlaid lattice of red and green circles represents the MgO top layer lattice of O and Mg atoms. This lattice orientation and spacing is extracted from an atomic-resolved image of the same MgO surface free of Ca atomic protrusions. A magnesium atom of the lattice is superimposed on one Ca protrusion and all the others ones are observed to sit on another Mg lattice position, independently on the local MgO thickness. The associated assumed model for the topography of the surface is reported on the Fig. 3.3(b). The MgO layer is topographically flat, with the Ca protrusions in the topmost layer, and differences between 1 and 2 MgO layers originates only from the MgO thickness grown toward into the Ag(100) substrate. We will show that the STM image [Fig. 3.3(a)] supports this interpretation. The shape of the frontier between the
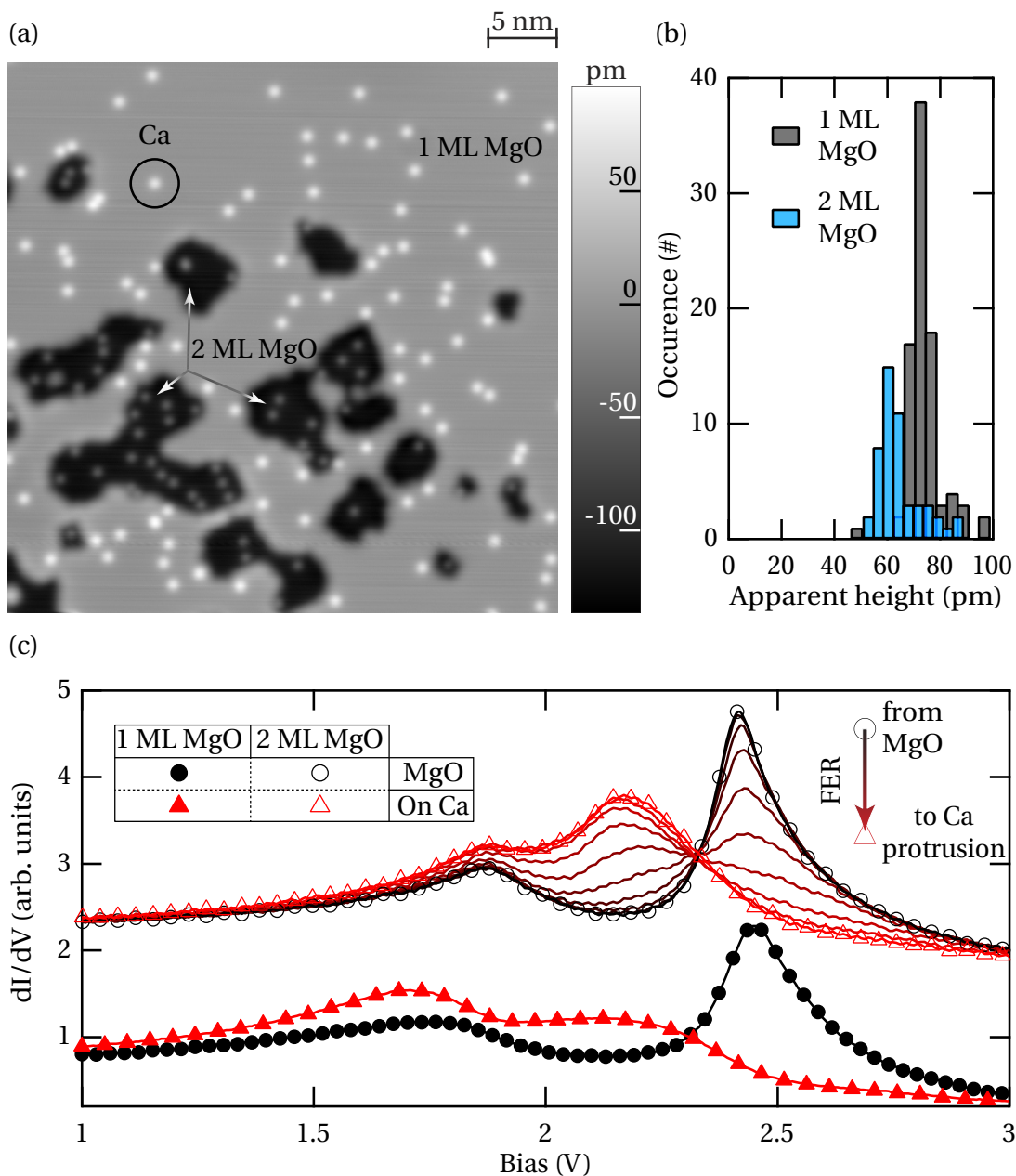
Figure 3.2 – (a) STM image of 1 and 2 ML MgO with the substitutional Ca atoms appearing as protrusions ($V_t = -515$ mV, $I_t = 100$ pA, $T_{STM} = 5$ K). Note that the apparent height of the MgO layers is inverted relatively to their thickness. (b) Histogram of the apparent height of the Ca protrusions in (a). (c) FER spectra of MgO and of one Ca protrusion on 1 ML (filled symbols) and 2 ML (open symbols) thick MgO layers, recorded on another region than in (a); Setpoint condition on 1 ML: $V_t = 1$ V, $I_t = 100$ pA, $V_{mod} = 10$ mV; On 2 ML: $V_t = 0.5$ V, $I_t = 100$ pA, $V_{mod} = 10$ mV. The upper curves for 2 ML MgO are offset for clarity. Curves for 2 ML MgO with intermediate color between red and black show the change in FER while recorded gradually closer to the Ca protrusions. Adapted with permission from [92].

1 and 2 ML MgO region is smooth and irregular. This is compatible with the shapes that a Ag(100) step can adopt. At variance, large MgO islands of a given thickness tend to adopt square shapes, as we can see on the Fig. 3.1(a). If the second MgO layer of Fig. 3.3(a) would have been topologically on top of the first layer, then one would have expected square frontiers between both layers, and that is not what is observed. Therefore we propose that the MgO layer of Fig. 3.2(a) is topologically flat and that the Ca atoms segregate to the topmost layer during the MgO growth.

Surface segregation of Ca in MgO crystals is further supported by the literature [100–103]. Indeed, upon annealing around 1200 K of Ca-rich MgO crystals, Mg atoms at the surface are replaced by Ca, diffusing from the bulk of the material. In our case, we recall that small MgO thicknesses are used in the experiments. The growth temperature is indeed of 770 K, but that is enough to get MgO islands topologically flat over hundred of nanometers. Therefore the temperature during the growth of the MgO is high enough to give mobility to the surface Ag atoms and to the MgO layers. Including the Ca in the growth would not change the overall situation, *i.e.*, thermal energy would be already enough to get the segregation of Ca to the topmost MgO layer. Indeed, we learn from P. Tasker *et al.* [101] that Ca atoms location at the MgO-vacuum interface is energetically favored. For all these reasons, we assume that all the Ca adatoms segregate to the surface during the growth. Therefore, the Ca atoms always mark Mg lattice sites in the topmost layer, independently of the MgO thickness.

The first resonance, at 1.8 eV and 1.9 eV for 1 and 2 ML MgO, respectively, in the FER spectrum of MgO layers of Fig. 3.2 can be traced back to the MgO-Ag interface state [53]. The second one around 2.4 eV and 2.5 eV for 1 and 2 ML MgO, respectively, is related with the work function of the sample [54]. Interestingly, we observe that the FER spectra on the Ca atoms on each MgO layer predominantly modifies the second resonance. Figure 3.2(c) shows for comparison spectra on MgO (round markers) and Ca (triangular markers) on 1 and 2 ML MgO (filled and open markers respectively). On the Ca protrusions, the second resonance for MgO is suppressed in favor of another one at lower energy. The energy separation between the two FER maxima when recorded on top of the Ca protrusion, on 1 and 2 ML MgO, are of 0.4 eV and 0.3 eV, respectively. This clearly contrasts with the values reported for the MgO, see Fig. 3.1(c). The series of FER spectra on 2 ML MgO of Fig. 3.2(c) are recorded successively on a line crossing the Ca protrusion. The black spectra is taken on the MgO substrate and then the STM tip is moved gradually toward on top of a Ca protrusion while still recording FER spectra. Clearly the second MgO resonance reduces in intensity while the one specific to the Ca protrusion gradually emerges at lower energy. Such series of spectra was not recorded on 1 ML MgO, but the same behavior is expected for the second resonance. In addition the first resonance is much more affected by the presence of the calcium than on 2 ML case, as it is shifted by 0.07 eV towards lower energy, at 1.7 eV.

The easier and most straightforward way to determine the adsorption site of any adatom adsorbed on the MgO thin film surface would take advantage of the knowledge of the atomic

contrast. Indeed, one could manage to record on the same STM image the atomic resolution of the MgO layer and also scan the adsorbate with standard scanning conditions. Thus one would only compare the apex location of the adsorbate to the MgO atomic contrast. Nevertheless, and even if theoretical works tried to explain the origin of the atomic contrast on MgO, this method is unusable, simply from experimental issues. Figures 3.4(a) and (b) show atomically resolved images of nearby regions of the same terrace of 1 ML Ca-doped MgO. The only difference between them is that they were recorded with two hours of interval, with some FER spectra recorded in the meanwhile. Clearly Fig. 3.4(a) and (b) do not have the same kind of atomic contrast because the regions around the Ca atomic protrusions are not identically resolved. The use of very similar tunnel parameters suggests that the change of contrast corresponds to a different apex of the STM tip. It is improbable to interpret the atomic contrast of MgO from these observations; One cannot neither even define the location of the Ca atom from atomically resolved STM images of Ca-doped MgO. Indeed, in Fig. 3.4(a), in the surroundings of the Ca atoms positions (marked with red ellipses in the figure), the contrast has a complex feature with an atomic protrusion with smaller apparent height. On Fig. 3.4(b),
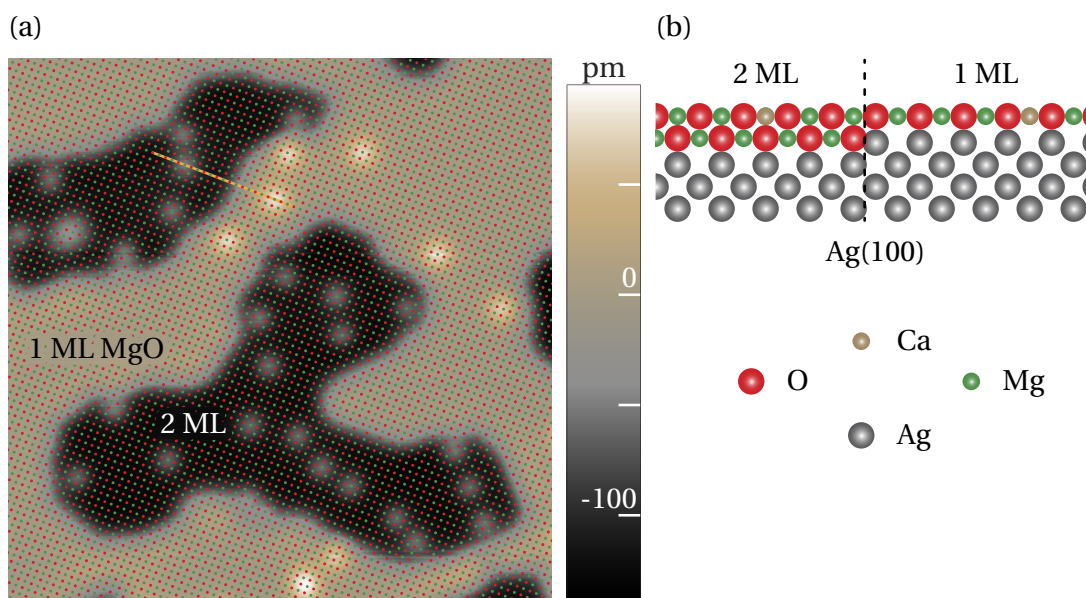
Figure 3.3 – (a) Magnified STM image of the central region of Fig. 3.2. All the protrusions are due to the Ca incorporation in the topmost MgO layer. The overlaid lattice of red (O) and green (Mg) circles represents the MgO lattice. All the Ca protrusions are located on the same lattice site, *i.e.*, on a Mg lattice position ($V_t = -0.5$ V, $I_t = 100$ pA, $T_{STM} = 5$ K). (b) Side-view schematics of the topography of the MgO layer along the orange line in (a). The second MgO layer is grown inside the Ag(100) substrate. Here we represented "1 ML" and "2 ML MgO" as one and two MgO(100) atomic planes, but recall that our definition of the MgO monolayer cannot certify that it corresponds to a physical layer of MgO. The idea of the schematics is to get known that the labelled "2 ML" region is one MgO layer thicker than the "1 ML" one and that in this case the growth take place inside the Ag(100) substrate.
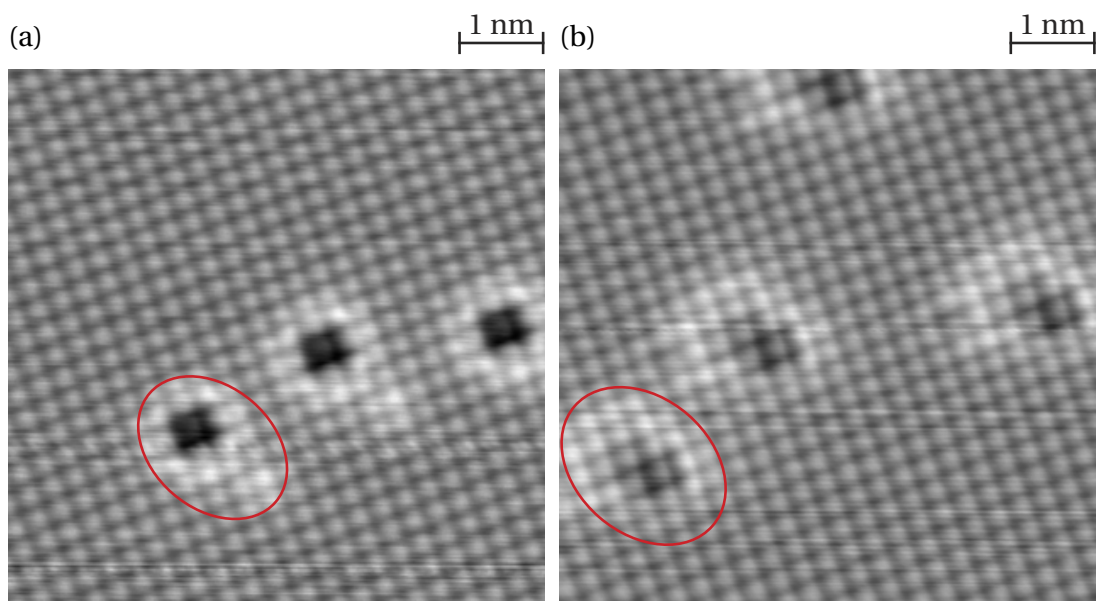
Figure 3.4 – STM images of the same region recorded under very close tunneling conditions. Atomic resolved images contrast of Ca-doped MgO highly depends on the STM-tip apex. (a) Ca atoms affect the atomic contrast by lowering significantly a unique atomic protrusion for each Ca atom while (b) Ca atoms have negligible effect on the atomic contrast. [(a): V_t = 5 mV, (b): V_t = 4 mV, both: I_t = 10 nA, T_{STM} = 5 K].

at the position of identicals Ca atoms another complex feature exists but differing from the one encountered in (a). But the shape of the atomic protrusions do not differ between (a) and (b) images. We therefore conclude that atomically resolved images of the Ca atoms are highly dependent on the STM tip apex, and are therefore of no utility at the time to interpret the MgO atomic contrast, neither to help in determining adsorption site of adsorbates. Note however that interpretation of the atomic contrast will finally be achieved by circumvent the problem. That will be presented at the end of section 3.3.

We characterized thin MgO films grown on Ag(100) substrate as well as the effect of Ca dopant incorporation. Atomic resolved images of the (Ca-doped) MgO substrate cannot be easily interpreted. Indeed, we are unable to define which of the two constituents of the MgO surface appears as protrusions in atomically resolved STM images. Even imaging with atomic resolution a Ca protrusion does not help in this task, see Fig. 3.4. Nevertheless we gave elements supporting the hypothesis of Ca segregation to the uppermost MgO layer. Since Ca would be located at the lattice position of Mg, Ca protrusions in STM images are markers for the Mg sublattice positions of the topmost MgO layer. We will exploit this information in section 3.3, right after characterizing the Ho/MgO(100)/Ag(100) system.

3.3 Determination of the adsorption sites of Ho adatoms on MgO
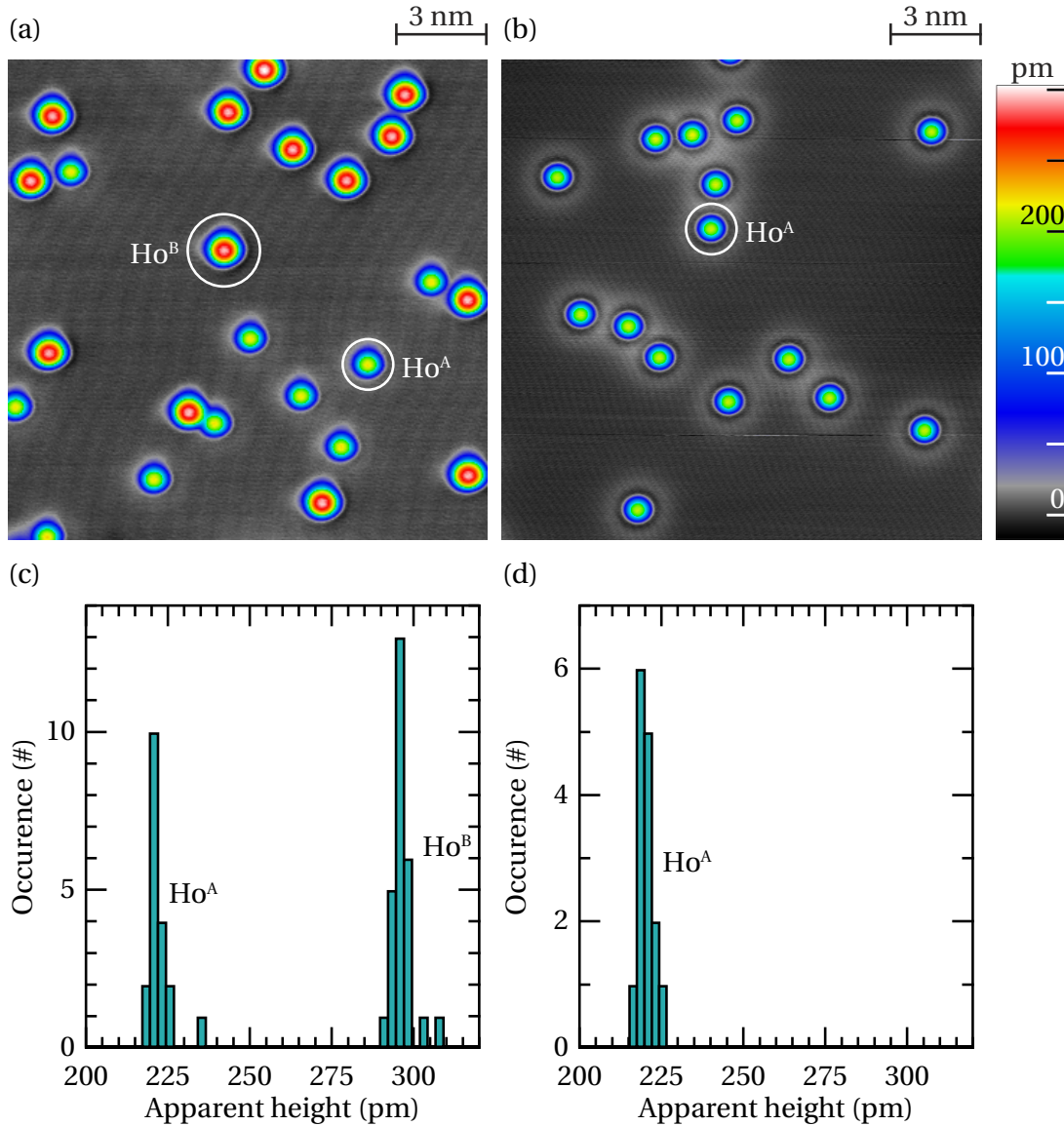
Figure 3.5 – STM images of (a) 1 ML and (b) 2 ML undoped MgO after the adsorption of 0.5% ML of Ho. Two species, Ho^A and Ho^B, are discerned by their apparent heights of 222 ± 4 pm *vs.* 296 ± 3 pm. ($T_{dep} \approx 10$ K, $V_t = -20$ mV, $I_t = 20$ pA, $T_{STM} = 5$ K). (c) and (d) Histograms of the apparent height of the objects in (a) and (b), respectively. Ho^A objects have a very similar apparent height on both MgO layers. Adapted with permission from [92].

Ho atoms are evaporated on the sample from an *e*-beam evaporator. A Ho rod is heated until Ho atoms are thermally evaporated from the rod. For the evaporation, the doors of the cryostat are open and the sample is exposed to a 300 K radiation. Therefore its temperature raises up to an estimated temperature of $T_{dep} = 10$ K during the evaporation. Right after the evaporation

	1 ML MgO		2 ML MgO	
	Abundance (%)	Number of atoms	Abundance (%)	Number of atoms
Ho^A	$35.8^{+1.6}_{-1.5}$	338	$91.5^{+1.6}_{-1.8}$	260
Ho^B	$64.2^{+1.5}_{-1.6}$	608	$8.5^{+1.8}_{-1.6}$	24

Table 3.1 – Number of Ho^A and Ho^B atoms counted on 1 and 2 ML MgO over many STM images and the corresponding abundances ϑ^O and ϑ^{br}.

which lasts about a minute, the doors of the cryostat are closed and the sample cools down to liquid He temperature (T_{STM} = 5 K) in a time of the order of minutes.

Figures 3.5(a) and (b) show a 1 and 2 ML MgO region, respectively, with a Ho coverage of 0.5%±0.1% ML. The Ho coverage is independent of the MgO thickness within the uncertainties. On 1 ML MgO, two species with two characteristic apparent heights coexist. These two species are not a hydrogenated version of the same adatom [104]. To check that, we exposed the sample to 21 L of H_2 and no modification in the proportion, nor apparent height, was detected. Note that this dose was enough to hydrogenate the Ho adatoms adsorbed on bare Ag(100). We define as Ho^A the objects with the smaller apparent height of 222 ± 4 pm. The other objects, Ho^B, are characterized by a larger apparent height of 296 ± 3 pm. On 2 ML MgO, almost exclusively Ho^A species occur, with the same apparent height according to the uncertainties. In very rare cases one encounters an Ho^B adatom on 2 ML MgO. The abundance ϑ^O and ϑ^{br} of Ho^A and Ho^B, respectively, as well as the number of adatoms counted, for each of the MgO layers, is reported in Tab 3.1. Uncertainties are calculated according to the constraint that Ho atoms should be shared between Ho^A and Ho^B species following a binomial distribution, *i.e.*, that $0\% \leq \vartheta^{+\Delta\vartheta^+}_{-\Delta\vartheta^-} \leq 100\%$. They correspond to 68% confidence intervals[2].

Determination of the adsorption site of the Ho adatoms on MgO thin films is achieved by a combination of two independent measurements. Its result is shown in Fig. 3.6. It depicts a single MgO layer with substitutional Ca atoms, as well as both adsorbed Ho species. The Ca atoms appear as faint spots with an apparent height of 59 ± 2 pm in the conditions of the measurement, while Ho^A and Ho^B apparent height is of 179 ± 1 pm and 257 ± 2 pm. The tunneling conditions yielding atomic resolution move the Ho atoms. Therefore we imaged a bare MgO spot of the same sample with atomic resolution from where we extracted the MgO lattice constant and orientation. The lattice is then overlaid onto the Fig. 3.6 and one of its Mg atom is aligned onto one substitutional Ca protrusion. All other Ca species (12 in total) fall exactly on a Mg site, level lines guide the eye to convince. Comparison of the Ho atoms position relatively to the MgO lattice reveals their adsorption site. From that we conclude that Ho^A species adsorbs on top of O (all the 9 of them are located on an O lattice position) and Ho^B adsorbs on a bridge site halfway between two O (or Mg) lattice positions (again, all the

---

[2]We calculated the uncertainties from the maximum likelihood function of the experimental results for each counting. The standard development of this method can be found in reference [130], chapter 9.3.2 *Non-parabolic log-likelihood functions*. The method generates uncertainties that will never go beyond (under) 100% (0%).

11 Ho^B share equivalent lattice position). All the different Ho and Ca species adsorb each on one type of lattice site, illustrating the precision of the method. Finally, on 2 ML MgO, the preferred adsorption site is therefore on top of oxygen, as the majority species is Ho^A.

The key point to achieve this level of precision is to let the STM measure the same region enough time to suppress the piezo creep. In our case, the timescale of this stabilization is estimated to 30 minutes. Therefore we are able to superimpose one measurement of the MgO lattice directly on top of a conventional STM image with the adsorbates. Fine adjustments are still allowed. Adaptation of the angles for the lattice directions of some degrees were sometime necessary, as well as adjustment of the order of percent for the lattice parameter. These issues are due to the technique[(3)]. Images recorded in the same conditions may show very small distortions, mainly due to the thermal drift. Nevertheless, the superposition of the grid originates from STM measurements and is clearly not a fit.

The very different abundances of both Ho species on 1 and 2 ML MgO is attributed to the MgO thickness dependent dissipation of the adsorption energy. On 1 ML, the abundance of the species, see Tab. 3.1, reflects the one of their adsorption site since there are two bridge sites per MgO(100) unit cell (one for O). This is compatible with statistical growth, where the atoms stick at their site of impact, irrespectively of the adsorption energy. This hypothesis is described in the appendix A.1, but note that this explanation is clearly not the unique possibility at all, and possibly not the best. On 2 ML MgO, the clear preference for O sites implies adatom motion, independently of the fact that the 2 ML region is an extended 2 ML film or an isolated spot on the 1 ML MgO film. Thermal mobility can be ruled out since both species on both MgO thicknesses are immobile for hours up to 58 K at least. Therefore the Ho atoms must exhibit transient mobility, at least for one atomic jump from a bridge site to the adjacent O one [105]. The fact that this occurs more readily on 2 ML MgO than on the monolayer can be related to the dissipation of the adsorption energy via electron-hole pair excitation in the metallic substrate [39, 106], which would be much more efficient on thinner MgO layers. We will come back to these considerations later, chapter 4 is entirely devoted to discuss this point.

3.4   Manipulation of the Ho adsorption sites

In order to explore other adsorption configurations, we carried out STM manipulations of the Ho/MgO system by applying voltage ramps with the STM tip placed above the Ho atoms. To prevent major modifications of the probed area by the high electric fields generated, the voltage is ramped while keeping the feedback loop closed. In this situation, the tunneling current remains constant while the STM tip retracts smoothly. Therefore, abrupt changes in the vertical position of the tip evinces a modification or a displacement of the probed atom [82]. Figures 3.7(a-c) illustrate the result of this process on three selected Ho atoms on

---

[(3)] Please note also that from sample to sample, the high symmetry directions of the surface MgO lattice can change, as evidenced by all the following images in this thesis. This is simply due to the change in the scan angle during the STM image recording.
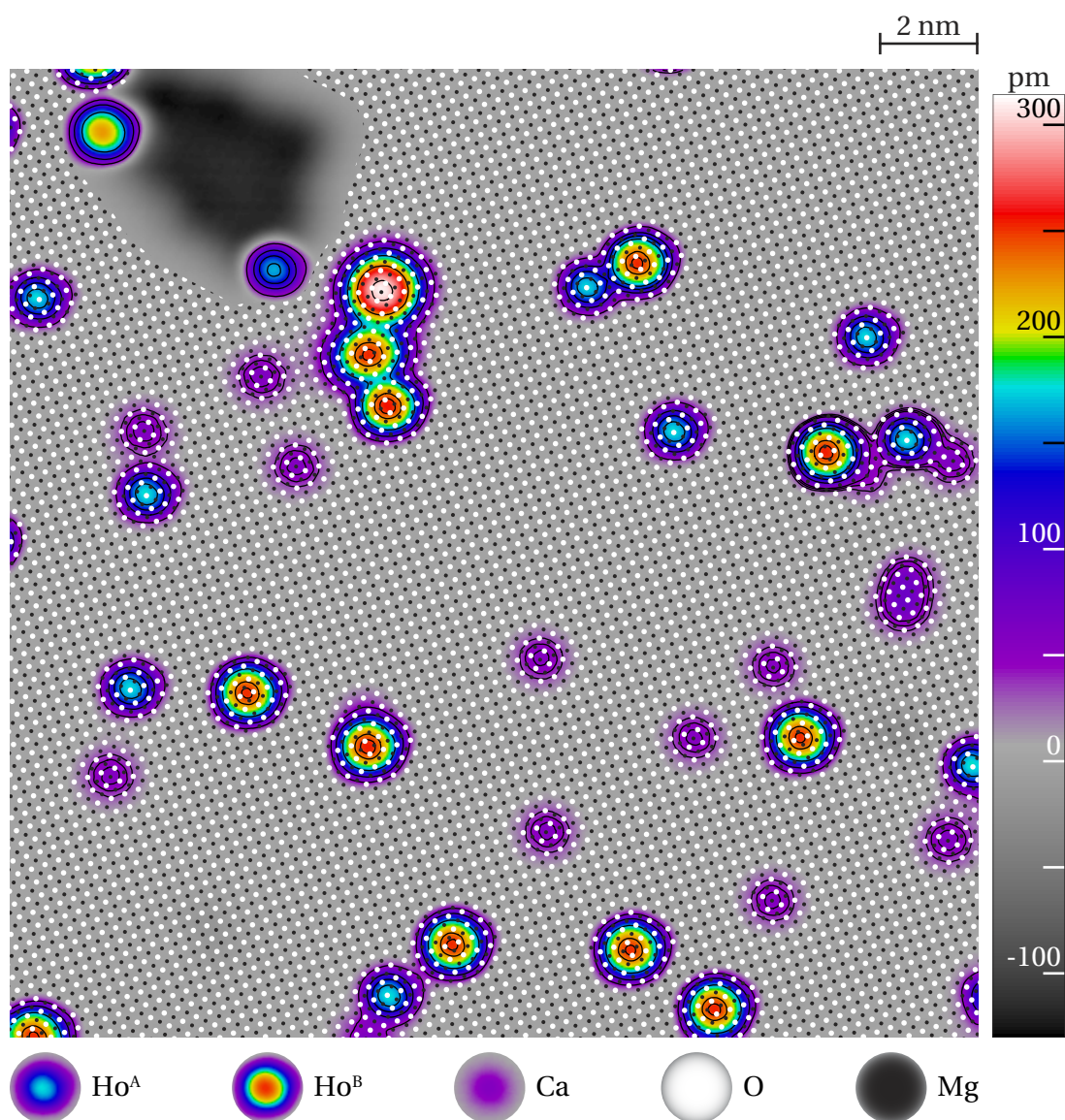
Figure 3.6 – STM image of 1 ML MgO grown with 0.5% ML Ca doping and the same amount of Ho atoms adsorbed onto it. The orientation and spacing of the overlaid MgO lattice were determined from an atomically resolved image recorded on a bare MgO spot of the same sample. This lattice was then translated to bring one of its Mg atoms in coincidence with the apex of one of the Ca species. Level lines overlaid on the atomic protrusions are guide to the eye, showing that each apex of Ca protrusions lies at the center. ($V_t = -20$ mV, $I_t = 20$ pA, $T_{STM} = 5$ K).

1 ML MgO. Ramping the bias up to -1 V on top on a Ho^A atom, see Figs. 3.7(a) and (f), switches them to Ho^B. The atoms of Fig. 3.7(b) have all the same apparent height and are adsorbed on a bridge site. The bias voltage at which the adatom change in appearance can vary in a range of 0.2 V, as shown in Fig. 3.7(f). Thus not all the atoms switch in appearance at exactly the same bias voltage.

The same ramping procedure with inverted polarity on top of an Ho^B atom transforms it into an Ho^A. Therefore, Ho^A and Ho^B atoms can be transformed back and forth. This permits to prepare the Ho/MgO system in a way suitable for electron spin resonance (ESR) experiment, as used in reference [37]. For example, as 1 ML MgO predominantly holds Ho^B adatoms, we can transform them into Ho^A species with a positive voltage ramp. On 2 ML MgO, where Ho^B
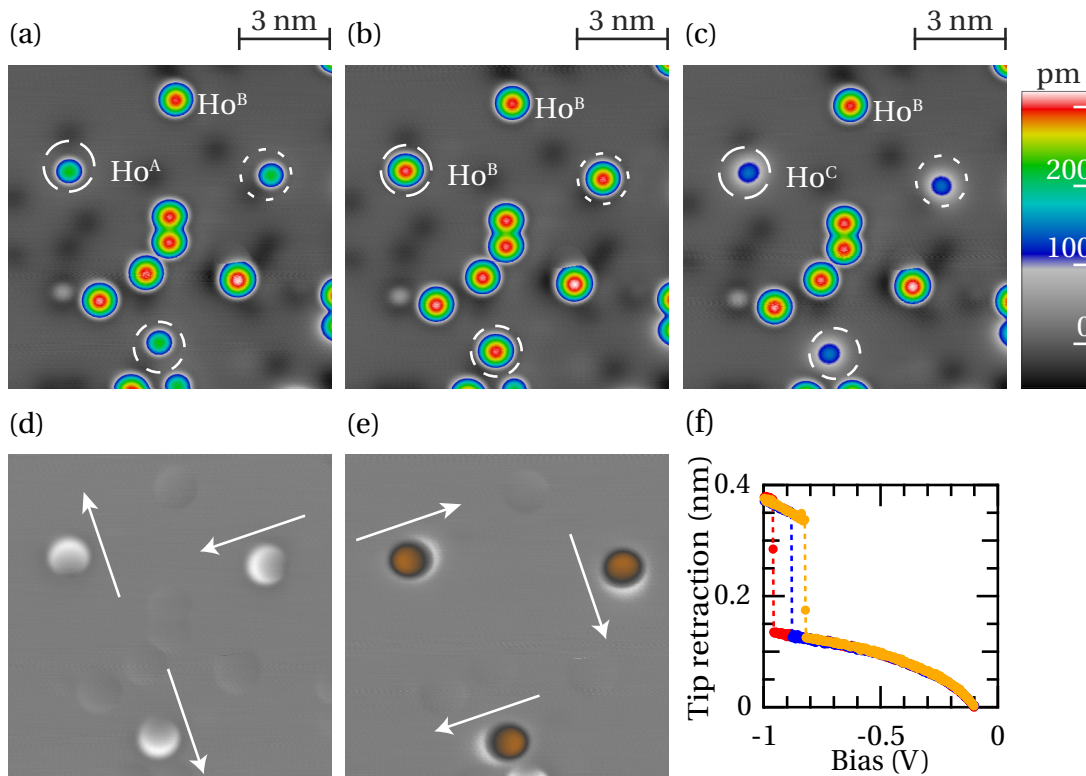
Figure 3.7 – STM images of Ho atoms on 1 ML MgO. Atoms indicated with dash-circles are successively transformed from (a) Ho^A to (b) Ho^B, and finally to (c) Ho^C by applying negative voltage ramps, see text for details (a-c: $V_t = -100$ mV, $I_t = 20$ pA, $T_{STM} = 5$ K). (d) Subtraction of image (a) from (b) using the unchanged atoms for precise alignment. (e) Subtraction of (b) from (c). The white (brown) color indicates levels above (below) the zero plane. Arrows indicate the directions of the atom displacements. (f) Negative voltage ramp used on image (a) to transform the three Ho^A atoms into Ho^B. Red, blue and orange curves correspond to bias ramps on the upper-left, upper-right and lower dash-circled Ho^A adatoms in (a). Adapted with permission from [92].
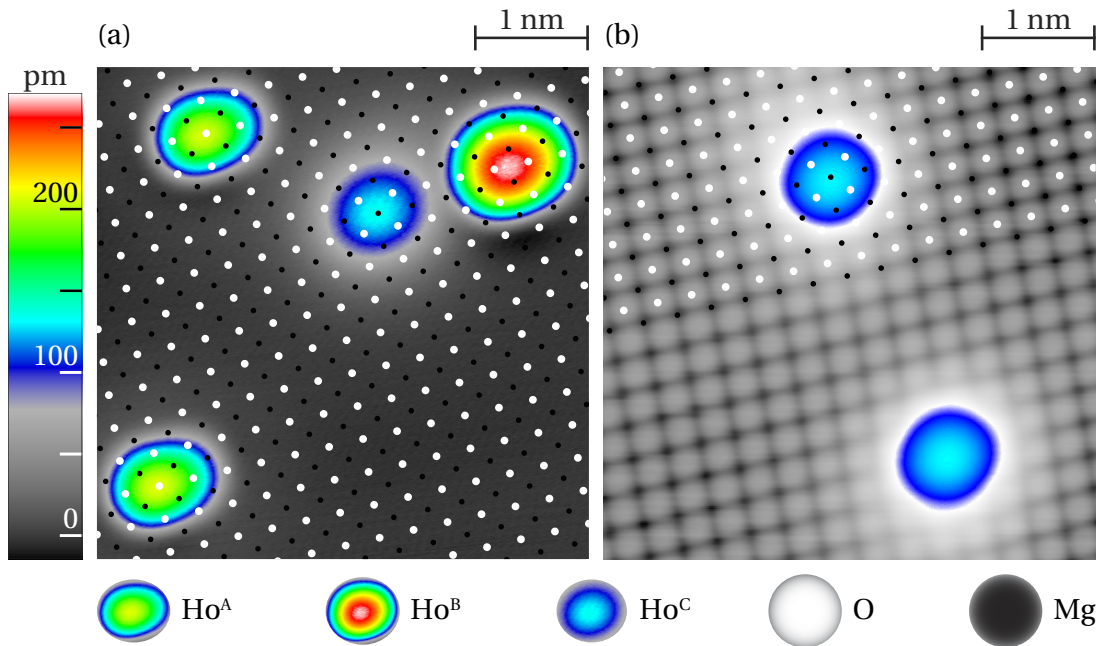
Figure 3.8 – (a) STM image of all three Ho species on 1 ML MgO ($V_t = -20$ mV, $I_t = 20$ pA, $T_{STM} = 5$ K). Ho^C has an apparent height of 141 ± 3 pm and is adsorbed on top of a Mg atom. The MgO lattice of white and black circles, standing for O and Mg atoms, is inferred from an atomically resolved image of the bare MgO surface. Note that the apparent elongated shape of the protrusions originates from the STM-tip convolution. (b) Atomically-resolved image of two Ho^C atoms on 2 ML MgO. The MgO lattice (O: white, Mg: black) shows that O atoms appear as protrusions ($V_t = -20$ mV, $I_t = 5$ nA, $T_{STM} = 5$ K). Only half of the MgO lattice is shown to better distinguish the atomic protrusions in the lower part. A gaussian blur of 0.016 nm in standard deviation was applied to image (b) in order to remove small spiked lines. Adapted with permission from [92].

atoms are very rarely found, one can make them appear by transforming the Ho^A ones, since similar ramping procedures hold on 2 ML MgO.

Ramping further a negative voltage ramp up to -1.2 V on top of Ho^B adatoms irreversibly switches them into a new Ho^C species, see Fig. 3.7(c). With an apparent height of 141 ± 3 pm, this species appears much smaller than Ho^A or Ho^B. Ho^C adatoms are remarkably stable. Voltage ramps up to a bias of ± 10 V have no effect on them, while Ho^A or Ho^B atoms are transformed or desorbed under these conditions.

Using the unchanged atoms as reference, we identify the possible displacement of the manipulated adatoms by subtracting subsequent images. Figure 3.7(d), result of the subtraction of (a) from (b), shows asymmetric spots at the positions of the three dash-circled atoms. The white arrows point into the direction of the displacement, thus indicating that the three switched atoms moved along two perpendicular directions. These are the two possibilities for hopping from an O to a bridge site. Figure 3.7(e) is obtained after subtracting (b) to (c). Interestingly, we observe that the switched atoms moved along two perpendicular directions but also per-

pendicular to their first switching direction, compare to Fig. 3.7(d). This evidences an overall movement along the bridge-Mg direction.

Figure 3.8(a) shows a 1 ML MgO region with all the three Ho species, with the Ho^C created using the bias ramping procedure. The overlaid lattice of O and Mg atoms was determined with the same method used for Fig. 3.6. By aligning the O lattice position on top of the Ho^A species, we verify that Ho^B adsorbs on a bridge site, and infer that Ho^C is located on top of a Mg lattice site.

3.4.1   Results from DFT calculations for Ho/MgO(100)/Ag(100)

Experimental investigations with the STM permit to determine the adsorption site of the various Ho species. Nevertheless, no insight can be brought explaining why the different Ho species coexist. DFT calculations of Ho on 1 and 2 ML MgO would help in answering this question. Željko Šljivančanin, and his collaborator Srdjan Stavrić, calculated with DFT the adsorption configurations of Ho on 1 ML and 2 ML MgO/Ag(100), using the method described in reference [80]. Results are reported in Fig. 3.9 for 1 and 2 ML MgO. The reference for the energy is taken for the most favorable species. Positive binding energies signify that they are less favorable. On 2 ML MgO, DFT finds in agreement with our observations that Ho adsorbs most favorably on top of O. Adsorption on the bridge site is higher in energy and that explains the lower abundance of Ho^B on 2 ML MgO, see Tab. 3.1. In addition, the Ho^C species appears to be the less favorable. This adsorption configuration requires to push the Mg atom down into the MgO layer, see Fig. 3.9(f). This is in contradiction with our experiment which shows that Ho^C species are also stable on 2 ML MgO. DFT results for 1 ML MgO are in better agreement with the experiment where Ho^C is predicted to be the most stable species. Again, this adsorption geometry requires to push down to the Ag substrate the Mg atom, as shows Fig. 3.9(a), but then this better stabilizes the Ho atom. Our experiment effectively observes this remarkable stability. Nevertheless, such adsorption configuration could only be accessed after STM manipulations on the Ho adatoms, as described in section 3.4.
It is worth to stress on the fact that more complete comparison with DFT calculation could be achieved by taking into account the effect of the O pressure for a partial layer of O at the MgO-Ag interface, as proposed by Smerieri *et al.* [107]. Naive interpretation would be that this new interface would give more space for the MgO lattice relaxation under the adatom and perhaps Ho^C species would become the most favorable also on 2 ML MgO.

Energy differences relatively to the most favorable configuration, ΔE, are reported in Fig. 3.9. In addition, Δq, the charge transfer to the Ho atom are in agreement with the experiment. Indeed, switching an Ho^A adatom to Ho^B and then Ho^C requires increasingly higher negative voltage. With negative bias, the electrons flow from the sample occupied states into the tip empty state trough the vacuum. Above a Ho adatom, this polarity contributes to extract
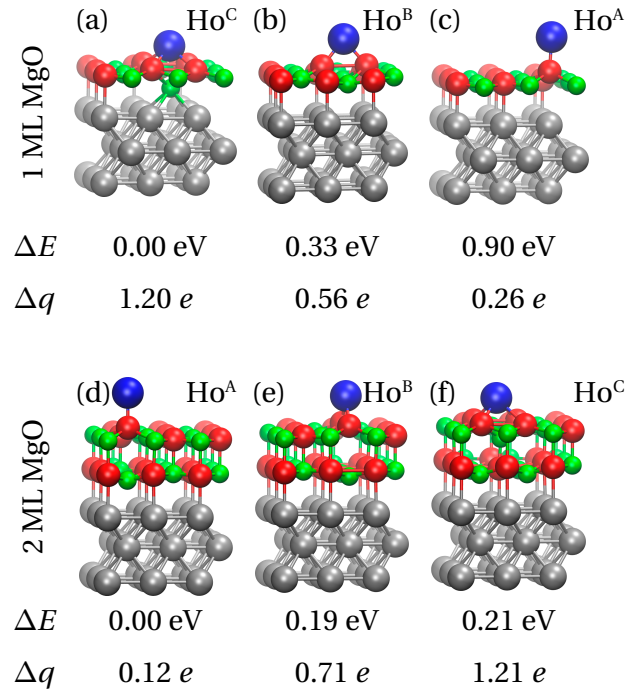
Figure 3.9 – DFT adsorption geometries of Ho adatoms on one (a-c) and two (d-f) MgO layers. Binding energy difference ΔE and charge transfer Δq (from the substrate to the adatom) for each configuration is also reported. The site with the highest binding energy was taken for reference. Positive ΔE stands for a decrease in binding energy. Blue: Ho; Red: O; Green: Mg; Grey: Ag. Adapted with permission from [92].

electrons from the atom, then changing its adsorption site and charge state. This was also observed for Au and Ag on NaCl(100) [82–84]. This indicates that the atom become more and more positively charged along the transformation sequence with the negative bias.

3.4.2 Origin of the atomic contrast on MgO

The remarkable stability of Ho^C adatoms permits to image it with tunneling conditions yielding atomic resolution on MgO. Figure 3.8(b) shows a 2 ML MgO region with two Ho^C adatoms and the atomic protrusions of the substrate. Knowing the adsorption site of Ho^C, we overlay the MgO lattice represented by white and black circles and identify the atomic protrusions as O atoms. As shown in section 3.2, this kind of atomic resolution is by far the most common in low-bias images of the MgO surface. Only in very rare cases are the Mg atoms imaged as protrusions. Usually to image the Mg we have an unstable tip and this atomic contrast does not survive too long under atomic resolution conditions. We still assume that imaging of the Mg atoms is possible because just after recovering a stable tip, the atomic protrusions are (mostly always) shifted by half of the MgO lattice constant, comparison made possible on STM images holding both kinds of resolution. This clarifies the controversial DFT results on the STM contrast observed on MgO/Ag(100) thin films [45, 98, 99].

3.5 Adsorption sites of other metal elements on MgO

The adsorption site of Ho adatoms has been determined using of Ca-doped MgO thin layers. Ho^A, Ho^B and Ho^C species were determined to adsorb on top of oxygen, on bridge site and on top of magnesium, respectively. The method of the Ca-doping can be applied to determine the adsorption site of any other adatom on MgO. Nevertheless, using an adsorbed species as marker for the MgO lattice site is a much more accessible experiment. To determine the adsorption site of other elements, one just has to co-evaporate Ho and the other element of interest. Using the same method as described in section 3.3 and Fig. 3.6, we will determine the adsorption site of new elements relatively to the Ho.

3.5.1 Erbium

Adsorption of Er on MgO is actually very similar to the case of Ho. Figure 3.10(a) shows a 1 ML MgO region with adsorbed Er atoms. At first sight, we recognize two species distinguishable from their apparent height, as the histogram of Fig. 3.10(b) evidences. The apparent height of the objects is of 224 ± 1 pm and 299 ± 1 pm. Few objects, with intermediate apparent height, are unidentified and could correspond Er adatoms on a defect site, or to contaminated adatoms. Similar to the Ho case, we label Er^A and Er^B the species with the smallest and largest apparent height, respectively. The grid overlaid onto the STM image in Fig. 3.10 is again extracted from an atomically resolved image of MgO. The grid is overlaid such as that one of its crossing is on top of an Er^A atom. All the others Er^A species fall exactly on the same lattice site and all the Er^B adatoms adsorb on a line connecting two crossings of the grid. This indicates that Er behaves as Ho on the MgO. A statistics over 127 valid objects adsorbed on 1 ML MgO indicates that abundances of Er^A and Er^B are $40.9^{+4.4}_{-4.3}$% and $59.1^{+4.3}_{-4.4}$%, with 10 objects removed from the statistics because of lack of identification. On 2 ML the statistics is relatively poor as we lack of data. Nevertheless, we can observe that the Er^A species is predominant on 2 ML MgO, following the same trend as Ho.

Transformation of Er adatoms has not been tested in the same way as for Ho. Interest was only about if Er^C could be produced. By pulsing the sample with voltages of 6 V, the Er adatoms undergo a transformation to a smaller species with apparent height of 136 ± 1 pm. These are identified as Er^C adatoms with similarity with the Ho case. The Er/MgO/Ag(100) system exhibits the same properties as the Ho/MgO/Ag(100) system from the adsorption point of view, that means that three species are stable on the MgO thin films and Er^A and Er^B objects can be transformed into Er^C.

Figure 3.10 – (Right) (a) STM image of Er adatoms adsorbed on MgO ($T_{dep} \approx 10$ K, $V_t = -200$ mV, $I_t = 200$ pA, $T_{STM} = 5$ K). (b) Histogram of the apparent height of the objects in (a). The two peaks correspond to two populations distinguishable from their apparent height. We identify as Er^A (Er^B) the objects of smallest (largest) apparent height. The lattice grid in (a) is extracted from atomically resolved images of the bare substrate and then tentatively put into coincidence of Er^A adatoms. It reveals that Er^A and Er^B do not share the same lattice site.

(a)

3 nm

(b)
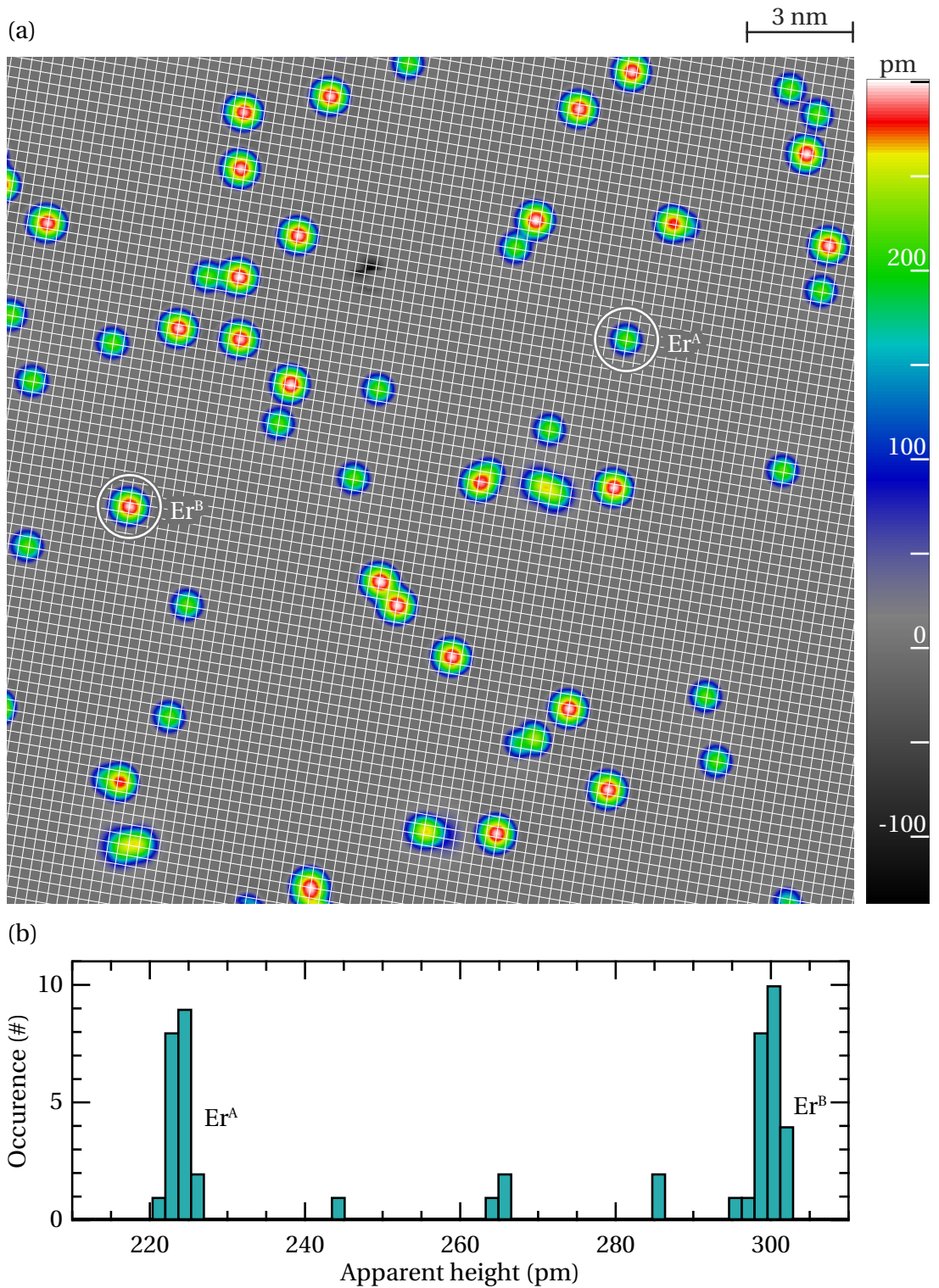
Figure 3.10 – (Caption at bottom of the previous page)

One way to determine the adsorption site of Er^A and Er^B species is to co-evaporate Ho and Er onto the same sample. Figure 3.11(a) shows a 1 ML MgO patch with Ho and Er atoms. At first sight, one distinguishes only two atomic species instead of the four expected. Under the tunneling conditions used for the STM image in Fig. 3.11(a), Ho^A and Er^A species have similar apparent height of about 220 pm, thus complicating their discrimination. The histogram of Fig. 3.11(b) shows a small double-peak feature, see the region with the orange rims, but we have not enough resolution to extract two different apparent heights from it. On the contrary, the histogram shows that Ho^B and Er^B could in principle be discriminated. Indeed, two peaks at 289 pm and 299 pm (with red and purple bar rim respectively), corresponding to Ho^B and Er^B, are visible. We are unable to identify the individual protrusion, but this does not inhibit the adsorption site determination of the Er species.

The overlaid lattice of white and black circles, standing for substrate O and Mg atoms, is again inferred from an atomically resolved image of the MgO substrate. One of the O atoms of the lattice is superimposed to the apex of one Ho^A or Er^A atom and all the other Ho^A or Er^A species fall exactly on an O site. Er^B and Ho^B species adsorb all on a bridge site. Again, even if we are not able to assign each object to Er or Ho species, we can still conclude that Er^A adsorbs on an O lattice site. The same holds for Er^B, which shares the same lattice site than Ho^B, namely, the bridge one.

Figure 3.12(a) shows a 2 ML region of MgO with Ho and Er atoms co-adsorbed. Two major atomic species are identified, as the two peaks of the histogram of Fig. 3.12(b) shows. We know from previous results, *i.e.*, section 3.3 and beginning of section 3.5.1, that on 2 ML MgO and more, Ho^A and Er^A species are mostly observed. Therefore, the two atomic species of Fig. 3.12(a) correspond to the Ho^A and Er^A species. Again, we cannot correctly label each object because one does not know which apparent height corresponds to Er or Ho. Nevertheless, the superimposed MgO lattice shows that they all share the same adsorption site. As Ho^A, one of the two species identified in the Fig. 3.12(a), adsorbs on O, then Er^A must adsorbs also on top of O.

The elongated objects of the Fig. 3.12(a) are identified as HoEr heterodimers. Samples with only Er (or Ho) adsorbed on 2 ML MgO did not exhibit such kind of objects. Following the similarities between the Ho/MgO/Ag(100) and Er/MgO/Ag(100) systems, we can assume that Er adatoms have also some transient mobility on 2 ML MgO. As Ho and Er are evaporated onto the substrate subsequently, it is likely that some Er atoms, while diffusing on the MgO surface, encounter an Ho adatom, forming an heterodimer. The remarkable precision of the measurements permits to reveal the adsorption configuration of the dimers. The Fig. 3.12 shows that they can be oriented following two perpendicular directions coinciding with the [110] direction of the lattice. We propose that each atom of the dimer adsorbs on top of two next-nearest neighbor O sites.

Figure 3.11 – (Right) (a) STM image of Ho and Er co-adsorbed on a MgO monolayer ($T_{dep} \approx 10$ K, $V_t = -20$ mV, $I_t = 110$ pA, $T_{STM} = 5$ K). (b) Histogram of the apparent height of the objects in (a). Distinction between Ho and Er adatoms is not possible. The lattice overlaid in (a) is extracted from atomically resolved images of the MgO. White (black) circles represent the O (Mg) atoms of the substrate.
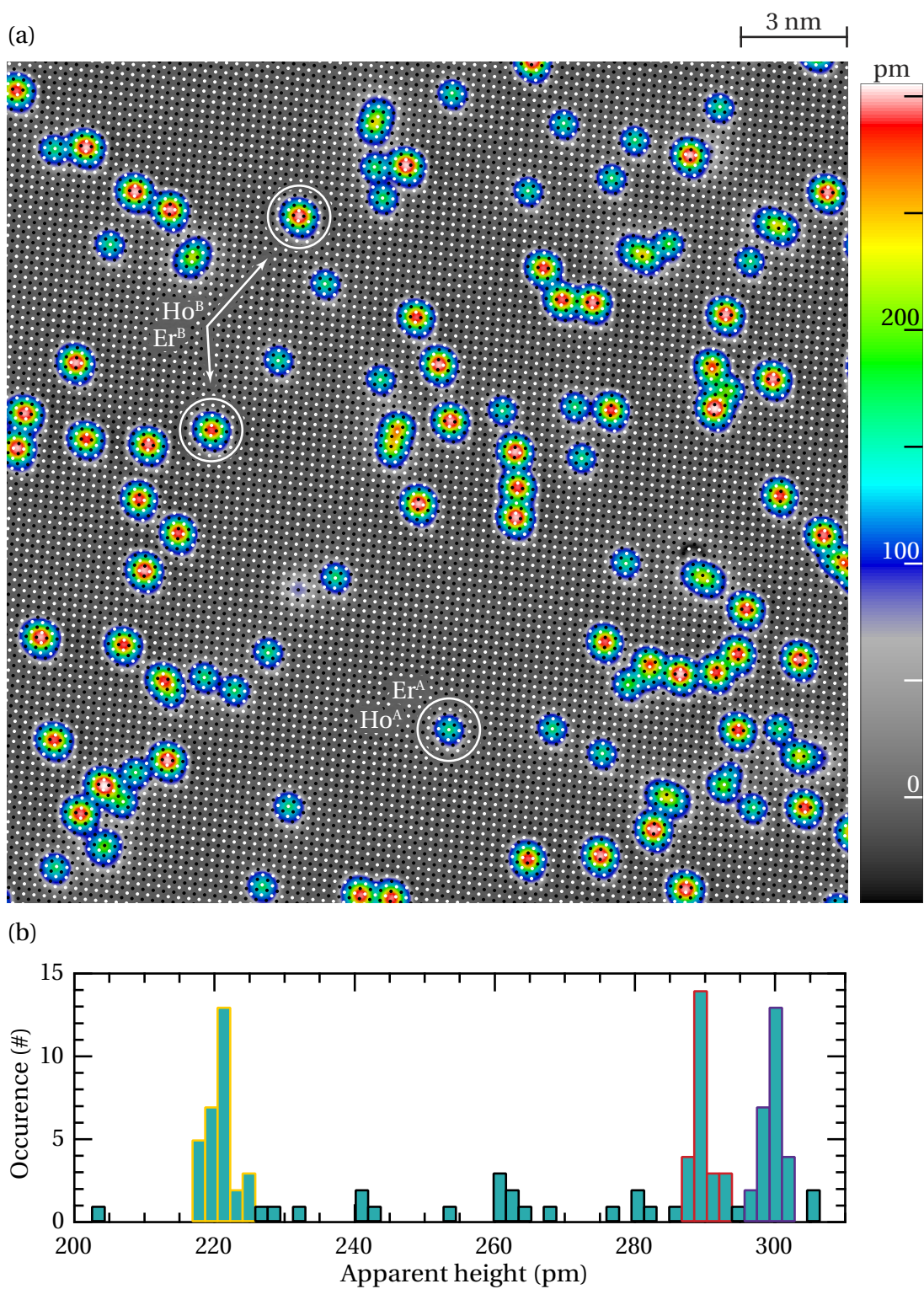
Figure 3.11 – (Caption at bottom of the previous page)
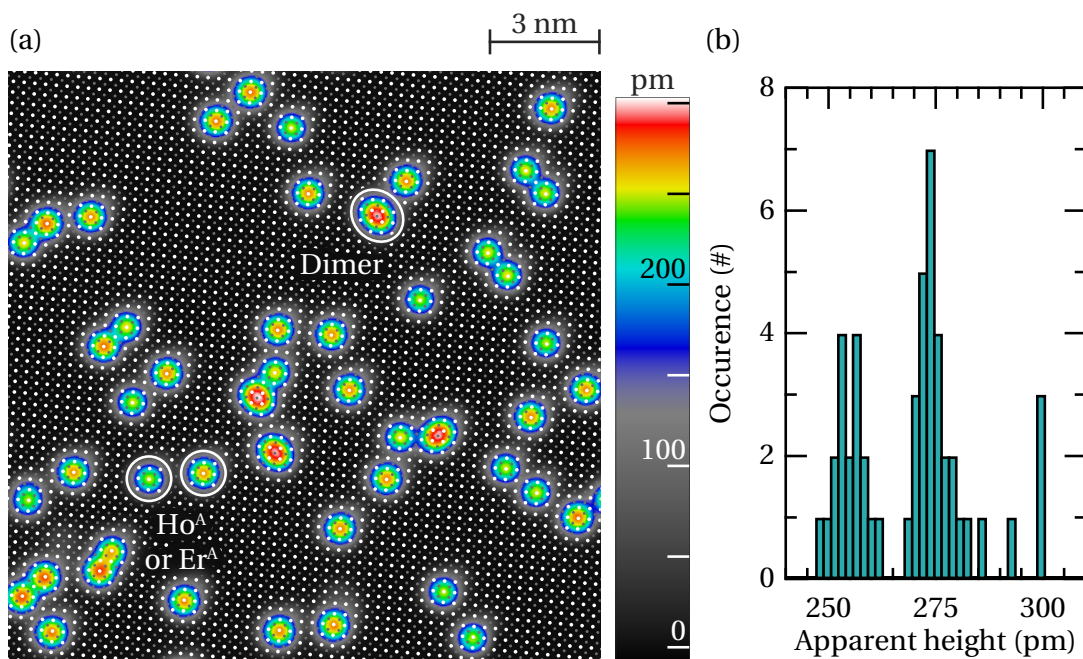
Figure 3.12 – (a) STM image of Ho and Er adatoms co-adsorbed on 2 ML MgO ($T_{dep} \approx 10$ K, $V_t = -20$ mV, $I_t = 200$ pA, $T_{STM} = 5$ K). (b) Histogram of the apparent height of the objects in (a). The lattice superimposed in (a) is still inferred from atomically resolved images of the substrate. Its O atoms (white circles) are put into coincidence with Ho^A and Er^A species. Grey circles of the lattice stand for the Mg atoms. Four objects are assigned to dimers because of their elongated shape.

The adsorption site of Er adatoms was determined on 1 and 2 ML MgO. We found two Er species, Er^A and Er^B, adsorbing on top of O and on a bridge site, respectively, with similarity with Ho. Er^C adatoms can also be created from the Er^A and Er^B species with STM-tip voltage pulses. Nevertheless, the apparent height of the Ho and the Er species is so close that we cannot label them individually on the STM images.

3.5.2 Cobalt

Holmium, as a marker for O and bridge sites of the MgO, can be used to determine the adsorption site of any other co-adsorbed atomic species. Nevertheless, straightforward discrimination between the adsobed atomic species is desirable. Co is an interesting atomic species because one can directly identify it with STS. Indeed, a spin excitation occurs at an energy of 57.7 meV [48], providing a direct way to identify the Co protrusions on STM images. If multiple adatoms coexist on the MgO substrate, STS provides a mean to identify any Co or Ho atom as Co will show spectroscopic features where Ho does not exhibit any.

Figure 3.13 shows a 1 ML MgO region with co-adsorbed Ho and Co atoms. We identify the smallest objects in apparent height to be the Co (173 ± 3 pm), the intermediate (228 ± 4 pm)
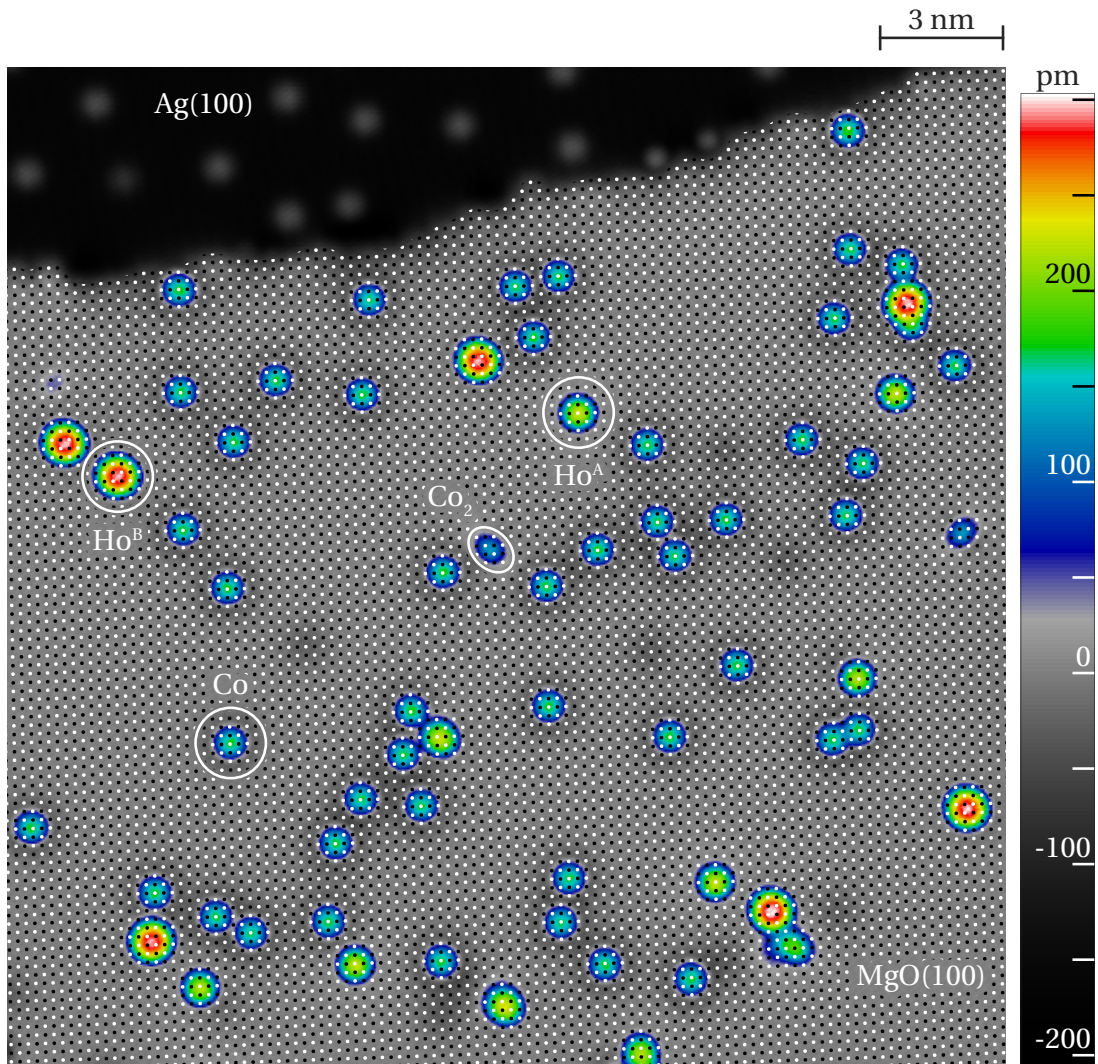
Figure 3.13 – STM image of Co and Ho atoms co-adsorbed on 1 ML MgO. The lattice is inferred from atomically resolved images of the bare MgO surface and the O (white circles) are put into coincidence with Ho^A atoms. Black circles stand for lattice Mg atoms. Note the presence of some defects on the MgO layer that can be ascribed to O point defects. ($T_{dep} \approx 10$ K, $V_t = -20$ mV, $I_t = 20$ pA, $T_{STM} = 5$ K).

and largest (301 ± 2 pm) objects to correspond to Ho^A and Ho^B respectively. The overlaid MgO lattice is extracted from an atomically resolved image of the substrate and one of its O atom brought in coincidence with one Ho^A atoms. One sees that all the Co atoms are adsorbed on top of O, in agreement with reported DFT calculations the literature [48]. For the range of MgO thicknesses between 1 and 3 layers we probed, no dependence of the Co adsorption site on MgO patch thickness was observed. Note the existence of two elongated objects. STS reveals inelastic steps around 8.0 ± 1.2 mV, therefore we identify this object as Co dimers [108]. Thanks to the overlaid MgO lattice, we find that their axis is aligned along the O sublattice and each of

the two constituents of the dimer very close to two neighboring O sites.

Cobalt atoms adsorb exclusively on top of the O atoms of the MgO. They are in addition easily identified with STS as they show inelastic step at 57 meV, see for example Fig. 3.14(b). They are markers of predilection to seek for the O sites of the MgO. Therefore they will be extensively used in the following to determine the adsorption site of other metal species on MgO.

3.5.3 Iron

The Fe/MgO system is of very great importance as for example this is the first system showing long spin-coherence and spin-relaxation times [38,81]. This is the first system where (ESR) with the STM was demonstrated. This powerful technique permits to use the adsorbed Fe atoms as a local magnetometer to probe atomic magnetic fields with the STM. Again, the magnetic particularities of the Fe atoms depend crucially on the crystal field of its adsorption site. This motivated for DFT calculations which have shown that Fe adsorbs on top of oxygen [109, 110]. Here we use Co as marker for the O lattice sites of the MgO and want to determine experimentally the adsorption site of Fe.

Figure 3.14(a) shows a MgO/Ag(100) region with Fe and Co atoms. Both atoms have quite the same apparent height but can easily be distinguished from their spectroscopic features, reported in Fig. 3.14(b). While Co exhibit a spin excitation around 57 meV, Fe atoms are identified by one at 12 meV [48, 109]. The MgO lattice, extracted from an atomically resolved image of the MgO substrate, is superimposed on the STM image with the O lattice site at the positions of the Co protrusions. We determine with experiment that Fe shares the same adsorption site as Co, namely O.

3.5.4 Gold

The adsorption site of Au adatoms on MgO is a subject of longstanding debate in literature. Electron paramagnetic resonance experiment on 20 ML thick MgO showed that Au is likely to adsorb on top of O [91]. Interest for Au atoms comes from the fact that charge transfer from the substrate to the adatom depends on the MgO thickness [97]. Thus this is a system where we can control the charge state of the adsorbate by modifying the substrate. However, on thin MgO layers ranging from 1 to 4 ML, the adsorption site of MgO has been predicted by DFT to be on top of O [90], on a bridge site and also on a Mg site, depending on the MgO thickness [89]. Sterrer *et al.* [97] proposed an experiment to show the adsorption site of Au and concluded that on 3 ML MgO, Au adsorbs equally on O and Mg sites. They also proposed, from another experiment, that on 8 ML MgO it preferentially adsorbs almost uniquely on top of O [97]. For that, they superimposed a grid representing the MgO lattice over their STM images but without any reference to anchor the grid. As a matter of fact, their results are fully compatible with adsorption of Au on top of bridge sites for 3 ML MgO.

Straightforward comparison between the works in references [97, 111, 112] and our work is unlikely, because they only base their MgO thickness calibration on the time of evaporation of magnesium during the CVD growth of the MgO thin films. We would assume that our 1
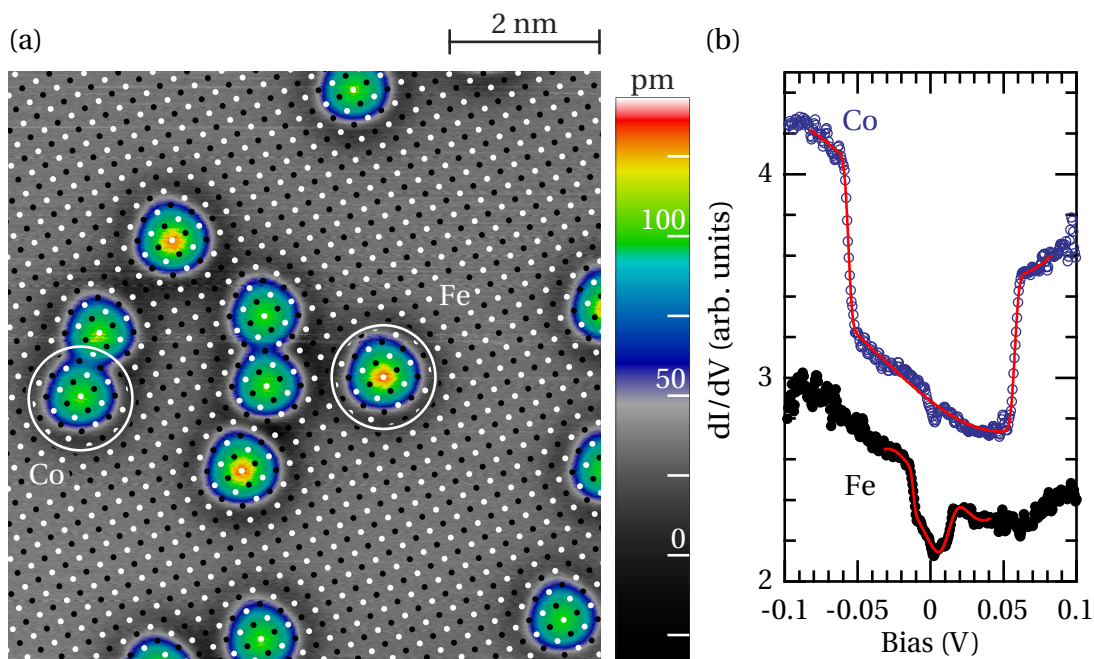
Figure 3.14 – (a) STM image of Fe and Co adatoms co-adsorbed on MgO. The MgO lattice is extracted from an atomically resolved images of the substrate. The O atoms of the lattice (white circles) are superimposed on top of Co atoms. Black circles stand for Mg lattice atoms ($T_{dep} \approx 10$ K, $V_t = -50$ mV, $I_t = 20$ pA, $T_{STM} = 5$ K). (b) Differential conductance spectroscopy (dI/dV) of the Fe and Co adatoms in (a). Spectra of a same atomic species are averaged; they can be used to distinguish between Co and Fe with STM. (Set-point: $V_t = -50$ mV, $I_t = 20$ pA, modulation frequency of 397 Hz with a peak-to-peak amplitude of 2 mV). Adapted with permission from [92].

and 2 ML MgO are representative for what they identify as 3 ML MgO. For that, we look at Fig. 3.15(a) which reports precisely an STM image of Au adsorbed on MgO. Firstly, most of the protrusions are single Au adatoms, but there are still three unidentified objects, marked with a question mark. We superimposed a MgO lattice grid on top of them (not shown here) and determined that all the objects adsorb on the same lattice site. We tried to compare our STM data to what is reported in the literature in order to possibly identify the larger objects. We note that Simic-Milosevic *et al.* [112] observed objects for Au/MgO/Ag(100) samples that were identified as flat lying and upstanding Au_2 dimers. Upstanding dimers are reported to have 20% of increase in apparent height as the monomers, *i.e.,* relation of monomers and upstanding dimer is of 1.2. Unfortunately, with the data of Fig. 3.15, we get a relation of 2.4 for the same quantity, thus not corresponding to Au dimers. One possibility would be a different charge state for the Au adatom. Similarities exist with the system of Au/NaCl, where a negatively charged Au adatom goes hand in hand with the depression rim all around the Au adatom. In their experiment, Steurer *et al.* [84] achieved manipulation of the charge state of the Au adatom and the neutral version of Au has an apparent height much larger than for the Au^-. In addition, the negative version of Au adatom holds a depression rim, while the neutral

one does not. One possibility would be that our unidentified object is a neutral Au adatom. But at the time we cannot prove that, one should be able to convert one species into the other one to show that it is the same object with different charge state. Secondly, the Fig. 3.15(b) presents the histogram for the first nearest neighbor distance, calculated from a bigger image than the Fig. 3.15(a). Overlaid in red is the curve representing the same distribution for a sample whose adatoms would occupy the surface at random. It follows the relation,

$$f_{\mathrm{ran}}(r) = \left(2\pi r \Delta r \frac{N^2}{L^2}\right)\left(1 - \frac{4\pi}{L^2}\right)^N \left(\frac{\pi L^2 + (4-\pi)r^2 - 4rL}{\pi L^2}\right), \tag{3.1}$$

where N, L, Δr stand for the number of atoms in the image, the lateral size of the STM image and the width of the histogram classes [113]. Clearly, the distribution of first neighbor distance for Au do not follow the red curve, indicating that an external interaction drives the system to make Au atoms adsorb with a specific defined distance of 2.3 ± 1.0 nm between them. We assume that Au adatoms experience Coulomb repulsion; this hypothesis is in-line with former experimental observations and theoretical calculations [97, 111, 114] which indicate that Au get charged on thin MgO layers supported by a metal substrate. Thus we propose that we also observe charged Au adatoms in Fig. 3.15(a). This is in line with the measurements for 3 ML MgO reporter by Sterrer *et al.* [97]. Our experiments on 1 and 2 ML MgO compares with their experiments reported for 3 ML MgO.
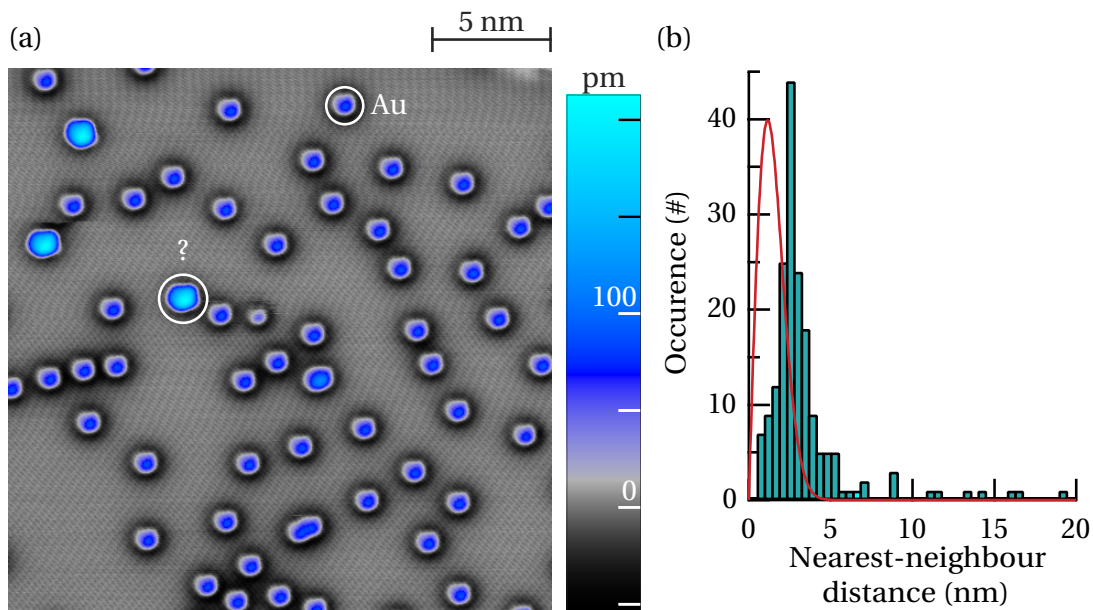
Figure 3.15 – (a) STM image of 0.94% ML of Au adsorbed on MgO. Most of the objects have an apparent height of 86 ± 3 pm, identified as Au monomers. Three objects, with apparent height of 209 ± 2 pm remain unidentified, but share the same adsorption site (not shown) as the Au monomers ($V_{\mathrm{t}} = -100$ mV, $I_{\mathrm{t}} = 20$ pA, $T_{\mathrm{STM}} = 5$ K). (b) Histogram of the distribution of the first nearest neighbor distance calculated for a wider image of the same sample, with superimposed in red the distribution expected for random placement of the adatoms at the surface for the same coverage.

We want now to determine the adsorption site of the Au monomers. For that, we will independently use Co and Ho as marker for the O and bridge lattice positions of the MgO. Figures 3.16 and 3.17 show a MgO region with Au atoms and, respectively, Ho and Co co-evaporated. The very small apparent height of 107 ± 4 pm of Au adatoms permit to recognize them easily. Again, the MgO lattice is inferred from an atomically resolved STM image of the bare MgO surface and one of its O lattice atoms brought in position on top of a Ho[A] atom or Co atom. We observe a predominant adsorption of Au adatoms on bridge sites. This is in line with calculation for Au adatoms adsorbed on MgO thin films grown on Mo(100), where the same adsorption site is predicted [89].

A statistical analysis over 50 Au atoms on 1 ML MgO indicates that they almost exclusively adsorb on bridge sites, with a very small fraction ($8 \pm 4\%$) found on top of Mg (see Fig. 3.16 and 3.17). We cannot for now discriminate between adsorption on a defect or if the Mg is a stable adsorption site for the Au atoms on thin MgO films. Nevertheless, it is interesting to compare this with Fig. 3 of reference [89]. Their DFT calculations of single Au atom adsorption on MgO/Mo(100) predicted, in order of decreasing adsorption energy, an adsorption on top of bridge, Mg and O. Note, however, that for thicknesses of 1 to 5 ML MgO, the difference in energy for the bridge and Mg site is very small, and Mg adsorption site is even the most favorable for 5 ML MgO. More investigations are needed for the Au/MgO/Ag(100) abundances of each adsorption site but our conclusions are fully compatible with the predictions of Honkala *et al.* [89].

The adsorption of Au adatom on 1 and 2 ML MgO/Ag(100) has been investigated with DFT with exactly the same method reported in reference [92]. Table 3.2 shows the results of these calculations. The bridge site is clearly identified to be the most favorable, but for 1 ML MgO, O site is very close in energy. Mg site is by far unfavorable on 1 and 2 ML MgO. On bulk MgO, O is the most favorable adsorption site. STM investigations did not exhibit any Au adatom adsorbing on top of O site. At variance, adsorption of Au on top of a Mg site was observed with STM, see for example Fig. 3.16. All calculations agree that on bulk MgO Au atoms adsorb on top of O and EPR experiment came to the same conclusion [90, 91]. In light of these observations, Au adsorption site must change between thin (1 to 3 ML) and thick (20 ML to bulk) MgO thicknesses. STM is not recommended for investigations on more that an

Site	1 ML MgO/Ag		2 ML MgO/Ag		MgO(100)	
	ΔE	Δq	ΔE	Δq	ΔE	Δq
O	0.04	-0.77	0.18	-0.80	0.00	-0.28
br	0.00	-0.77	0.00	-0.83	0.15	-0.31
Mg	0.19	-0.73	0.18	-0.79	0.35	-0.26

Table 3.2 – DFT binding energy differences ΔE (eV) and charge transfers from the substrate to the adatom Δq (e) for individual Au atoms on O, bridge (br), and Mg sites on 1 and 2 ML thick MgO/Ag(100) and on the (100) surface of bulk MgO. The site with the highest binding energy is taken as reference; positive values signify a decrease in binding energy. The simulated system in globally neutral.

estimated thickness of 3 or 4 ML MgO due to the reduced conductance of the MgO layers. In this case AFM experiments are suggested due to their ability to scan over insulating samples. Experiments that could be conducted to determine the adsorption site of Au adatoms on thick MgO layers could be the following: From a Ca-doped bulk MgO crystal, gentle annealing of the substrate will allow the Ca to segregate to the surface [100, 101] and then provide robust markers for the Mg lattice positions. Subsequent evaporation of Au atoms on the He-liquid cooled sample will provide adsorption of individual adatoms. Then adsorption site of Au adatoms should be determined following the same method used in section 3.3. Atomically

Figure 3.16 – STM image of Au and Ho atoms co-adsorbed on 1 ML MgO. The MgO lattice, extracted from atomically resolved images of the substrate, is overlaid such that the O (white circles) are put into coincidence with Ho^A protrusions. Black circles represent the Mg lattice atoms. We could not identify the objects with an elongated shape. ($T_{dep} \approx 10$ K, $V_t = -100$ mV, $I_t = 20$ pA, $T_{STM} = 5$ K).

resolved AFM images of the substrate could provide the lattice parameter and orientation of the MgO lattice. By overlaying the Mg atoms of the lattice on top of the Ca atoms of the AFM measurement, the adsorption site of Au adatoms can be determined. In the case of difficulties in discriminating the Au adatoms from the Ca protrusions in the AFM contrast, one could check which protrusions could be manipulated or desorbed, as reported for Au on NaCl [84]. Ca species, embedded into the MgO surface, are not expected to be affected by such manipulations.

When Au adsorbs on thin MgO layers, the adatoms get charged negatively [89, 90, 97, 111], see table 3.2. Interestingly, this charge is opposite in sign to the charge that one Co or Ho adatom gets [48, 80]. Therefore, one cannot exclude electrostatic interactions between two adatoms of opposite charge. Visual comparison between figures 3.16, 3.17 and 3.13 reveals that the presence of Au adatoms goes hand with hand with the presence of many more unidentified objects. These objects would correspond to AuHo (Fig. 3.16) or AuCo (Fig. 3.17) heterodimers, adsorbing in a configuration still to resolve. These objects are never identified without the presence of at least two atomic species, therefore they should be a mixture of them. In the STM image of Fig. 3.17 there are some objects identified as AuCo dimers. These are also reported on the Fig. 3.18, where one can only note that these AuCo protrusions are perfectly circular. They adsorb on top of an O site and appear as very round protrusions, thus excluding a planar adsorption geometry for a dimer. Indeed in the case of planar adsorption, the shape would be oblong, see Fig. 3.13 for the case of Co dimers for example. Note that all the protrusions are surrounded by a depression rim, much more pronounced for the Au adatom (negatively charged, apparent depth of -53 ± 5 pm) than for the Co ones (-24 ± 4 pm). The AuCo depression rim depth is of -20 ± 6 pm, very close to the Co one. For the systems we are aware of, the existence of the depression rim around an adatom adsorbed on insulating thin films goes hand in hand with a charge transfer from (to) the adatom to (from) the underlying metal substrate [82–84]. The similarity of the depression rim for Co and AuCo objects would tentatively suggest that Co is in contact with the surface, and Au lies on top of Co. They are readily identified as AuCo upstanding dimers, with the dimer long axis perpendicular to the MgO plane. Note that Simic-Milosevic *et al.* [112] reported on creation and dissociation of a Au upstanding dimers on MgO, therefore this is worth to consider the existence of upstanding metal element dimers on the MgO substrate.

3.5.5 Terbium

Lanthanide elements adsorbed on MgO are promising systems for the study of the magnetism at the atomic level with scanning probes techniques. The Ho/MgO system was shown to have magnetic remanence even at very low magnetic fields [80], and further investigations revealed its exceptional magnetic moment of about 10 Bohr magnetron [37]. Naturally, following steps include the study of other lanthanide elements on MgO. In this line, one additional lanthanide to be investigated is Tb. We investigated the Tb/MgO system with the STM to get

insight in their adsorption configuration while Pietro Gambardella's group, at ETH Zürich, was responsible for the investigation of the same system with x-ray magnetic circular dichroism. The interest is strongly focused on Tb adsorbing on 2 ML and thicker layers of MgO, since in analogy with the Ho/MgO system, interesting magnetic properties are expected to arise on MgO thicknesses of 2 ML and more.

An STM image of 2 ML MgO with 0.9% ML of Tb adatoms is presented in Fig. 3.19. At first sight we recognize the presence of two species of different apparent height. In analogy with the Ho
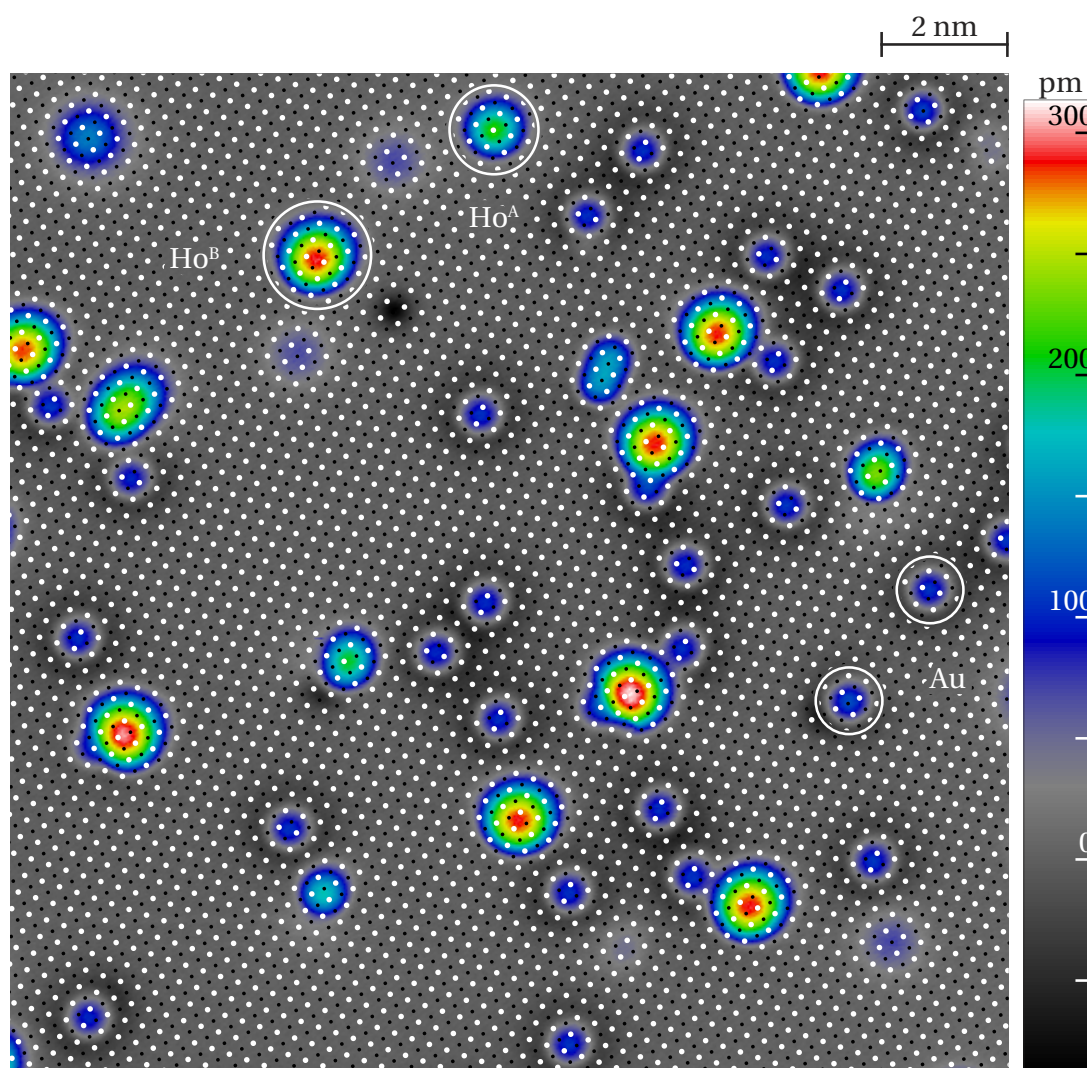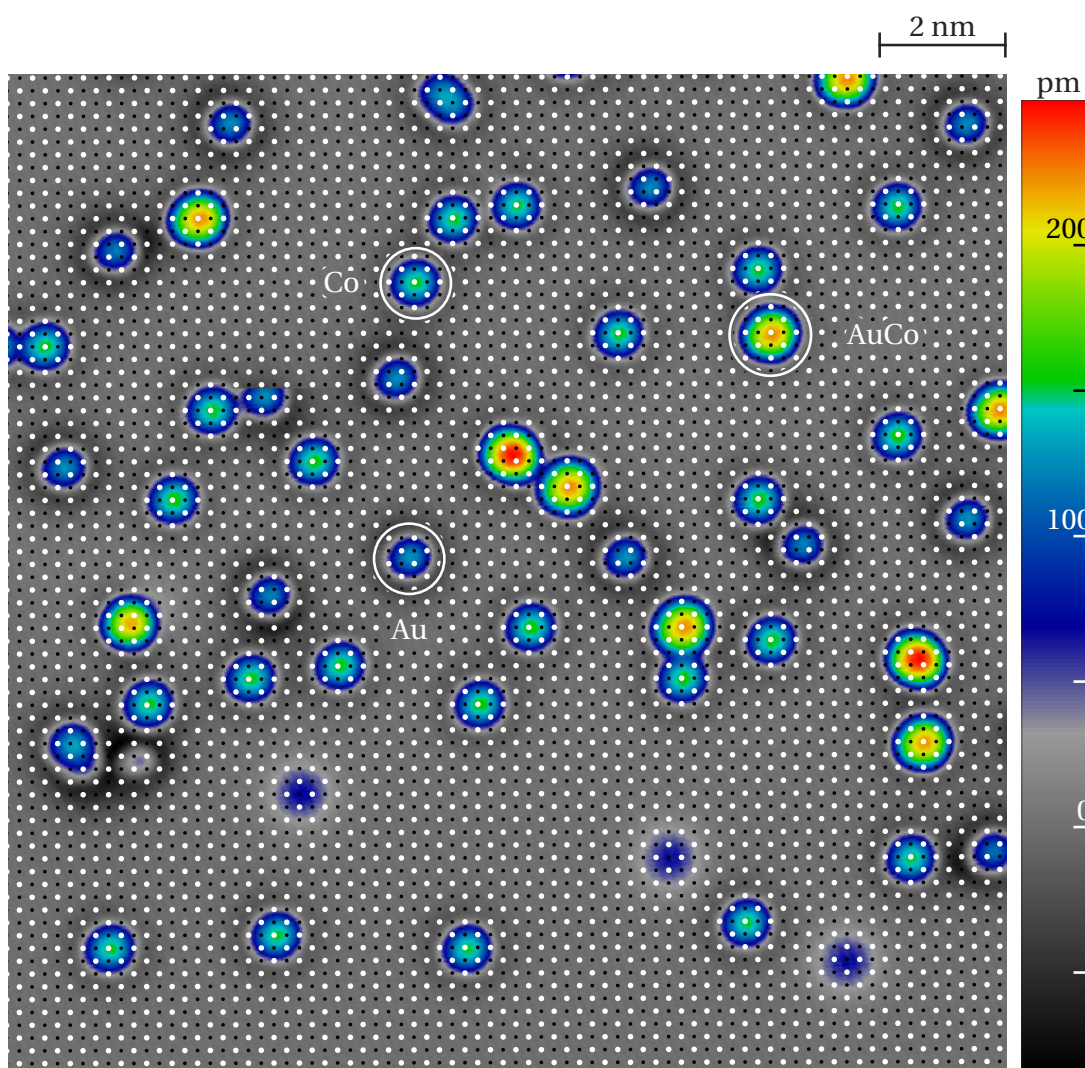

Figure 3.17 – STM image of Au and Co atoms co-adsorbed on MgO. The overlaid MgO lattice is extracted from atomically resolved images of the substrate. White circles, standing for the O atoms of the MgO lattice, are brought on top of Co atoms. Black circles stand for Mg. Note the presence of very small protrusions on the MgO substrate on top of Mg lattice positions, identified as defects. Objects with the biggest apparent height are assumed to be AuCo upstanding dimers, see the main text. ($T_{dep} \approx 10$ K, $V_t = -100$ mV, $I_t = 20$ pA, $T_{STM} = 5$ K).

and Er/MgO systems, we label the one with smaller apparent height (250 ± 6 pm) Tb^A and the larger one (327 ± 4 pm) Tb^B. The overlaid grid is extracted from atomically resolved images of the substrate and then superimposed on the image. It cannot determine the adsorption site of the Tb adatoms, but clearly shows that the newly named Tb^A and Tb^B adatoms do not share the same lattice site. Tb^A species adsorb all on the same site, as they are all imaged on the crossings of the grid, while Tb^B adatoms adsorb on the two equivalent sites halfway between the crossings of the grid. This provides strong evidences for Tb^A and Tb^B adsorbing on O and bridge sites, respectively, but that would be certain only with comparison of Tb species adsorption position relatively to a marker, like Co. This is reported on the Fig. 3.20 which shows co-adsorbed Co and Tb on MgO. Because Co acts as a marker for O lattice positions, Tb^A is known to adsorb on O sites of the MgO while Tb^B adsorbs on bridge sites halfway between two O (Mg) lattice position.

The proportions of Tb^A and Tb^B species on 2 ML MgO is of $82.9^{+1.3}_{-1.4}$%, respectively $17.1^{+1.4}_{-1.3}$%. These are calculated from the objects clearly identified as Tb^A or Tb^B species. From our STM observations, from 2 ML MgO and more, Tb^A species is by far the most abundant. These abundances do not depend drastically on the Tb coverage, nevertheless, at high Tb coverages like the one used in Fig. 3.19, around 4% of the total objects at the surface exhibit an elongated shape, indicating that for high coverage Tb adatoms could perhaps interact between themselves. They do not appear at lower coverages of 0.5% ML, and are quite exclusively found on 2 ML MgO. As we learn from section 3.3 that Ho adatoms have some kind of transient mobility on 2 ML MgO, we assume that it should be the case also for Tb. These elongated objects (labeled Tb2 in Fig. 3.19) are too elongated to assume them to be terbium homodimers. They could perhaps better correspond to adatoms adsorbing very close. Interestingly, Fig. 3.19
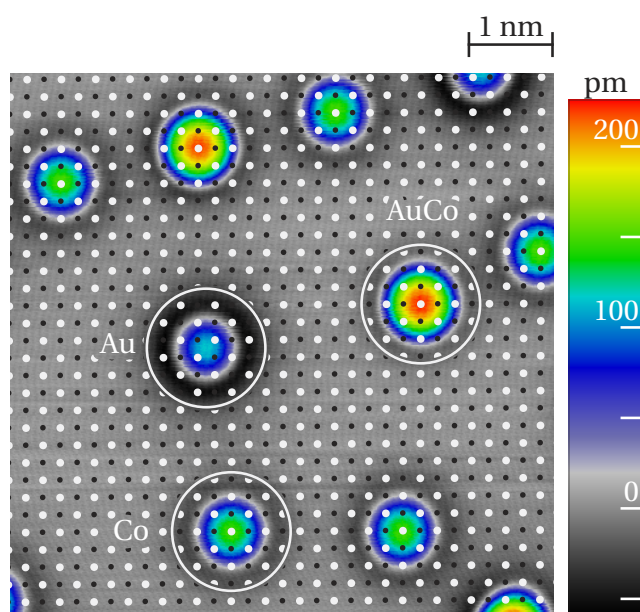
Figure 3.18 – (a) Magnified STM image of a MgO region supporting Au and Co adatoms as more as assumed AuCo heterodimer. The overlaid lattice of black (Mg) and white (O) protrusions represents the MgO atomic lattice. AuCo protrusions are perfectly circular and adsorb on top of an O lattice site. Note the depression rim around each objects, betraying fractional charge on the objects ($T_{dep} \approx 10$ K, $V_t = -100$ mV, $I_t = 20$ pA, $T_{STM} = 5$ K).

shows that there are two kinds of Tb2 objects. The one with higher apparent height seems to be two Tb^A objects adsorbing on nearby O sites. Indeed, apexes of the object are located on two next-nearest neighbor O lattice positions (represented by the crossing of the grid). Dimers with smaller apparent height seem to be composed by two objects adsorbing on two Mg sites separated by two atomic lattices distance. This is strange because no Tb single atom was observed to adsorb on Mg site on 2 ML MgO. Perhaps that by pair they have some interaction
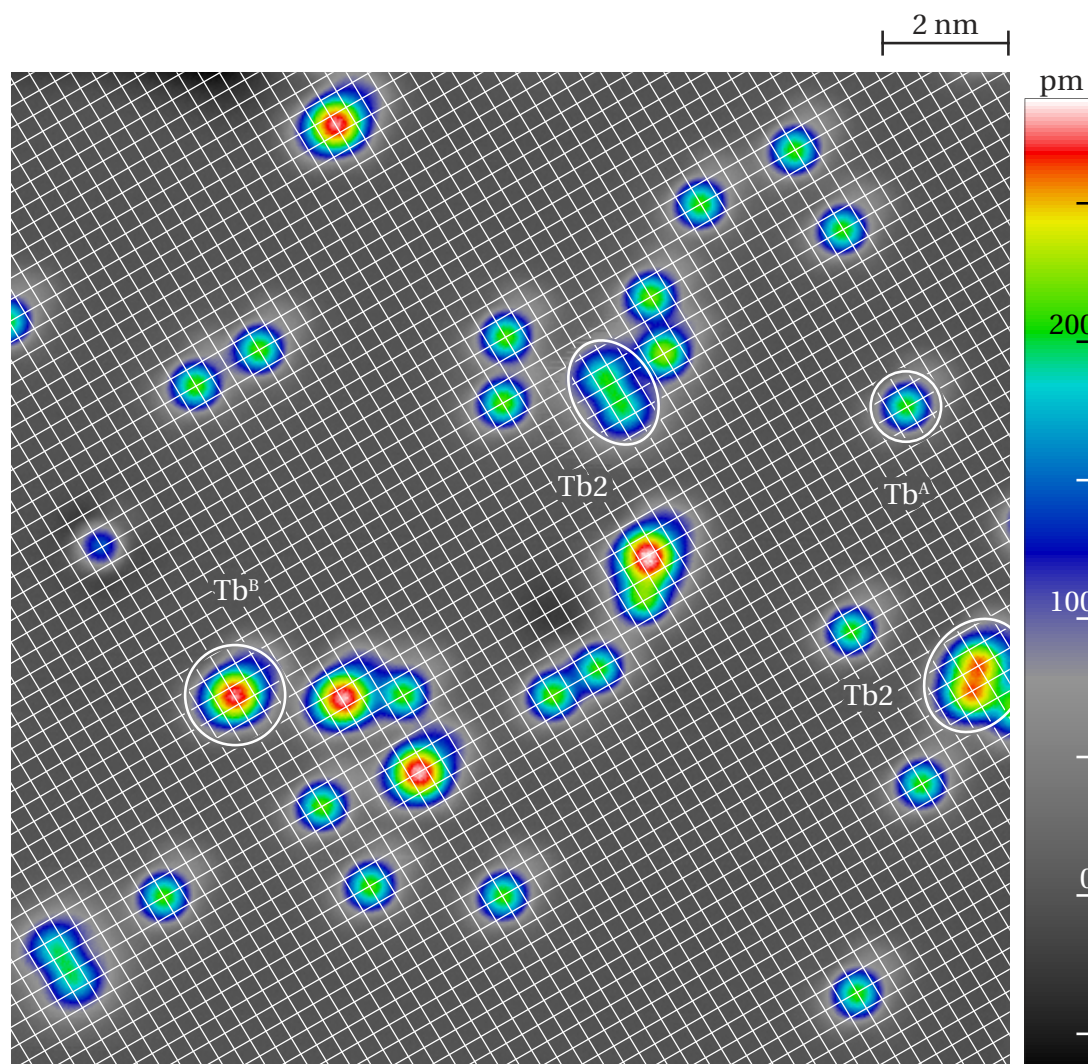
Figure 3.19 – STM image of 0.9% ML Tb adsorbed on 2 ML MgO, exhibiting two major species labelled Tb^A and Tb^B, with similarity to the Ho/MgO case. The grid is extracted from atomically resolved images of the substrate and one of its crossing put into coincidence with one Tb^A adatom. Tb^A and Tb^B do not share the same adsorption site. Elongated objects, labelled Tb2 and aligned along the [100] and [110] directions of the MgO substrate, are assumed to be two Tb adatoms adsorbing very close to each other. ($T_{dep} \approx 10$ K, $V_t = -100$ mV, $I_t = 20$ pA, $T_{STM} = 5$ K).

that stabilizes the adsorption on a Mg site. At this time we cannot understand the origin of this kind of objects. An idea for answering this question would be to try to produce this kind of Tb2 objects. One could try to manipulate one Tb atom and bring it close to another Tb atom and to see they can be created. With delicate manipulations one would affect only the adsorption site on the manipulated object, while the second would not change. If the objects can be created with this method, we could then resolve their adsorption configuration. We also can additionally to try to separate both of the Tb2 objects. If after the manipulation we end with two individual Tb objects, we would have indications that Tb2 objects are two Tb adatoms adsorbing very close. Unfortunately at the first sight we associated the Tb2 objects as defaults, this is later that we got aware of the reality of existence of such objects. Therefore we have not conducted these tests to identify the origin of the Tb2 objects.

Figure 3.20 shows an STM image of Co and Tb atoms co-adsorbed on 1 ML MgO. Co, Tb^A and Tb^B adatoms are easily recognized. Using Co as a marker for O lattice positions, we determind their respective adsorption site, as already reported. In addition to that, we identify a new natural specie which apparently exists on 1 ML MgO, the Tb^C species, adsorbing on top of a
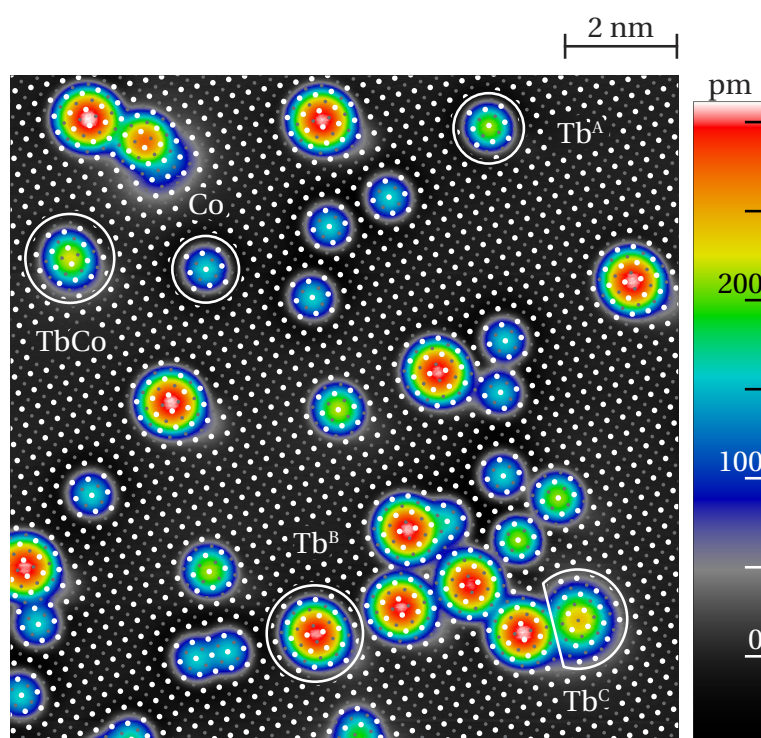
Figure 3.20 – STM image of Co and Tb atoms co-adsorbed on 1 ML MgO. The superimposed MgO lattice was extracted from atomically resolved images. Its O atoms (white circles) are put into coincidence with the Co protrusions. The grey circles stand for the Mg atoms of the lattice. A TbCo heterodimer is identified thanks to its asymmetric shape, with similarity with HoCo dimers [115]. Note the presence of Tb^C species naturally existing for Tb on 1 ML MgO, at variance with Ho and Er. ($T_{dep} \approx 10$ K, $V_t = -100$ mV, $I_t = 20$ pA, $T_{STM} = 5$ K).
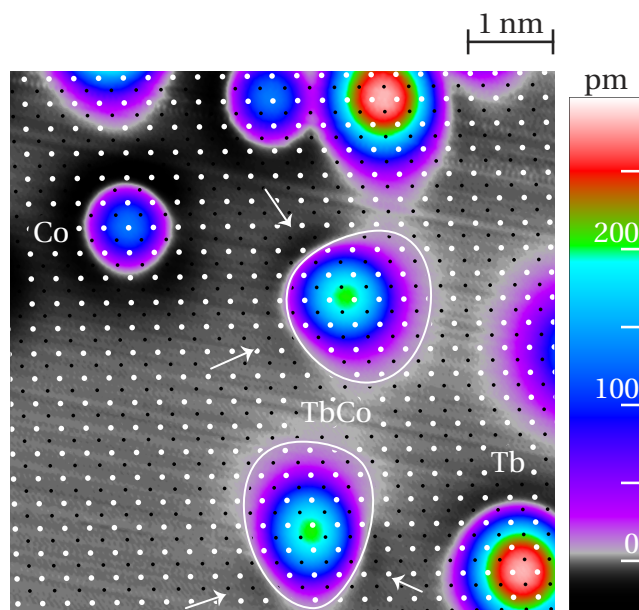
Figure 3.21 – Magnified STM image showing better the asymmetric shape of the TbCo dimers. The overlaid grid of white (O) and black (Mg) circles represents the MgO lattice. Note that TbCo adsorbs on directions joining two nearest neighbor O lattice positions. The overlaid white curves represent the shape of the TbCo dimer. The shape of the top (bottom) dimer is symmetric along the horizontal (vertical) O–O direction. It has a non-diffuse part on the left (bottom) of the top (lower) dimer, and a diffuse tail on the right (top). The arrows indicate the small apparent height depth always found in front of the non-diffuse part of the dimer. The STM image was filtered with a gaussian kernel with 0.016 nm in standard deviation to remove the high frequency speckle pattern existing on the flat regions of the MgO surface ($T_{dep} \approx 10$ K, $V_t = -100$ mV, $I_t = 10$ pA, $T_{STM} = 5$ K).

Mg lattice position. Objects with asymmetric shape are identified as TbCo heterodimers as they do not appear without the presence of Co at the surface. Figure 3.21 shows a zoomed area with two of these TbCo dimers. Clearly the asymmetric shape is recognizable, with a sharp head and a diffuse tail, exhibited with the purple color. Unfortunately the imaging conditions were not the best one could expect from the STM, but still we can observe that these dimers are orientated perpendicularly one to each other, following the symmetry of the substrate. This TbCo dimer shows inelastic conductance steps at 60.5 ± 0.2 meV, very close to the reported value of 57 meV for Co monomers [48]. TbCo dimers are objects whose adsorption geometry can be resolved in the STM images. Firstly, they adsorb along the [100] directions of the lattice, thus they can be found in two orientations corresponding to the two equivalent [100] directions of the MgO substrate. With good imaging conditions one observes the asymmetric shape of the dimer. The right part of the TbCo dimer at middle of the STM image in Fig. 3.21 is more diffuse than the left part. In addition, very faint depression in the left-part side of the dimer are observed, see where the arrows are pointing. This permits to set-up a tentative model for adsorption of the TbCo heterodimer on the MgO:

- Tb and Co adsorb on two neighboring O lattice position, or

- Tb and Co adsorb on an O lattice site and a close neighbor bridge site.

Manipulation of the adsorption site of Tb atoms with the STM tip is also possible. Figures 3.22(a-c) shows the same region with Tb^A adatoms being transformed into Tb^B and transformed back to Tb^A. For that we ramped the bias with the tip over an adatom, keeping the feedback loop active. Bias ramping procedures are shown in panel (d). Negative bias ramping on top of Tb^B does not affect them, as the tip does not experience an abrupt change in its height. On the other hand, the same ramping procedure on top of Tb^A species transforms them into Tb^B ones, see the changes between Fig. 3.22(a) and (b), and the change in tip height on the red-curve in (d). Inverting the ramping bias to positive one shows that Tb^B adatoms can be transformed into Tb^A, as the changes between Fig. 3.22(b) and (c) show. More interesting is the positive/negative ramping procedure on the two other objets. The first one is a Tb^C adatom, while the second one remains unidentified. The negative bias ramp on top of the unidentified object changed it appearance, but one cannot certify if the adsorption site really changed due to the non-symmetric shape of the object. Clearer observation comes out from the Tb^C species. On Fig. 3.22(a), the Tb^C adatom appears unstable, and with an apparent height intermediate between Tb^A and Tb^B. After the negative ramping procedure, its apparent height lowered, as it appears even smaller than Tb^A species, see Fig. 3.22(b). This change is evinced by the change in tip height over this adatom, see the blue curve in (d). Nevertheless, this object did not change its location on the surface, it is adsorbed exactly at the same site, only its appearance changed. Further bias ramping with positive voltage did not affect it. This is interpreted as a sign of hydrogen contamination [104], as the rare-earth elements are highly reactive and hydrogen molecules are always present in a STM chamber even with a cryogenic pumping. The Tb^C adatom of Fig. 3.22 might be hydrogenated. After the first bias ramp, we removed the hydrogen from the adatom, without changing its adsorption site. The resulting object has an apparent height smaller than Tb^A, which is in better agreement when comparing the apparent height of Ho adatoms on MgO: Ho^C is the smallest one, as Tb^C is after hydrogen cleaning.

Observation of STM images of Tb adsorbed on 1 ML MgO gives rise to some difficulties for the identification of objects. Indeed, close inspection of a total of 2600 Tb objects adsorbed on 1 ML MgO showed that one has to distinguish at least six different type of objects. We suspect that Tb is easily hydrogenated on 1 ML MgO [104], where the hydrogen is thought to reside longer time at the surface due to the increased interaction with the metal substrate. Therefore, if each of the three Tb^A, Tb^B and Tb^C species can get hydrogenated, 6 different species can be potentially found. This was effectively the case and made impossible to have a statistics of abundance for each species on 1 ML MgO. The main reason was because one could not label the different objects of STM images from their apparent height. We have seen in Fig. 3.22 that the hydrogenated version of the Tb^C species has an apparent height close to the Tb^B one. There is no reason that the Tb^A and Tb^B species do not get hydrogenated. Therefore we have
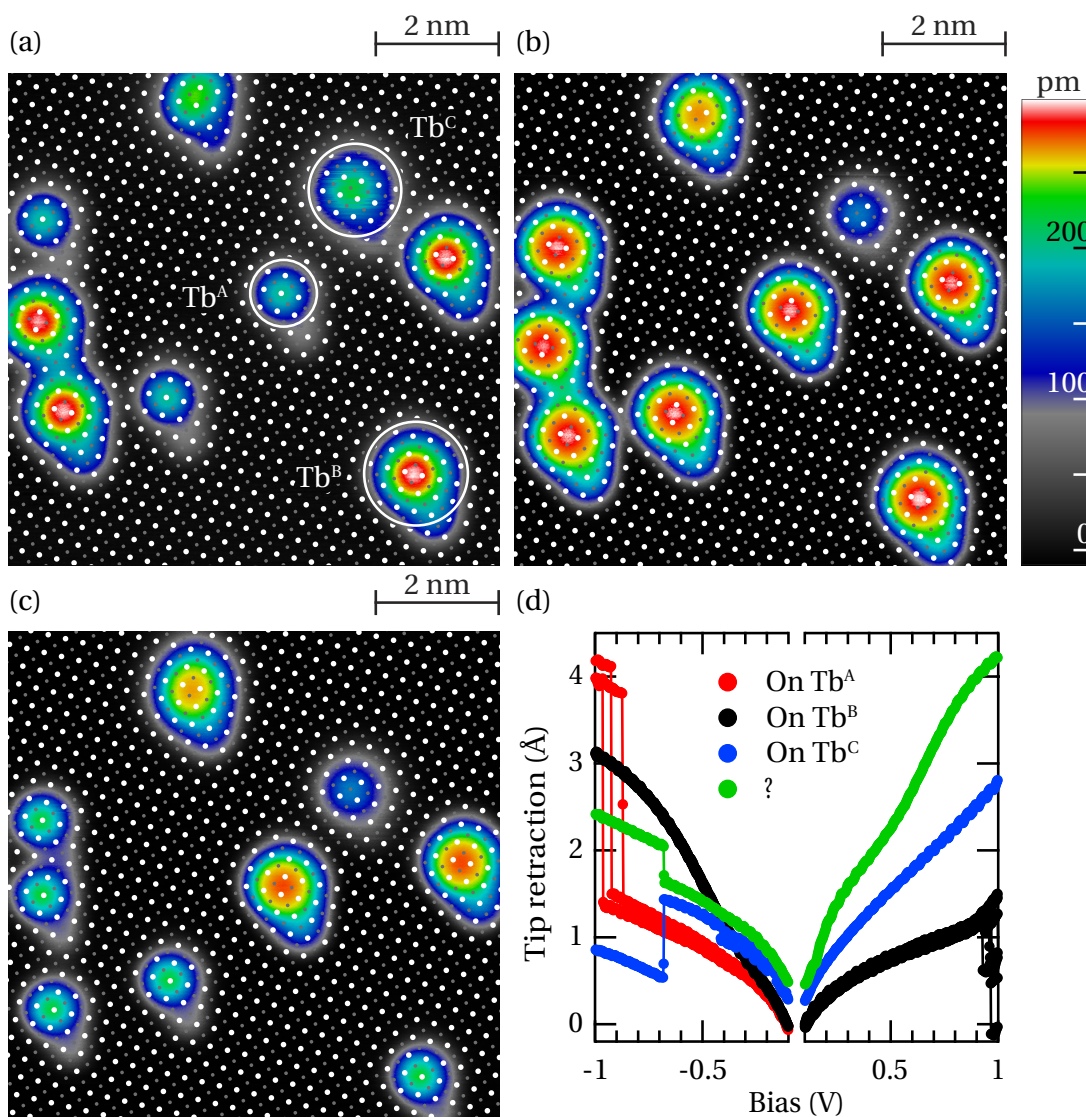
Figure 3.22 – (a-c) Series of images demonstrating the manipulation of Tb species on 1 ML MgO. The MgO lattice, whose white (black) circles stand for O (Mg), is extracted from atomically resolved images of the MgO substrate. The STM image (a) holds Tb^A, Tb^B and Tb^C species, as well as an unidentified object. Negative voltage ramp, shown in (d), on top of Tb^A transforms them into Tb^B. Positive bias ramping (d) on top of Tb^B atoms of (b) transform them back into Tb^A (c). (d) Graph of the positive and negative ramping procedure, performed once for each atoms. Spontaneous change in tip height position evince a modification of the adsorption site of the manipulated adatom. Curves are slightly offset for clarity. Note that between (a) and (b), the Tb^C species adsorbing on top of a Mg lattice position changed in apparent height without changing its location on the substrate. This is understood as the removal of an hydrogen atom, which are known to be the major contaminant in high-vacuum and low-temperature installations. (a-b: $V_t = -100$ mV, $I_t = 20$ pA; c: $V_t = 100$ mV, $I_t = 20$ pA; $T_{STM} = 5$ K).

no clue of what their apparent height could be. At some point one could not differentiate between hydrogenated species and pristine ones and therefore one would count falsely the different objects. Nevertheless, abundance statistics of the Tb species on 1 ML MgO would be possible exploiting these two remarks. First, as green and blue curves of Fig. 3.22(d) teach, the bias of about 0.68 V required to remove the hydrogen from the Tb^C species is lower than the minimal bias of 0.87 V required to transform the Tb^A species. This suggest that imaging with the STM an entire region with a bias of 0.7 V would remove the hydrogen from the adsorbed Tb species without transforming them. This allow a much better counting and labeling of the different Tb species to produce a correct statistics of the abundance of the Tb species on 1 ML MgO. This method has the advantage that scanning over larges areas like 50×50 nm^2 would provide more atomic species on one unique image and then give rise to a more correct statistics. Indeed, on smaller images, the operator always tends to choose regions of interest where there are enough objects and therefore this is already a bias to the statistics. The second conceivable method, which allows in practice only STM image up to 30×30 nm^2, is to consider to put a MgO lattice grid on every STM images where object identification is desired. This allows very clear identification of the different atomic species, even in case of hydrogenated ones, but requires much more time in practice, as the STM image has to be stabilized to reduce the piezo creep and, afterwards, the identification of the objects with an overlaid MgO lattice (or grid) requires much more time than simply visual identification. During the measurement phase of the Tb/MgO system, we were not aware of all these issues. This is why we do not report any abundances for Tb species on 1 ML MgO.

3.5.6 Dysprosium

The last element whose adsorption site was investigated is Dy. Figure 3.23(a-b) shows a 1 ML and 2 ML MgO region, respectively, with adsorbed Dy adatoms. We observe the presence of two atomic species, and we labelled Dy^A and Dy^B the ones with smaller (191 ± 4 pm), respectively larger (275 ± 2 pm), apparent height. The overlaid grid is extracted from atomically resolved images of the MgO substrate and is put into coincidence with the Dy^A species. We observe that all the Dy^A species share the same lattice site, while Dy^B ones adsorb on other site. Determination of the adsorption site of the Dy species is achieved by co-evaporating Dy and Co on the same substrate, as Co acts as a marker for O lattice positions. Figure 3.24 shows a 2 ML MgO region with co-evaporated Co and Dy. The overlaid MgO lattice is extracted from atomically resolved images of the MgO substrate. By aligning the O atoms of the MgO lattice on top of the Co adatoms, one observes that Dy^A adsorbs on top of O while the Dy^B species adsorb on a bridge site.
The abundances of each Dy species are MgO layer-thickness dependent. These are reported on the Tab. 3.3. We observe that on 1 ML MgO the Dy^B species is by far the most abundant, while on 2 ML MgO, Dy^A is the most represented.

When Co and Dy are both present on the MgO surface, sometimes elongated objects are present, as evidenced in Fig. 3.24. They adsorb following the (100) direction of the substrate

and have the same asymetric shape than the TbCo dimers (Fig. 3.21), with a more diffuse end on the larger side of the object. This shape is consistent with the ones found for TbCo, or HoCo. We therefore identify this object as a DyCo heterodimer.

As the studied lanthanide elements on MgO do all follow the same trend, we would expect the possibility to manipulate the Dy species on MgO, and also to create a Dy^C species, potentially adsorbing on top of a Mg lattice site. Figure 3.25 shows a series of manipulations of the adsorption site of the Dy adatoms. Interestingly, the transformation procedures are a little bit different than expected when comparing to the Ho/MgO case. Panel (a) shows a region with 1 and 2 ML MgO patches and a lattice of white (O) and black (Mg) circle representing the MgO substrate. An O atom of the lattice is brought into coincidence of a Dy^A adatom (on 1 ML MgO). All the other Dy^A species fall on O lattice site too, while all Dy^B ones adsorb on a bridge site. One observes that on 2 ML MgO, the Dy^A species also adsorb on top of O, while the MgO lattice was not offset for the additional layer. This is understood as a topologically flat MgO surface as already reported in Fig. 3.3. Nevertheless, even if the substrate is topologically flat locally, the Dy abundances follow what is reported on Tab. 3.3, *i.e.*, we find almost exclusively Dy^A species on the 2 ML patch.

We will describe the transformations procedures on 1 ML MgO and then on 2 ML MgO. Table 3.4 summarizes the experiment of transformations of Dy adatoms, while Fig. 3.25(h) summarize the average bias needed to provoke a change of adsorption site of the Dy adatoms.
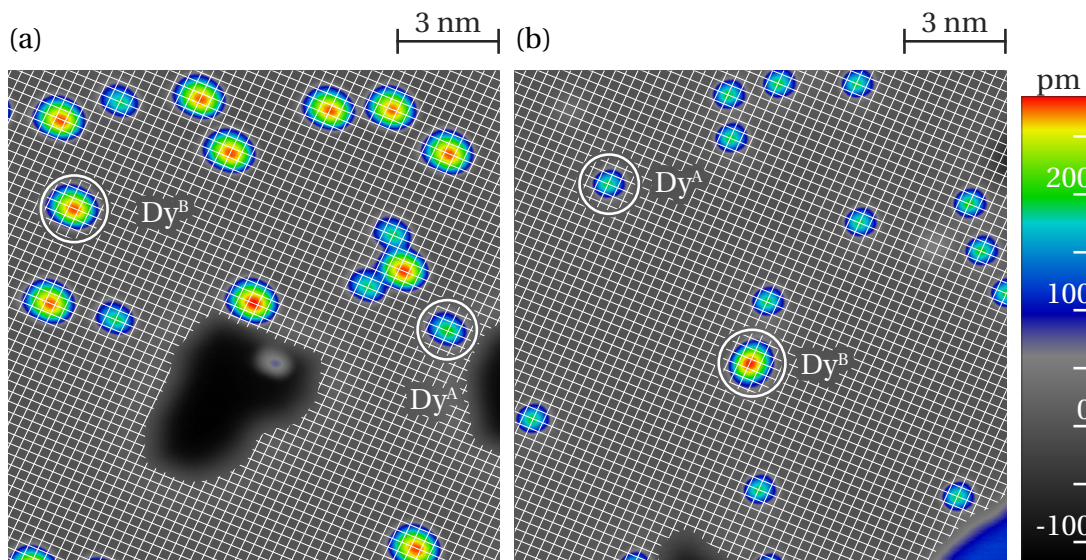
Figure 3.23 – STM images of Dy adsorbed on (a) one and (b) two ML MgO. Two species, Dy^A and Dy^B are distinguished and labelled according to their increasing apparent height, with similarity to the Ho, Er and Tb. The overlaid grid is extracted from atomically resolved images of the substrate and is tentatively put into correspondence with the Dy^A species. (a-b: $T_{dep} \approx 10$ K, $V_t = -100$ mV, $I_t = 20$ pA, $T_{STM} = 5$ K).

	1 ML MgO		2 ML MgO	
	Abundance (%)	Number of atoms	Abundance (%)	Number of atoms
Dy^A	$21.2^{+4.3}_{-3.9}$	21	$74.7^{+4.4}_{-4.7}$	68
Dy^B	$78.8^{+3.9}_{-4.3}$	78	$25.3^{+4.7}_{-4.4}$	23

Table 3.3 – Number of Dy^A and Dy^B atoms counted on 1 and 2 ML MgO over many STM images and the correspondent abundances.
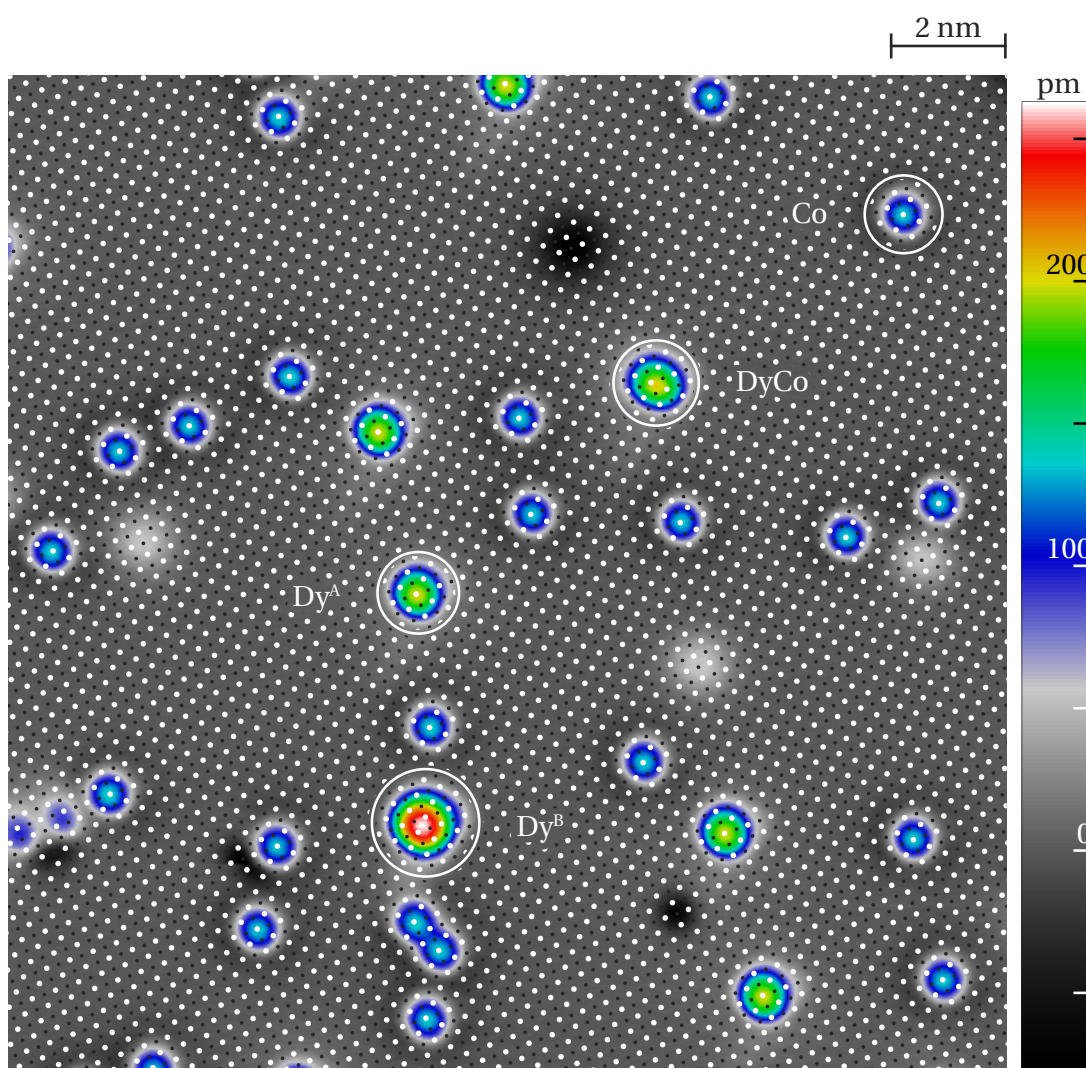
Figure 3.24 – STM image of co-deposited Dy and Co on MgO. The MgO lattice is extracted from atomic resolved images of the substrate. The O (white circles) atoms of the lattice are brought into coincidence of Co adatoms. The black circles stand for Mg. An elongated object is identified as DyCo heterodimer. ($T_{dep} \approx 10$ K, $V_t = -100$ mV, $I_t = 20$ pA, $T_{STM} = 5$ K).

Manipulation of Dy adsorption sites on 1 ML MgO

The 1 ML region of Fig. 3.25(a) supports Dy^A and Dy^B adatoms. A positive voltage ramp, see Tab. 3.4 on top of some Dy^A species permits to transform them into Dy^B. The bias at which the transformation occurs is of about 0.6 V and the transformation produces effectively a Dy^B as it is adsorbed on a bridge site, compare to the overlaid MgO lattice on Fig. 3.25(b), and its appearance is similar to the others unchanged Dy^B species. Interestingly, negative bias ramping on top of Dy^A species of Fig. 3.25(b) also permit to transform them into Dy^B ones, see panel (c). Therefore, we conclude that positive and negative bias ramping allows for Dy^A to Dy^B transformation on 1 ML MgO. Between panel (c) and (e), positive bias up to 1 V were ramped on top of Dy^B species. They did not change in appearance, but sometimes moved to another bridge site. To achieve the STM image in panel (f), a negative bias up to -1.3 V was ramped on top of some Dy^B adatoms. The new and expected Dy^C species, adsorbing on top of a Mg site, is created. This species is also formed after a positive voltage ramp [+1.5 V on Fig. 3.25(f)]. We conclude that on 1 ML MgO, the Dy species transformation is possible only in one way: From Dy^A, we can create Dy^B species with both bias polarity and again with both polarity but higher voltages, create the Dy^C species. This procedure is summarized in Fig. 3.25(h). Reverse transformations were never observed, not even after manipulations.

Manipulation of Dy adsorption sites on 2 ML MgO

The 2 ML regions of Fig. 3.25(a) hold initially only Dy^A species. The first positive bias ramp had no effect on the Dy^A species. Indeed, the Dy^A adatoms did not change in appearance and they adsorb also on the same place in panel (b) than in (a). But, application of a negative bias ramp between (b) and (c) permits to transform the Dy^A species on 2 ML into Dy^B ones. The voltage at which the transformation occurs is around -0.5 V. In panel (c), all the atomic species on 2 ML MgO were transformed into Dy^B. Interestingly, positive bias ramp on Dy^B species transform them into Dy^A ones, as the changes between panel (c) and (d) shows. This transformation occurs at bias around 0.5 V. Therefore by controlling the bias sign, we can transform forth and back the Dy^A and Dy^B species on 2 ML MgO. The next question is whether Dy^C species could also be produced on 2 ML MgO. From Fig. 3.25(e), we apply a negative voltage ramp up to -1.3 V on some Dy^A species. Because we reached higher bias than the 0.5 V required, the Dy^A species were transformed into Dy^B ones, but two over the three probed atoms went transformed back into Dy^A with a change of adsorption location. Indeed, comparison between panel (e) and (f) shows a displacement of the Dy species on 2 ML MgO. Between panel (f) and (g), the same procedure was done with a positive bias on all the Dy species on 2 ML MgO and again, Dy^B species were transformed into Dy^A ones, and the others Dy^A adatoms moved on the surface. We conclude that on 2 ML MgO, creation of the Dy^C adatom is not possible.

Images	Bias ramp (V)	Effect	
		1 ML MgO	2 ML MgO
(a) → (b)	0.1 → 0.8	$Dy^A → Dy^B$	No effect on the Dy^A
(b) → (c)	-0.1 → -1.0	$Dy^A → Dy^B$	$Dy^A → Dy^B$
	-0.1 → -0.6		
(c) → (d)	0.1 → 0.8	No effect on the Dy^B	$Dy^B → Dy^A$
(d) → (e)	0.1 → 1.0	Displacement of Dy^B	$Dy^B → Dy^A$
(e) → (f)	-0.1 → -1.3	$Dy^B → Dy^C$	$Dy^A → Dy^B$
			Displacement of Dy^A
(f) → (g)	0.1 → 1.5	$Dy^A → Dy^C$	$Dy^B → Dy^B$
		$Dy^B → Dy^C$	Displacement of Dy^A

Table 3.4 – Summary of the bias ramp used to transform the various Dy adatoms in Fig. 3.25. Adatoms transformation can occur before reaching the end of the bias ramp. Approximated bias for these transformations and summary of the possible transformations are reported in Fig. 3.25(h).

The summary of the possible transformations between Dy species on 1 and 2 ML MgO is reported in Fig. 3.25(h). We observe that Dy behaves differently from Ho concerning the viability of the different species on 1 and 2 ML MgO. The fact that on 1 ML MgO one cannot recover the Dy^A species from a Dy^B reveals all the complexity of the system.
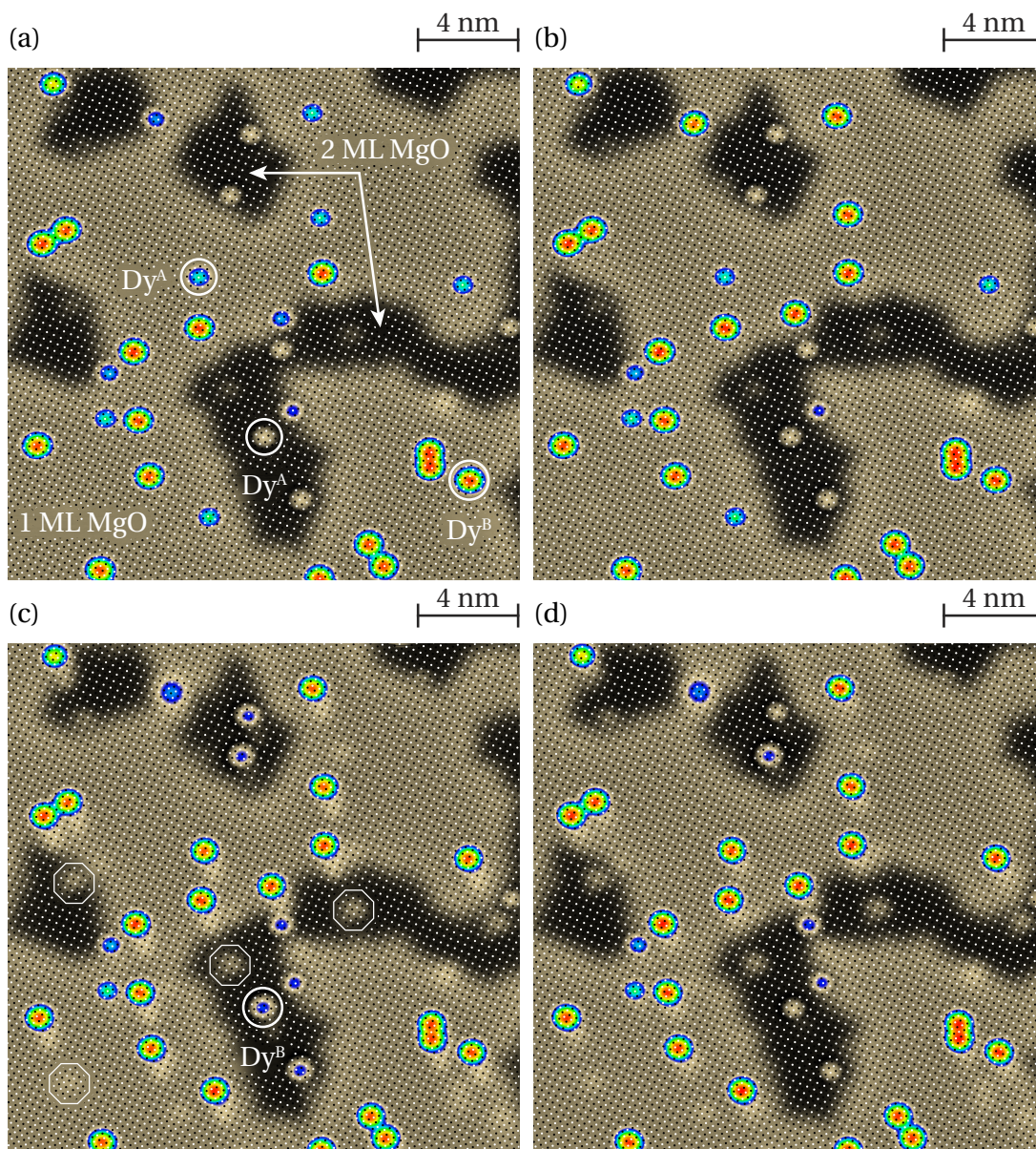
Figure 3.25 – Double page figure — Series of STM images demonstrating the change of Dy adsorption site with STM manipulations. We refer the reader to the Tab. 3.4 for the different bias ramp used for the transformations. Positive voltage ramp on Dy^A species in (a) switches them to Dy^B only on 1 ML MgO. Negative voltage ramp on Dy^A species (both MgO layers) in (b) switches them to Dy^B ones, see the objects which were transformed in (c). From (c) to (d), and (d) to (e): Positive bias ramp, transforming Dy^B to Dy^A only on 2 ML MgO. From (e) to (f): Further negative voltage ramp on top of 1 ML MgO Dy^B switches them to Dy^C. From (f) to (g): Positive voltage ramp on top of 1 ML MgO Dy^B objects switches them into Dy^C. For all images, the MgO lattice of white (O) and black (Mg) circles is extracted from atomically resolved images of the substrate. The colorbar stands for images (a-g). The summary of the possible transformations, on 1 and 2 ML MgO, and the required voltage ramp are reported in (h). The objects inside the octagons in (c), and appearing until image (g), are the shadow of existing objects due to the double tip. (a-g: $T_{dep} \sim 10$ K, $V_t = -100$ mV, $I_t = 20$ pA, $T_{STM} = 5$ K). 78

(e)

4 nm

(f)

4 nm

Dy^C

(g)

4 nm

(h)

pm

200

100

0

-100

1 ML MgO

$$Dy^A \underset{-0.6\,V}{\overset{0.6\,V}{\rightleftharpoons}} Dy^B \underset{-1.3\,V}{\overset{0.9\,V}{\rightleftharpoons}} Dy^C$$

2 ML MgO

$$Dy^A \underset{-0.5\,V}{\overset{0.5\,V}{\rightleftharpoons}} Dy^B \qquad Dy^C$$
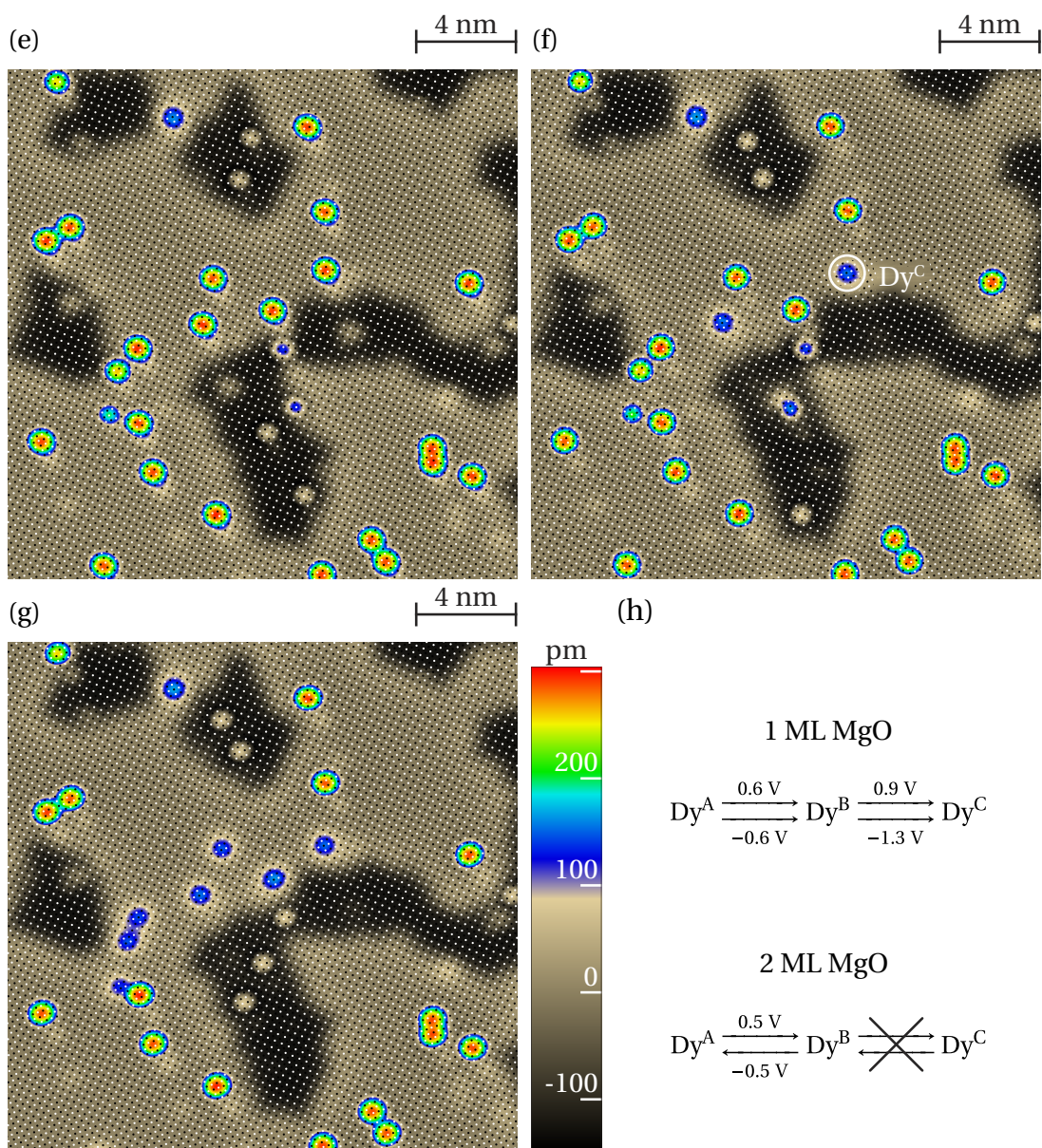
3.6 Conclusion

This chapter shows how we can experimentally determine the adsorption site of various adatoms on MgO thin films. Once the adsorption site of a given element is known surely, one can simply compare the adsorption site of additional elements to the first one. Here we used Ca atoms embedded into the MgO layer as marker for the Mg atom lattice positions. Ca has been shown to segregate toward the surface during the thin film preparation. The adsorption site of Ho, Tb, Er, Co, Fe and Au was determined. Multiple adsorption sites were observed for all the elements except Fe and Co. In the case of Au/MgO, we have shown that previously published data are in line with our experiment and that former investigations misinterpreted the adsorption site of Au, due to the lack of a reference for the Mg or O sites at the surface. Table 3.5 summarize the results on this chapter concerning the adsorption site of the adatoms. We showed that with STM tip manipulations, one could create a variety of objects that do not natively exist upon adsorption, as for example, make Ho to adsorb on top of Mg sites. These manipulations can also be used to control the adsorption site of an adsorbate. The possible transformations are dependent on the adsorbate. For example, Dy adsorbed on 1 ML MgO only allows a one-way transformation process. Nevertheless, in the frame of the possible adsorption site manipulations, one could generate the object of interest to study it. Taking the Ho as example, one only has to transform Ho^A to Ho^B on 2 ML MgO regions if, for some reason, one wants to investigate the properties of Ho^B on this specific MgO thickness.

Species		Site	MgO surface thickness	
			1 ML MgO	2 ML MgO
Ho	Ho^A	O	$35.8^{+1.6}_{-1.5}\%$	$91.5^{+1.6}_{-1.8}\%$
	Ho^B	bridge	$64.2^{+1.5}_{-1.6}\%$	$8.5^{+1.8}_{-1.6}\%$
	Ho^C	Mg	✓$^{(*)}$	✓$^{(*)}$
Er	Er^A	O	$40.9^{+4.4}_{-4.3}\%$	✓
	Er^B	bridge	$59.1^{+4.3}_{-4.4}\%$	✓
	Er^C	Mg	✓$^{(*)}$	✓$^{(*)}$
Tb	Tb^A	O	✓	$82.9^{+1.3}_{-1.4}\%$
	Tb^B	bridge	✓	$17.1^{+1.4}_{-1.3}\%$
	Tb^C	Mg	✓	?
Dy	Dy^A	O	$21.2^{+4.3}_{-3.9}\%$	$74.7^{+4.4}_{-4.7}\%$
	Dy^B	bridge	$78.8^{+3.9}_{-4.3}\%$	$25.3^{+4.7}_{-4.4}\%$
	Dy^C	Mg	✓$^{(*)}$	✗
Au	Au^A	O	✗	
	Au^B	bridge	$92.0^{+3.3}_{-4.4}\%$	
	Au^C	Mg	$8.0^{+4.4}_{-3.3}\%$	
Co		O	100 %	
Fe		O	100 %	

Table 3.5 – Summary of the possible adsorption sites and associated abundances for the measured metal adatoms adsorbed on the MgO thin layers. Cell with the abundances stand for a measured value. Cell with "✓" signify that this species is stable on the MgO surface at 5 K, but that abundances were not measured; additional $^{(*)}$ marker indicates that this species is only found after STM manipulations. Question mark specify that we have no information on the species, as it might be produced by STM manipulation but it was not tried. The symbol "✗" indicates, for Au, that the species was never found in the measurements and, for Dy, that creation with atomic manipulations was not possible, for the probed MgO thicknesses. We recall that the uncertainties are calculated according to the constraint that Ho atoms should be shared between Ho^A and Ho^B species following a binomial distribution.

4 Temperature dependence of Ho species abundance

In this chapter, we will first focus on the temperature dependence of the abundance of the different Ho species, principally on 1 and 2 ML MgO. The thermal stability of the Ho species will also be investigated.

Crucial information presented in chapter 3, prerequisites to the current chapter, is the following. Adsorption of Ho adatoms on 1 and 2 ML MgO is possible on two different adsorption sites of the substrate, *i.e.*, on top of the O, and on the bridge site, halfway between two neighboring O (or Mg) lattice positions. In order to have a direct identification of which species we are concerned with, we rename the Ho species according to their site of adsorption. The former is labelled Ho^O while the second is referred as Ho^{br}. On 1 ML MgO, when the Ho atoms are evaporated onto the sample held at $T_{dep} = 10$ K, the Ho^{br} species is the major population with an abundance of $64.2 \pm 1.6\%$. On the 2 ML regions, almost only Ho^O species are observed, when evaporated in the same conditions. In the following, we will observe how these evolve with the sample temperature during the adatoms deposition.

4.1 Introduction

The laws of thermodynamics tell that a system will, given the possibility, reach the thermal equilibrium which is characterized by a specific value of the energy of the system while at the same time its entropy is maximized [61], *i.e.*, by minimizing its free energy F. When one evaporates the lanthanide (hereafter abbreviated with "Ln") metal atoms (Ho, Dy, Tb, Er) on the MgO/Ag(100) sample, the latter is held at the temperature T_{dep} which value was about 10 K for all the experiments presented in chapter 3. We recall that table 3.5 presents the abundances found for each species on the MgO surface and the main observations are the following:

- The abundances of the species of a lanthanide element greatly vary between MgO thicknesses of 1 and 2 ML.

- The abundances on a specific thickness of the MgO layer also vary a lot depending on the adsorbed lanthanide element.

As we learned in chapter 3, each studied lanthanide is found on two adsorption sites on the MgO surface, on the O and the bridge lattice sites. Adsorption on top of Mg is possible, but it is not populated just after the Ln material evaporation. Only Tb adsorbing on 1 ML MgO is an exception to this rule, and thus is excluded from the following discussion. We will consider that adsorption of Ln adatoms take place only on O and bridge sites for sake of simplicity.

We can easily assume that the evaporated adatoms hit the surface in a random way. If the two adsorption sites the incoming adatoms can relax on are O and bridge, with the bridge one twice as abundant than the O one, sticking of the evaporated atoms at the surface in a random way should exhibit abundances of $1/3$ and $2/3$ for the Ln^O and Ln^{br} species, respectively. In most of the cases, this is not observed. This indicates that the lanthanide adatoms can explore the surface before they relax in their final adsorption site, as suggested by the work of Gao *et al.* [105], who calculated the adsorption mechanism of Pd adatoms on a MgO(100) surface. Our experiments cannot conclude on the adsorption mechanism that an atom undergoes from the gas phase until it get adsorbed. We can nevertheless, and with light of the work of Gao *et al.* [105], propose a model for that. The adsorption mechanism of the Ln adatoms on the MgO thin films is thought to follow roughly the following steps. The Ln atoms are thermally evaporated from a hot rod of the material (temperature $T_{rod} \approx 1700$ K). The energy of these atoms is of the order of $k_B T_{rod}$, in the range of 150 meV in our experiments. When these atoms approach the surface, they are first attracted and gain kinetic energy of the order of the adsorption energy, thus in the electron-Volt magnitude. At some point, incoming adatoms hit the surface and get trapped, but they can travel on the surface until they loose their kinetic energy and relax on one of the possible adsorption sites, O or bridge sites. The fact that the adatoms can explore the substrate before being finally adsorbed is reported as the *transient mobility* [105].

In this picture, and also because we observe two Ln species at the MgO surface, the adatoms should have sufficient energy to overcome the diffusion barrier for each adsorption site just before the relaxation. Following this idea, during the moment that the adatoms exhibit transient mobility, they can test all the possible adsorption sites. In a first approach, we would consider that occupation of the multiple adsorption sites, following a Maxwell-Boltzmann distribution, is possible, provided that the two adsorption sites are close in energy.

In the following the considered lanthanide element will be holmium. We first present data on the abundance of the Ho species as a function of the sample annealing temperature T_{ann}, ranging 4.7 K to 76 K. With that we will be able to estimate the barriers for diffusion of the Ho species. From them we will show that our system of Ho adatoms on MgO should be described in terms of free energy, thus taking into account an entropic term. Trial to explain the abundance of the Ho species as a function of the deposition temperature T_{dep} will help in partially validating the new approach. We finish this chapter in giving some propositions were the description could be improved, despite of the fact that we are unable to provide more experimental data attesting our hypothesis.
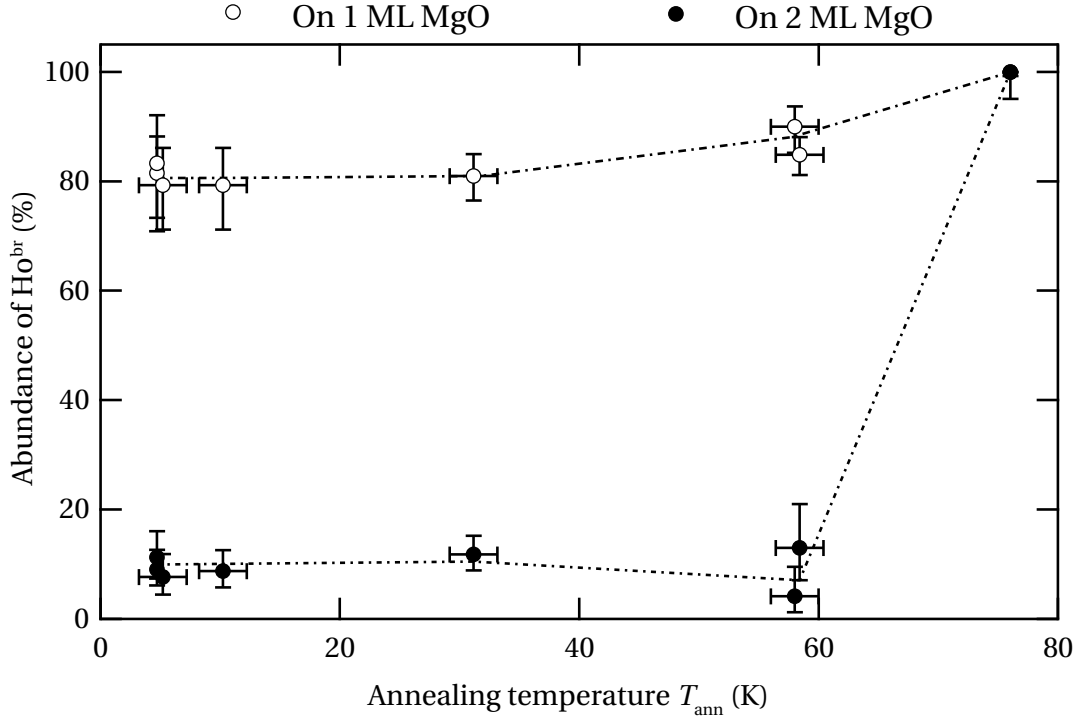
Figure 4.1 – Abundance of the Ho^{br} species as a function of the annealing temperature, adsorbed on the MgO mono- and bilayer. At an annealing temperature comprised between $58\,K \leq T_{ann} \leq 76\,K$, suddenly the abundance of Ho^{br} species reaches 100%, indicating that Ho^{O} species spontaneously hop to a bridge site. Uncertainties on T_{ann} are of $\pm 2\,K$ during the annealing (between $4.7\,K < T_{ann} < 76\,K$, and no uncertainty on T_{ann} is provided for $T_{ann} = 4.7\,K$ and $76\,K$ because the sample is thermalized with certainty with the liquid He or N$_2$ bath, respectively. Uncertainties on the abundances are calculated according to the binomial distribution for the Ho^{br} species. The data between $4.7\,K < T_{ann} < 45\,K$ correspond to abundances measured on a same region of the sample during the annealing of the sample, the slight variations are attributed to tip-induced transformation of the Ho species. The measurements at $T_{ann} \approx 58\,K$ correspond to another macroscopic region of the same sample.

4.2 Thermal stability of the Ho species

In order to get insights about the on-site (O or bridge) stability of the different Ho species, we tried annealing of the sample with simultaneous STM imaging. The sample was prepared as described in section 3.2 and the Ho atoms are evaporated on the sample at the deposition temperature $T_{dep} \approx 10\,K$. We then let the sample thermalize with the STM at the liquid helium temperature and, when the cryostat went empty of liquid helium, the STM started to heat. The annealing temperature T_{ann} is varied from 4.7 K to 77 K. During the annealing, we continued to image the sample surface with the STM and measured the abundance of the Ho species as a function of T_{ann}. The result is reported in Fig. 4.1 for the abundance of the Ho^{br} species (the abundance of the Ho^{O} species is the complementary of the data to 100%).

The first observation when looking at the data of Fig. 4.1 is that the change of abundance for Ho^{br} occurs between $T_{ann} = 58$ K and $T_{ann} = 77$ K on both 1 and 2 ML MgO. Between these temperatures, the abundance of Ho^{br} reaches 100% on both MgO layers. By definition, Ho^{br} is the equilibrium species because it is the one which is favored at high temperatures.

In principle, the temperature at which the Ho species start to diffuse gives information on the diffusion barrier, provided that we use the Arrhenius law [7] and that we know the hoping (and attempt) frequency at some temperature. In our case, we observed that at a temperature of $T_{ann} = 58$ K, the Ho^O and Ho^{br} adatoms were immobile at least over a scanning period of 15 minutes, that means that the hoping frequency of the Ho species is lower than $\nu \leq 1.1 \cdot 10^{-3}$ Hz. For the Arrhenius law parameter, we arbitrary chose an attempt frequency of $\nu_0 = 10^{12}$ Hz, usually good for adatoms at surfaces [116]. From these we can calculate the energy barrier to hop from the O site to the bridge site for $T_{ann} = 58$ K:

$$\nu = \nu_0 e^{-\frac{E^{O \to br}}{k_B T_{ann}}} \quad \Rightarrow \quad E^{O \to br} \geq k_B T_{ann} \ln\left(\frac{\nu_0}{\nu}\right) = 172 \text{ meV}, \tag{4.1}$$

with $k_B = 8.617$ meV K^{-1} the Boltzmann constant. At a temperature of $T_{ann} = 77$ K, we imaged the substrate with STM. We tried atomic manipulations and were not able to stabilise any Ho^O species, indicating that the thermal energy is high enough to induce spontaneous hoping of the manipulated Ho adatoms from O to bridge sites.

We can also to some extend evaluate the diffusion barrier energy for Ho adsorbed on MgO. Indeed, Ho^{br} adatoms are stable at least up to a temperature of $T_{ann} \approx 125$ K. We estimate that the hoping frequency at this temperature is smaller than $\nu = 10^{-2}$ Hz because we do not observe any formation of clusters after flash-annealing to $T_{ann} \approx 125$ K. The evaluation of the energy barrier for the diffusion holds:

$$E_{diff} \geq k_B T_{ann} \ln\left(\frac{\nu_0}{\nu}\right) = 347 \text{ meV}, \tag{4.2}$$

using again $\nu_0 = 10^{12}$ Hz.

The conclusions of the annealing experiment are striking:

- The favored Ho species at equilibrium is Ho^{br};

- The estimated energy barrier for the diffusion of Ho^{br} on the MgO surface is $E_{diff} \geq$ 347 meV;

- The Ho^O species hops from the O to the bridge site for a temperature comprised between 58 K and 77 K, thus the estimated energy barrier for this hoping is $E^{O \to br} \geq 172$ meV.

These conclusions are in direct competition with the observed abundances of Ho species for $T_{dep} = 10$ K, at least on 2 ML MgO, as reported in Tab. A.1 and Fig. 4.2. Indeed, even if on 1 ML MgO the majority species stays the Ho^{br} one, on 2 ML MgO there is a huge majority of the Ho^O species, thus clearly indicating that at low temperature ($T_{dep} = 10$ K), when the Ho atoms
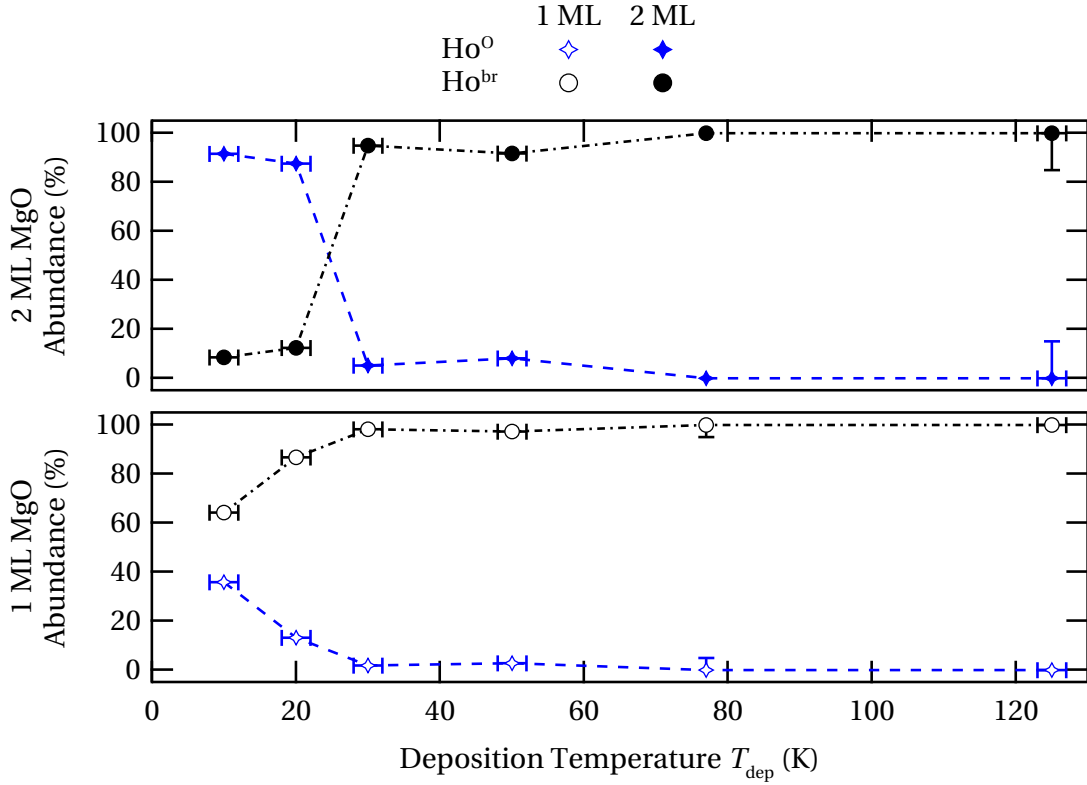
Figure 4.2 – Abundances of Ho^O and Ho^{br} species as a function of the deposition temperature T_{dep}. The dash-dotted and dashed lines are guide to the eyes. On 1 ML MgO, increasing T_{dep} lead to a monotonic increase (decrease) of Ho^{br} (Ho^O), while on 2 ML MgO, an inversion of the Ho species population occurs. Error bars smaller than the marker size were not reported.

are evaporated on the MgO surface, they prefer to finally adsorb on the O site, which is not the favored one at equilibrium. This observation is intriguing because one has to explain why the preferred adsorption site at low temperature is different from the one at equilibrium. A simple explanation is that the most favored adsorption site changes with the temperature. Thus it suggests a description of the system in terms of the free energy function $F = U - TS$, taking into account a term of entropy S, than using internal on-site energy function U. We will describe this approach in the following section.

4.3   Thermodynamical approach

Figure 4.2 shows the abundance ϑ of the Ho^{br} species as a function of the deposition temperature T_{dep}. On the MgO monolayer, the abundance of Ho^{br} species increases smoothly with T_{dep} and reaches already a value close to unity for $T_{dep} \geq 30$ K. On the MgO bilayer, the observations are much more interesting as for 20 K $\leq T_{dep} \leq 30$ K, the abundance of the Ho^{br} species changes from $\vartheta^{br} \approx 10\%$ to $\vartheta^{br} \approx 100\%$, indicating that between a little range of deposition temperature, the evaporated adatoms can reach or not the site favored at equilibrium, *i.e.*,
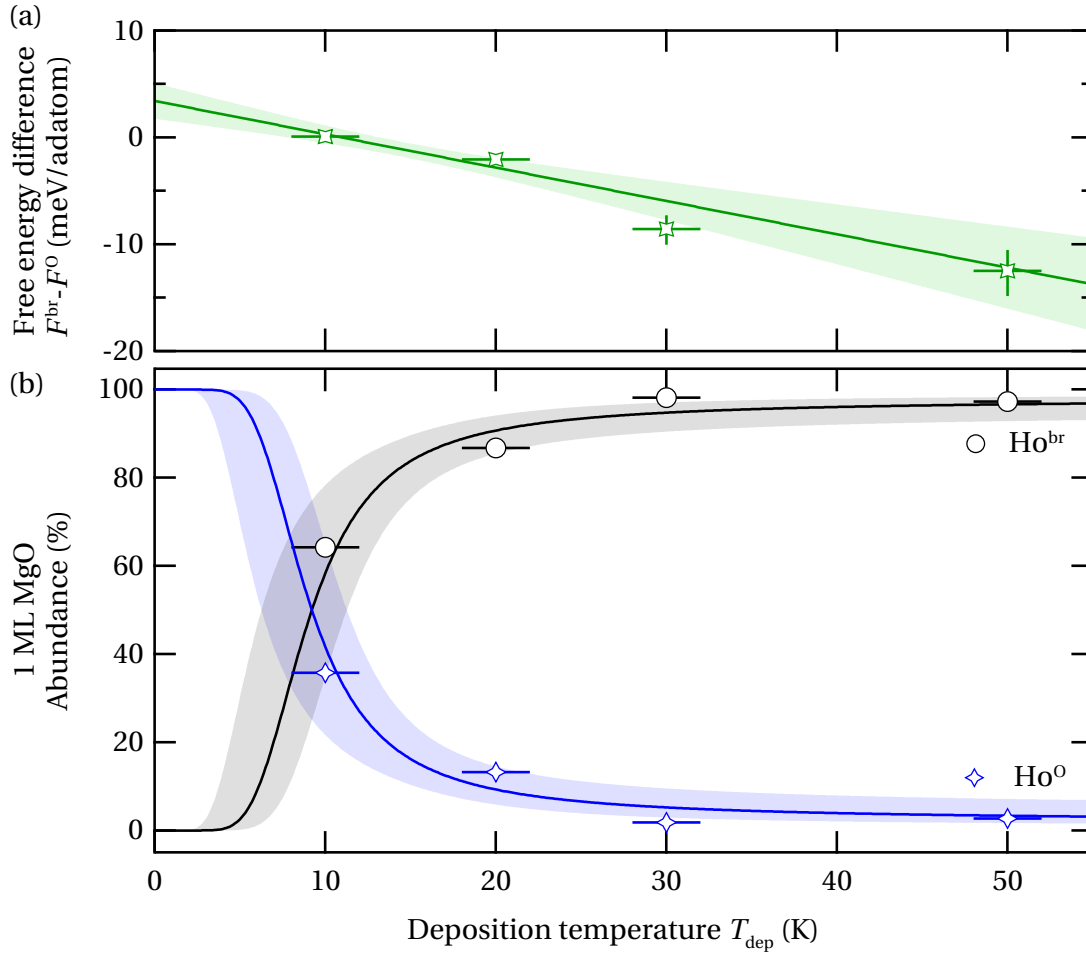
Figure 4.3 – Abundance of the Ho species on the MgO monolayer, understood in terms of Maxwell-Boltzmann statistics. (a) The free energy difference $\left(F^{\mathrm{br}} - F^{\mathrm{O}}\right)$ data point are reported. These are determined using the relation (4.5). The data points show an alignment suggesting in linear dependance of $\left(F^{\mathrm{br}} - F^{\mathrm{O}}\right)$ with the temperature T_{dep}. The green line represents the weighted least square fit to the data points in (a), and the light-green region corresponds to the 1σ uncertainty region around the fit line. Fit using the relation $\left(F^{\mathrm{br}} - F^{\mathrm{O}}\right) = \left(U^{\mathrm{br}} - U^{\mathrm{O}}\right) - \left(S^{\mathrm{br}} - S^{\mathrm{O}}\right) T_{\mathrm{dep}}$ returns $\left(S^{\mathrm{br}} - S^{\mathrm{O}}\right) = 0.31 \pm 0.11 \ \mathrm{meV \, K^{-1}}$ and $\left(U^{\mathrm{br}} - U^{\mathrm{O}}\right) = 3.4 \pm 1.7 \ \mathrm{meV}$. (b) The experimental data points for the abundance of $\mathrm{Ho^{O}}$ and $\mathrm{Ho^{br}}$ are reported. The blue and black curves correspond the Maxwell-Boltzmann equilibrium abundance calculated using the values of the fit in (a) for $\mathrm{Ho^{O}}$ and $\mathrm{Ho^{br}}$ respectively. The light-blue and light-black areas around the curves represent the extremal abundances associated with the light-green area of (a). The abscisse scale holds for both (a) and (b). Uncertainties smaller than the marker size were not reported.

(a)

(b)
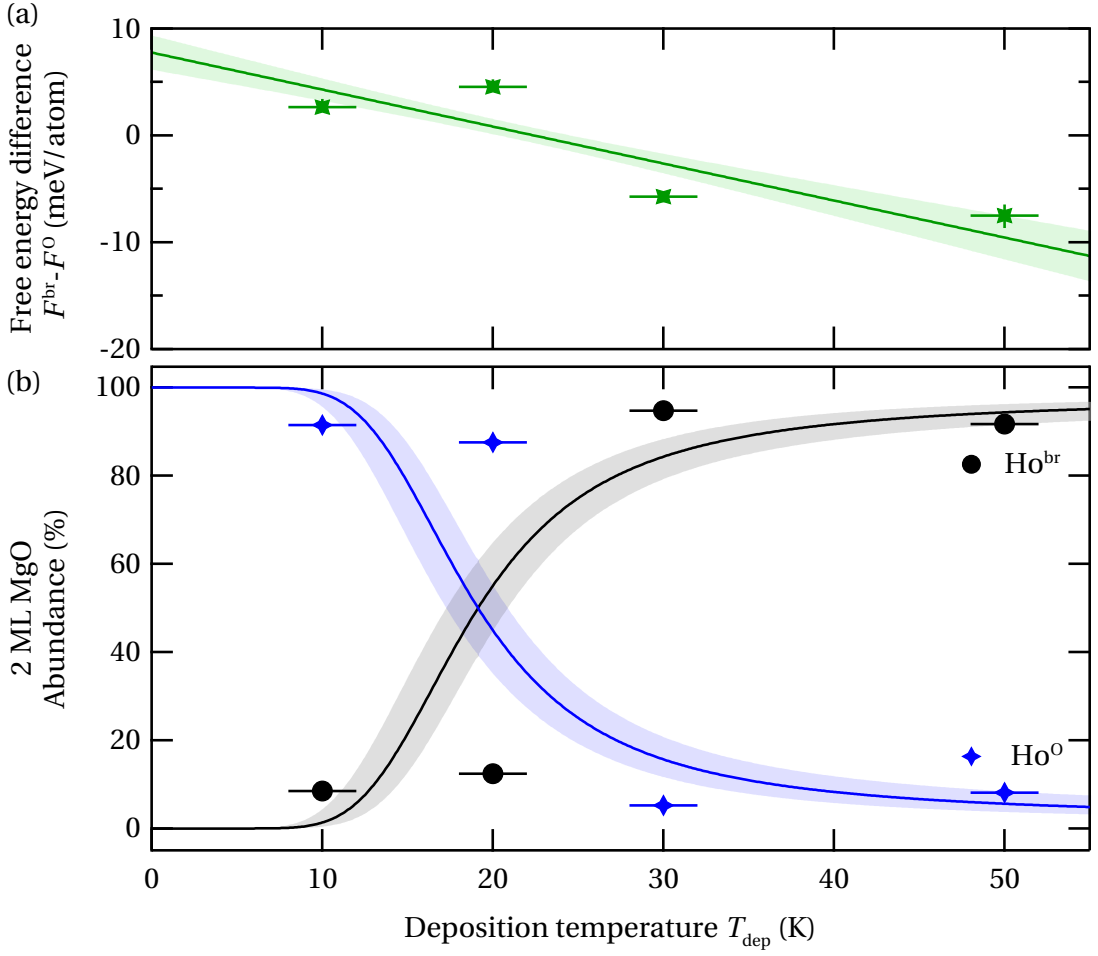
Figure 4.4 – Abundance of the Ho species on the MgO bilayer, understood in terms of Maxwell-Boltzmann statistics. (a) The free energy difference $\left(F^{\mathrm{br}} - F^{\mathrm{O}}\right)$ data point are reported. These are determined using the relation (4.5). The data points show an alignment suggesting in linear dependance of $\left(F^{\mathrm{br}} - F^{\mathrm{O}}\right)$ with the temperature T_{dep}. The green line represents the weighted least square fit to the data points in (a), and the light-green region corresponds to the 1σ uncertainty region around the fit line. Fit using the relation $\left(F^{\mathrm{br}} - F^{\mathrm{O}}\right) = \left(U^{\mathrm{br}} - U^{\mathrm{O}}\right) - \left(S^{\mathrm{br}} - S^{\mathrm{O}}\right) T_{\mathrm{dep}}$ returns $\left(S^{\mathrm{br}} - S^{\mathrm{O}}\right) = 0.35 \pm 0.07$ meV K^{-1} and $\left(U^{\mathrm{br}} - U^{\mathrm{O}}\right) = 7.6 \pm 1.6$ meV. (b) The experimental data points for the abundance of Ho$^{\mathrm{O}}$ and Ho$^{\mathrm{br}}$ are reported. The blue and black curves correspond the Maxwell-Boltzmann equilibrium abundance calculated using the values of the fit in (a) for Ho$^{\mathrm{O}}$ and Ho$^{\mathrm{br}}$ respectively. The light-blue and light-black areas around the curves represent the extremal abundances associated with the light-green area of (a). The abscisse scale holds for both (a) and (b). Uncertainties smaller than the marker size were not reported.

bridge site. Such a behavior *can* in principle be explained using a thermodynamical approach, disregarding the potential energy barriers existing for hoping between the different lattice sites[1]. The goal is to describe the abundance of the Ho species with the Maxwell-Boltzmann statistic, using the free energy $F^L = U^L - T S^L$ as thermodynamic function, with the superscript "L" standing for "O" or "br". In this description, U^L stands for the on-site internal energy of the Ho species, and S^L an associated entropy. We express the free energy for the Ho^O and Ho^{br} species, respectively, as

$$F^O = U^O - T_{dep} S^O \tag{4.3}$$
$$F^{br} = U^{br} - T_{dep} S^{br}, \tag{4.4}$$

From section 4.2, we understood that we cannot determine any of the U^L, because they would not correspond to the estimated diffusion energies (4.1) and (4.2). Nevertheless we could express the ratio of the abundance of the Ho species in the following form:

$$\frac{\vartheta^{br}}{\vartheta^O} \frac{1 - c\vartheta^O}{2 - c\vartheta^{br}} = e^{-\frac{(F^{br} - F^O)}{k_B T_{dep}}} = \exp\left(-\frac{U^{br} - U^O}{k_B T_{dep}} + \frac{S^{br} - S^O}{k_B}\right), \tag{4.5}$$

where the second fraction in the left-hand side of the relation (4.5) takes into account that the bridge sites are twice as more abundant than O at the surface, and $c = 0.005$ describes the Ho coverage, *i.e.*, the mean number of Ho adatoms per MgO unit cell. With this description, one could explain the change of inversion assuming the following hypothesis:

- The difference between the on-site energy $(U^{br} - U^O)$ should be small in order to populate both adsorption sites at low T_{dep},

- The change in the preferred adsorption site could be explained by a difference of entropy $(S^{br} - S^O)$ between the configurations of Ho adsorbed on the bridge and on the O lattice site.

Following this idea, we can use the data in Fig. 4.2 to calculate the free energy difference between Ho adsorbed on bridge and on O sites for each of the deposition temperatures T_{dep}. The result of this is reported in Fig. 4.3 and Fig. 4.4 for 1 and 2 ML MgO respectively.

The data markers in Figs. 4.3(a) and Fig. 4.4(a) report the free energy difference value $(F^{br} - F^O)$ for Ho adatoms on 1 and 2 ML MgO, respectively. These were calculated using the relation (4.5), and are more or less aligned. We fitted this data with a line function, using a least square model wighted by the uncertainties in abscisse and ordinate, and the result is reported with the green line; the light area around corresponds to the uncertainty region. The result of the line fit provides two quantities, $(U^{br} - U^O)$ and $(S^{br} - S^O)$, which are reported in Tab. 4.1. We first

---

[1] This assumption holds for the fact that transient mobility allows to overcome the diffusion barrier, at least for some jumps around the impinging position.

	$\left(U^{\mathrm{br}} - U^{\mathrm{O}}\right)$ (meV)	$\left(S^{\mathrm{br}} - S^{\mathrm{O}}\right)$ (meV K^{-1})
1 ML MgO	3.4 ± 1.7	0.31 ± 0.11
2 ML MgO	7.8 ± 1.6	0.35 ± 0.07

Table 4.1 – Difference between the on-site energy $\left(U^{\mathrm{br}} - U^{\mathrm{O}}\right)$ and entropy $\left(S^{\mathrm{br}} - S^{\mathrm{O}}\right)$ following the thermodynamical approach (4.5), for Ho adatoms on 1 and 2 ML MgO. These values do not vary a lot between both MgO layers.

observe that differences between 1 and 2 ML MgO, the two quantities returned by the fit do not differ too much between both MgO layers. The difference in on-site energy between Ho$^{\mathrm{br}}$ and Ho$^{\mathrm{O}}$ between both MgO layers are very close, and the difference in the entropy content between the two Ho species is the same, given the uncertainties. This indicates that with light of the thermodynamical model (4.5), both MgO layers are similar in terms of Ho adsorption result. Nevertheless, clear differences arise from the measured abundances ϑ^{O} and ϑ^{br}. This can be compared, on each MgO layers, in Figs. 4.3(b) and 4.4(b), where is reported the prediction of the thermodynamical model (4.5) with the parameters extracted from the fit in (a), see Tab 4.1. Clearly, the model explains the data on the MgO monolayer (Fig. 4.3), the increase of the Ho$^{\mathrm{br}}$ species as a function of T_{dep} is well caught by the model, including the uncertainty region associated from the variability in the parameters. On the MgO bilayer (Fig. 4.4), the model reproduces the inversion of the Ho species population but is unable to follow the sharp change imposed by the experimental data. This kind of discrepancy with the experimental data is not surprising. Very small changes in the parameters of the thermodynamical model have a big influence in the prediction of the Ho abundances, because the temperatures we are concerned with are very low (between 5 and 30 K).

In order to attest of the validity of the thermodynamic approach, we propose to combine the information about the thermal stability of the Ho adatoms presented in section 4.2 and the thermodynamical model (4.5). The idea is to propose one global free energy surface spanning the O and bridge lattice sites that evolves with the substrate temperature and explains why the Ho$^{\mathrm{O}}$ hopping to the bridge site occurs before the diffusion of the Ho at the MgO surface, even if adsorption on O lattice site is largely preffered at low temperature, on 2 ML MgO. For that we should establish the parameters of the relations (4.3) and (4.4), which are related between themselves, see Tab 4.1. Let us define the quantity $\delta U \equiv \left(U^{\mathrm{br}} - U^{\mathrm{O}}\right)$ and $\delta S \equiv \left(S^{\mathrm{br}} - S^{\mathrm{O}}\right)$, then the question resumes itself to find the magnitude for the quantities U^{O} and S^{O} such that

$$F^{\mathrm{O}}\left(T = 58\ \mathrm{K}\right) \quad = \quad U^{\mathrm{O}} - 58 \cdot S^{\mathrm{O}} \leq -172\ \mathrm{meV} \tag{4.6}$$

$$F^{\mathrm{br}}\left(T = 125\ \mathrm{K}\right) \quad = \quad \left(U^{\mathrm{O}} + \delta U\right) - 125\left(S^{\mathrm{O}} + \delta S\right) \leq -347\ \mathrm{meV}, \tag{4.7}$$

with δU and δS fixed and known. The conditions (4.6) and (4.7) allow in principle multiple solutions, and we will restraint ourself to the case with an equality. The solution is found

	U^{O} (meV)	S^{O} (meV K^{-1})	U^{br} (meV)	S^{br} (meV K^{-1})
1 ML MgO	-56 ± 13	2.02 ± 0.23	-52.6 ± 13	2.33 ± 0.23
2 ML MgO	-56.5 ± 9.5	2.01 ± 0.16	-48.7 ± 9.5	2.36 ± 0.16

Table 4.2 – On-site energy U^{L} and entropy S^{L} for Ho adatoms adsorbing on O and bridge lattice site. These values were empirically estimated by fitting the different constraints (see main text) on thermal stability and abundance of the Ho species.

graphically and is reported in Fig. 4.5(a). The blue curve corresponds to the free energy for an adatom adsorbing on the O lattice site. The light-blue area corresponds to the extremal regions for the blue line, taking into account the uncertainties in δU and δS; the data is centered around a first green marker which represents the relation (4.1). The black curve is also the free energy line for a Ho adatom, but adsorbing on the bridge lattice site, again with the light area representative for the uncertainty region. The latter curve is constrained to pass through a second green marker, which expresses the constraint (4.2).
From the Fig. 4.5, we can extract the quantities F^{O} and S^{O}, which are given in Tab. 4.2. Finally, from these values we can draw a sketch of the free energy potential landscape as a function of the position on a O-bridge line, and the temperature. This is reported in Fig. 4.5(b), with the color code representing the depth of the free energy potential well.

4.3.1 Discussion on the parameters of the thermodynamical model

This is not surprising that the values for entropy and on-site energy for the Ho$^{\mathrm{O}}$ and Ho$^{\mathrm{br}}$ are similar between the MgO monolayer and bilayer. Indeed, we would not expect a sharp change of the surface potential just by adding a MgO layer. What is more interesting is to look after the values U^{O}, S^{O}, δU and δS. First of all, the energy barriers at 0 K (U^{O} and U^{br}) are of the order of 50 meV. This is a very small value for what we are used to, but not exceptional as some systems, like Ce/Ag(111), do exhibit very low diffusion barrier [117, 118]. More interesting is about the justification we can find to understand the origin of the entropy that the thermodynamical model requires. We will construct the discussion on two points: What is the signification of S^{O} (S^{br}), and can we explain the difference of entropy δS between Ho$^{\mathrm{br}}$ and Ho$^{\mathrm{O}}$ adatoms.

Globally, the magnitude of the values of S^{O} and S^{br} are not so meaningful because any known source of entropy, such as magnetic degree of freedom or vibrations associated with the Ho adatoms, would explain an entropy magnitude of the order of 2 meV K^{-1}. What happens is that the model proposed uses two parameters, thus all the physics of the system will be caught and hidden in them. The quantity $\delta S \approx 0.3$meV K^{-1} for both MgO layers expresses the difference in entropy between the Ho$^{\mathrm{br}}$ and Ho$^{\mathrm{O}}$ adatoms, and thus carries valuable information. First of all, the question is about whether one could explain where could this entropy difference come from. We identify two possible origins for that:
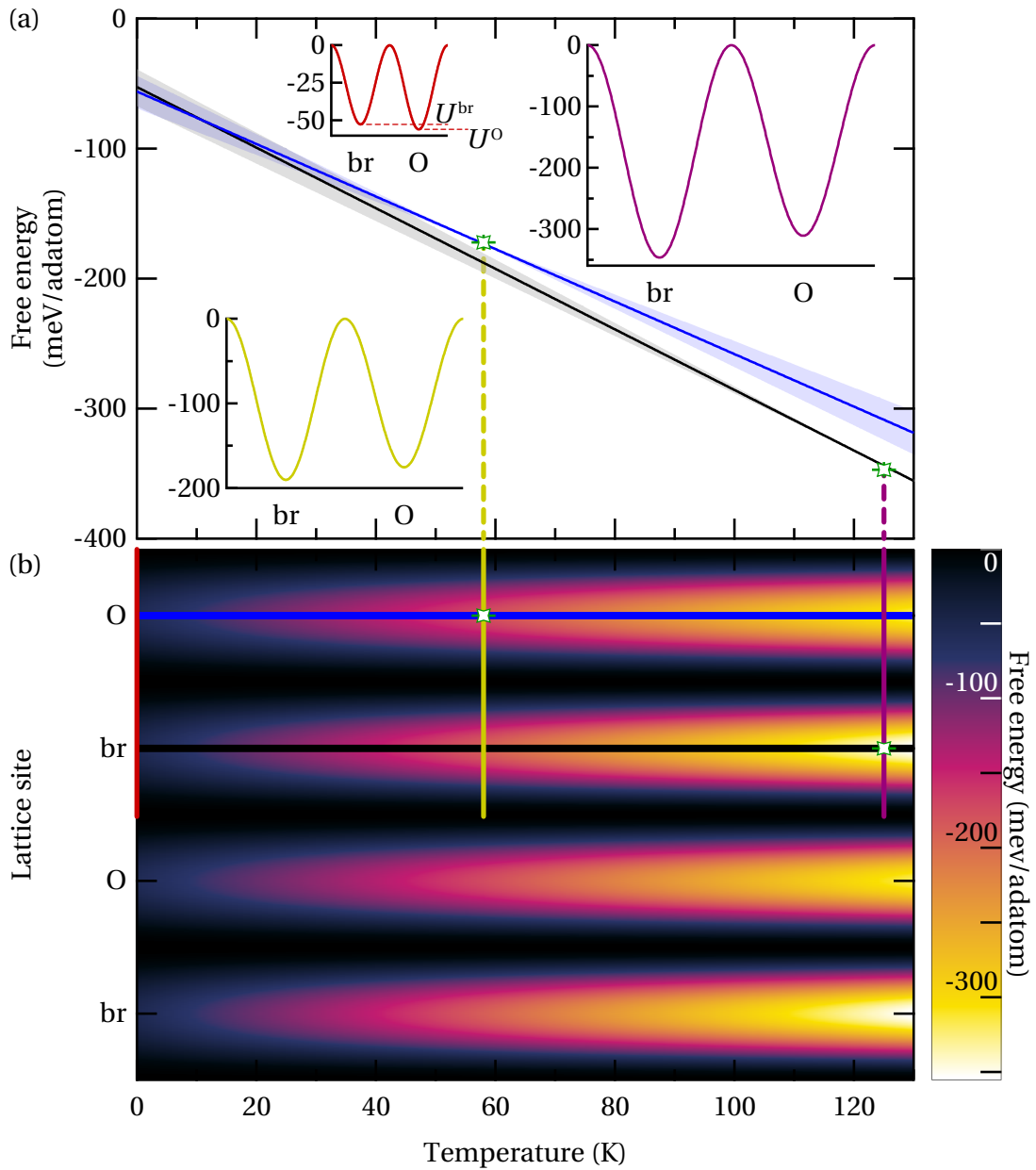
Figure 4.5 – (a) Blue and black lines correspond to the on-site (O: blue, and bridge: black) free energy magnitude as a function of the MgO temperature, see relations (4.3) and (4.4). The two green markers correspond to the condition expressed by the relations (4.1) and (4.2), *i.e.*, that the barriers for hopping of the Ho^O and Ho^{br} should be greater than 172 meV and 347 meV, respectively. (b) Free energy map explaining the experimental results in a qualitative way. The free energy magnitude varies from O to bridge lattice site, with higher magnitude for the O lattice site at 0 K. As the temperature increases, the bridge site becomes favored as it exhibit higher magnitude for the free energy, as evidenced by the three plots (*F* versus lattice site) in panel (a). Each plot correspond to a cut of the free energy in (b) along the MgO O-bridge line for different temperatures (red: 0 K, dark-yellow: 58 K and purple: 125 K). At 0 K, the depth of the free energy profile corresponds to U^{br} and U^O on bridge and O sites, respectively. The data shown here corresponds to the one established for the MgO monolayer, and is representative also of the MgO bilayer. Energy reference is fixed at the top of the diffusion barrier. 93

- Spin of the Ho adatom;

- Vibration of the adatom.

The Ho^O species is known to exhibit magnetic bistability, thus the magnetic moment of the atom can take two opposite orientations [80]. This is responsible for an entropy content of

$$S^O_{spin} = k_B \ln(2) \approx 60\,\mu\,eVK^{-1}. \tag{4.8}$$

Naturally, the same can be established for the Ho^{br} species. Natterer *et al.* [37] concluded from electron spin resonance that the total magnetic moment of the Ho^O species is of 10.1 ± 0.1 Bohr magneton. The total angular momentum proposed in their work holds $J = 8$ very close to the value of $J = 7$ proposed by Donati *et al.* [80]. We can assume that the total angular moment is independent of the adsorption site of the Ho adatoms and that only the groundstate configuration would depend on. Assuming $J = 8$ for the Ho^{br} species, we get a maximum of $2(J+1) = 17$ projections that can be very close in energy. The maximal entropy associated with this number of spin configurations of the Ho^{br}adatom holds

$$S^{br}_{spin} = k_B \ln(17) \approx 0.24\,meV\,K^{-1}. \tag{4.9}$$

We see that about 2/3 of the magnitude of δS could already be explained by the different spin configuration of the Ho adatoms species. One could additionally consider additional source of entropy difference between the two Ho species from the vibrational modes that the adatoms experiences. Nevertheless we could not advance any number because little is know about that.

To summarise the understanding of the quantities used in the thermodynamical approach, we coud state that one lacks of entropy sources to explain the results. Indeed, entropy magnitudes for S^O and S^{br} of the order or 2 meV K^{-1} are hard to explain. Nevertheless, we could imagine that our model is not fully representative of the reality. We should stress on the fact that we have no strong clues about the adsorption and relaxation process of the Ho adatoms at the surface, but we could imagine mechanisms which would explain the high values of S^O and S^{br}.

First of all, changes in the attempt frequencies of one order of magnitude has the global effect of increasing the magnitude of U^O and U^{br} to something about ~ -100 meV, with at the same time a reduction of the magnitude of S^O and S^{br} to ~ 1.6 meV K^{-1}. Naturally, the experimental data could not determine the value of the attempt frequency, but this information is attainable with experimental investigations.

Secondly, we can also consider a certain kind of selectivity of the different adsorption sites that would favor the occupation of one of them. In such picture we are no more in the Maxwell-Boltzmann description proposed, but this has the advantage that if both descriptions are in concurrence, then we can lower the part of entropy needed in the thermodynamical model. Selective processes that we thought about are the dependance of the transient mobility and impinging energy dissipation as a function of the impinging site. We recall that Gao *et al.* [105]

presented molecular dynamics simulations of the adsorption process of Pd on MgO. The main point that we retain is that the transient mobility of the adatom is highly dependent on the impinging site. As far as we have multiple adsorption sites for a species at the MgO surface, there is no reason for the transient mobility to select one of them [119]. Nevertheless, the transient mobility, or the sticking coefficient, could be different between O to bridge site, and that would favor an artificial increase of the abundance of one of the two species. We can also imagine that the efficiency of dissipation of the adsorption energy could vary from O to bridge site. In both picture, we can imagine to increase artificially the population of Ho^O species at low deposition temperature with such mechanisms, and that the increase of T_{dep} would only favor transient diffusion, whose species abundances would be described then by the thermodynamical model. These mechanisms are a way to reduce the entropy content needed in the thermodynamical model.

4.4 Conclusion

The results presented in this chapter testify of the whole complexity that simple systems can reveal. We presented experimental data on the abundance for the different Ho species, on 1 and 2 ML MgO. The interpretation was mainly constructed about the question whether we can describe the system with a simple thermodynamical model. The answer was partly positive, because we have to justify a large amount of entropy needed to explain the experimental data. To my mind the results of this chapter are appealing, justifying for deeper investigations that should answer two questions: Do every lanthanide element exhibit a change in the population abundance as a function of the deposition temperature? Is the thermodynamical model approach partially correct? If yes, this implies we could measure the difference in entropy between the Ho^O and Ho^{br} species just from a statistical analysis of the abundances.

In summary, even if we were not able to fully satisfactorily explain the experimental abundance of the Ho species, we put the finger on very uncommom results, *i.e.*, the change of a Ho species population at temperatures where thermal diffusion is clearly absent.

5 Conclusions and outlook

This thesis gives an overview of subjects studied during my PhD. It is composed of two different subjects because I got involved in two distinct projects.

In chapter 2 we presented the rotational quantum states spectroscopy for hydrogen and deuterium adsorbed on metallic substrates as well as on Xe islands. We have shown that the presence of the metallic substrate did not inhibit the excitation of the rotational levels of the physisorbed molecules. The energies measured for p-H_2 and o-D_2 correspond to these predicted for a 3D rigid rotor, for a change of the rotational quantum number of $J = 0 \rightarrow 2$. But all the measurements made on metal surfaces correspond to the probe of a bidimensional layer of H_2 or D_2 molecules, of variable density. Therefore, the excitations we measured could correspond to librons modes of this layer [120–125].

Our desire to probe an individual molecule with the STM oriented us to try to isolate them on a decoupling layer. We used Xe islands supported by the metal surface for that. The possibility to reduce the Xe islands size down to the single-atom was appealing, but revealed to introduce more questions that it should solve. Rotational spectroscopy for H_2 and D_2 physisorbed on the Xe islands is presented and the rotational excitation energies do not change compared to what is obtained on the bare metal substrate. But the combination of Xe and H_2 (or D_2) generates huge conductance steps in the differential conductance spectra. By chance [*sic*] this transition occurs at 46 meV for p-H_2 but has nothing to do with the excitation of the first rotational transition of the molecule. Additionally, in presence of H_2 (or D_2), small islands of Xe made of ~ 10 atoms are unstable, *i.e.*, one cannot expect to acquire spectroscopic data on islands whose atoms are not sufficiently bound between each other. This observation marked a pause in this first project, that finally last until the end of my PhD.

The study of the rotational properties of physisorbed H_2 (or D_2) on surfaces is nevertheless a very interesting project. Nobody reported the existence of rotational quantumstate excitation for the o-H_2 (p-D_2) with the STM. The results of the present thesis suggest they could be observed, should the scientist be patient enough to record a lot of spectra. We propose to continuously dose at very low pressures $\left(\sim 10^{-9} \text{ mbar} \right)$ normal hydrogen on the Ag(100)

metallic sample. Observation of both the $J = 0 \rightarrow 2$ and $J = 1 \rightarrow 3$ rotational transitions would definitively prove that the STM is capable of investigating the rotational quantumstates of homonuclear diatomic molecules. This opens the route for nuclear isospin configuration investigations with the STM.

The second project I got involved with is the determination of the adsorption site of Ho on MgO thin films grown on Ag(100) substrate. Rapidly this task attracted more and more time as it revealed that Ho/MgO(100)/Ag(100) system has very rich physics. First of all, to answer the question "what is the adsorption site of Ho on MgO?", we developed a method which relies only on *experimental investigations*. We used slight calcium doping of the MgO thin layers to identify some of the Mg lattice positions of the MgO surface. The experiment showed that the Ca atoms will always (we have no experimental counter-argument) be located on the topmost layer, thus we are able to identify the Mg lattice site on *each* layer where we subsequently evaporate the Ho metal atoms. Overlay of the MgO lattice onto the STM images allowed to identify the two adsorption sites for Ho: O and bridge site. We directly used Ho as marker for these sites on the MgO and additional investigations allowed to determine the adsorption sites of Er, Dy, Tb, Au, Co and Fe, see Tab. 3.5 for the summary.

Rapidly the scientific investigations of the Ho/MgO system opened new questions. The first one concerns the evolution with the substrate temperature of the abundance of the Ho^A and Ho^B species. To get deeper insight with the thermal properties of the adsorbed Ho, we estimated the temperature at which each species diffuses. What a surprise to notice that we had hard work to explain the experimental data with simple hypotheses! We concluded from this investigation that entropy should have an important effect. The two Ho^A and Ho^B species should not have the same entropy content, and the magnitude of this difference is of $1 \, \mathrm{meV \, K^{-1}}$, surprisingly high because we cannot establish which source of entropy would justify such difference. Generally speaking this is not the first time that entropy (of any form) has an influence in surface science [93, 126–129]. But according to our analyses, the Ho/MgO(100)/Ag(100) system should conceal very interesting physics!

The second interesting questions concerns the spectroscopic properties of the Ho_2 dimers. They are produced by evaporating more metal material on the MgO surface as well as with STM manipulations. STS investigations of these show an important increase in the differential conductance for energies of the order of 0.1 eV. We refer the reader to the Fig. 5.1 to get a flavor of these preliminary results. Transitions at such high energies for an adsorbed dimer are intriguing because they appear too high to be the testimony of magnetic excitations, but also at too low energies to be related to electronic transitions. Comparison with other species (Er, Tb[1], Dy[2]) showed that this feature is not limited to the Ho_2 dimer. We have here an

---

[1] Aparajita Singha first observed a differential conductance for Tb_2 dimers around bias of 0.12 V.
[2] Marina Pivetta observed similar differential conductance features for Dy_2 dimers.

additional starting point of investigations that extend the general study of rare-earth elements adsorbed on thin-insulating films.

Last, but surely not least, point concerns the experimental determination of the real MgO thickness on which the adatoms adsorb on. As far as our method of the Ca-doping of the MgO layers marks the Mg lattice sites position of the topmost layer, we are not concerned by this issue. Nevertheless, this point becomes crucial when one wants to compare the experimental data to the results of DFT calculations. All along this thesis we used the calibration for the MgO layer as reported by Silvia Schintke *et al.* [53], differing by 1 layer to the calibration reported by Wiliam Paul *et al.*, see section 7 of the supplementary information of reference [81]. This latter assures that our 1 ML MgO layers correspond to their 2 ML MgO ones, as they reported on the existence of a thiner layer. Therefore we tried to reproduce the measurement of Paul *et al.*, but were unable to exhibit one of their 1 ML MgO region as they report. Nevertheless across our experiments, we came to measure MgO layers exhibiting *only* one peak in the FER spectra, very similar to Fig. S15 in [81]. This was assigned to a MgO layer whose construction was not optimal due to the very low temperature used during the growth (620 K). Figure 5.2 shows the unique sample we produced having such FER spectroscopic characteristics. Clearly we cannot assume that we have grown a flat MgO layer. That motivates surely to look deeper into the multiple ways to prepare the MgO thin layers. Establishment of a recipe that could reproduce in large quantities the 1 ML MgO presented in Fig. 5.2, and possible comparison to what is reported by Paul *et al.*, would be of a valuable information and ask to reinterpret the DFT calculations in many published works [48, 80, 92, 109].

As a general conclusion I would like to mention that the work presented in this thesis is clearly not closing any surface-science domain that we studied directly or indirectly. Quite the reverse, we answered some important questions and I think we succeeded in identifying new investigations subjects that are fundamental. This is encouraging, the scientific knowledge is just asking for deeper investigation on the topics presented, that remains a matter of interest.
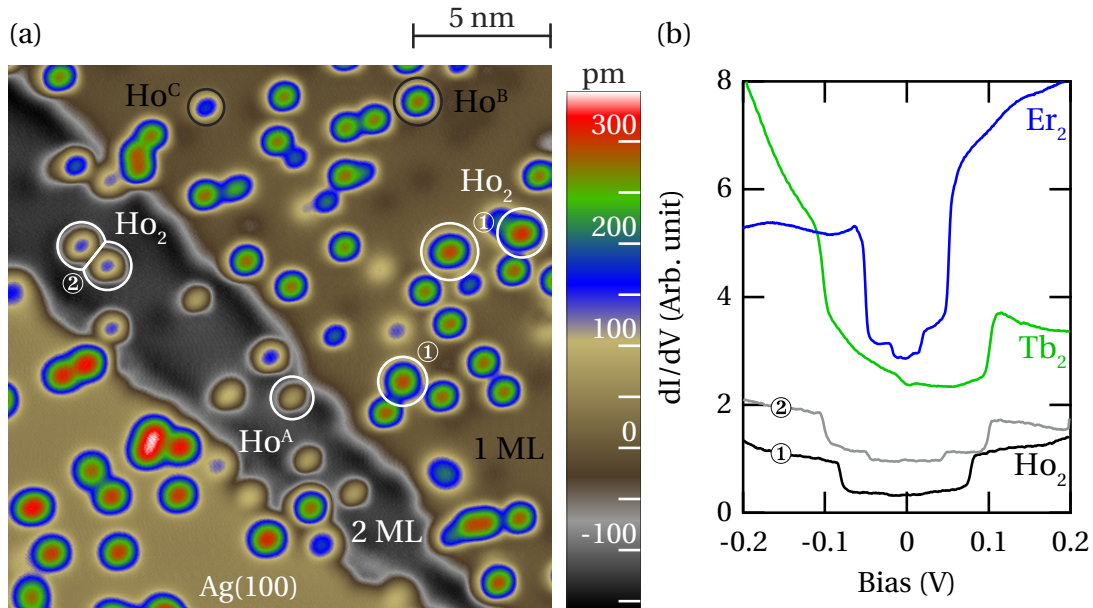
Figure 5.1 – (a) STM image Ho adatoms on 1 and 2 ML MgO. This image was recorded after having made some atomic manipulations as described in section 3.4, justifying the presence of Ho^C adatoms joint with the Ho^A and Ho^B. Objects with a white circle around are identified as Ho_2 dimers via their spectroscopic properties. (b) Differential conductance spectra for the Ho_2 objects of panel (a), as well as for Tb_2 and Er_2 dimers (STM image is not shown). The lanthanide dimers can be created with atomic manipulation, or by evaporating more metal material. In the STM image (a), Ho_2 were produced by atomic manipulations. Spectra labelled ① and ② refer to the protrusions with the same label in (a). In general, all the lanthanide dimers show an increase in the dI/dV spectra at energies ranging from ∼ 0.04 to ∼ 0.12 eV. Threshold energy can vary from element to element, but also between dimers adsorbed on a same MgO terrace (thus compound of the same metal element). Indeed, the inelastic steps show a certain variability inside an identical population of dimers. Finally we report here on the existence of multiple dimer species with the example of Ho_2 ① and ②. The first one displays only one conductance step, while the second exhibits two distinct ones. We suspect that Tb_2 and Er_2 have the same characteristics, and possibly other lanthanide dimers. Spectra for Ho_2 ①, ②, Tb_2 and Er_2 are averaged over 3, 2, 14 and 11 individual spectrum, respectively. STM image measurement conditions: $V_t = -100$ mV, $I_t = 100$ pA, $T_{STM} = 5$ K. Setpoint conditions for the spectroscopy: Ho: $V_t = -100$ mV, $I_t = 100$ pA; Tb: $V_t = -100$ mV, $I_t = 100$ pA; Er: $V_t = -200$ mV, $I_t = 200$ pA. All spectra were recorded with a peak-to-peak bias modulation of 2 mV at a frequency of 397 Hz.
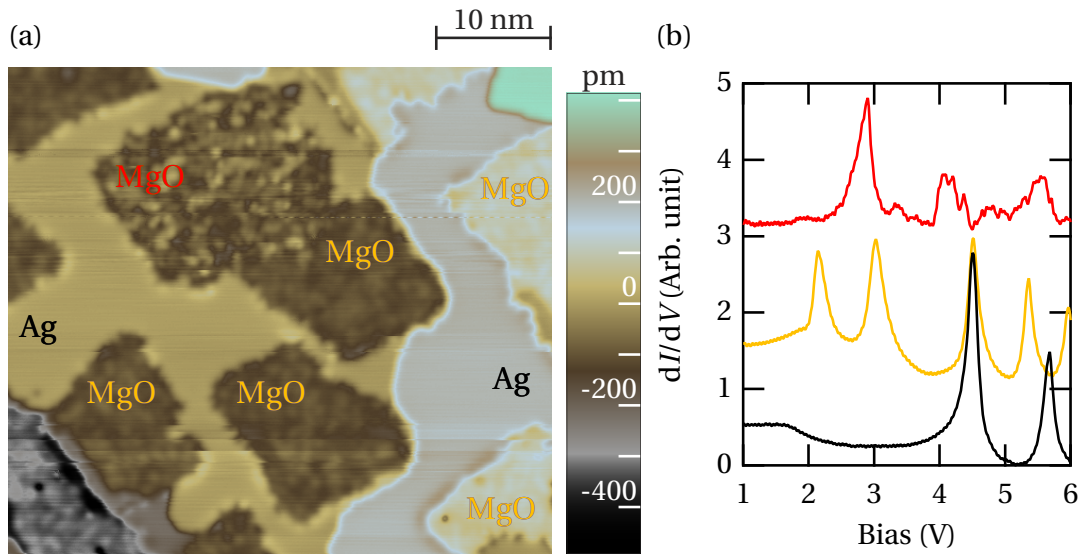
Figure 5.2 – (a) STM image of MgO grown by chemical vapor deposition. Mg is evaporated from a Knudsen cell toward the Ag(100) substrate held at low temperature (620 K), under 1×10^{-6} mbar of oxygen partial pressure. The total reaction time was 2 minutes. Large domains of Ag(100) surround the MgO patches which are not well formed. Their STM topography contrast is not flat, at variance to what is obtained for the MgO patches grown at higher temperature, see Fig. 3.1(a). (b) Field emission resonance spectroscopy of the different domains in (a). The spectroscopic curves are recorded on the Ag or MgO domains of the associated color in (a). The Ag patches display a pretty good flat surface. The MgO patches are better characterized by a granular surface, but we cannot inform whether this comes from a topological roughness or from a local change in the density of states. Note that MgO patches labelled in yellow or red do not exhibit the same FER spectra. The former shows two peaks, at higher bias to what is reported in Fig. 3.1(c). The latter exhibits only one peak at a bias of ~ 2.9 V. This should be compared to the Fig. S15 in reference [81]. Note that our result and the one of Paul *et al.* cannot be directly compared; we do not have a flat surface as they present in Fig. S14, and they measured dz/dV, where we measured dI/dV. Still the maxima in these spectroscopies should not depend on the spectroscopic method used. (V_t = 1 V, I_t = 100 pA, T_{STM} = 5 K, peak-to-peak modulation amplitude of 10 mV at a frequency of 1397 Hz).

Appendix

A Details about abundances of Ho species

A.1 Statistical test for Ho abundance for a deposition temperature $T_{\text{dep}} = 10$ K

For the following development, even if all the numerical calculations were done by myself, I am indebted to Prof. Clément Hongler, from the Chair of Statistical Field Theory at EPFL, who took his best patience to teach me how to setup a valid statistical test adapted to my problem.

Random occupancy of the O and bridge lattice sites (hereafter refered as *random statistics*) by the Ho atoms at the MgO surface would predict a Ho^A (Ho^B) abundance of exactly 1/3 (2/3), simply because the bridge site is twice as more abundant that the O one. Process producing such statistics would be explained from a direct adsorption of the impinging Ho atom on the lattice site it falls on. Atoms impinging on the Mg lattice site would be randomly redistributed around the nearby O or bridge lattice sites, or would better bounce and leave the system [105]. Nevertheless, the abundances of Ho^A for $T_{\text{dep}} = 10$ K, see Tab. A.1, including its uncertainty, do not cover the value of 1/3. The question now concerns whether one has to rule out random statistics or not. For that we conducted a statistical test asking if the random statistics hypothesis is compatible with the measured abundances at $T_{\text{dep}} = 10$ K. For that, we need to define the maximal deviation to 1/3 one would consider as acceptable. While counting the Ho^A and Ho^B objects from the experiment, there is an estimated fraction of 3% of unidentified objects. We will use this as sensitivity for our counting, that means that if the system follows a random statistics (RS) behavior, we could approach $\vartheta^{O,\,RS}$ by counting the Ho^A objects only with $\pm1.5\%$ of indetermination. We define $\mathcal{H}_0$ the hypothesis standing that the real (and unknown) $\vartheta^\star$, abundance of Ho^A on 1 ML MgO, is contained in the range $\vartheta^\star \in [0.318, 0.348]$, *i.e.*, $33.3\%\pm1.5\%$. The other hypothesis $\mathcal{H}_1$ expresses that $\vartheta^\star$ is outside this region, *i.e.*, $\vartheta^\star \in [0, 0.318[\cup]0.348, 1]$.

We describe broadly the hypothesis test we conducted. We define two hypothesis, $\mathcal{H}_0$ that the abundance ϑ of the Ho^A species fits inside the interval $[A, B]$ with $A = 0.318$ and $B = 0.348$,

Appendix A. Details about abundances of Ho species

$\mathcal{H}_1$ being the alternative hypothesis. We will use the method of the maximum likelihood ratio as described in [130].

The maximum likelihood function for a binomial distribution is defined by

$$\mathcal{L}(x, \vartheta) = \vartheta^x (1-\vartheta)^{N-x} \binom{N}{x}, \tag{A.1}$$

where $x \in \mathbb{N}$ is the number of time that Ho^A adatoms are observed and N the total number of counted Ho adatoms. We calculate the maximal value of the likelihood function under the assumption of the two hypothesis

$$\max_{\vartheta \in \mathcal{H}_0} \mathcal{L}(x, \vartheta) = \begin{cases} \mathcal{L}(x, \hat{\vartheta}) & \text{if } \hat{\vartheta} \in [A, B] \\ \mathcal{L}(x, A) & \text{if } \hat{\vartheta} < A \\ \mathcal{L}(x, B) & \text{if } \hat{\vartheta} > B \end{cases} \tag{A.2}$$

and

$$\max_{\vartheta \in \mathcal{H}_1} \mathcal{L}(x, \vartheta) = \begin{cases} \mathcal{L}(x, \hat{\vartheta}) & \text{if } \hat{\vartheta} \in [0, A[\bigcup]B, 1] \\ \mathcal{L}(x, A) & \text{if } A \leq \hat{\vartheta} \leq \frac{A+B}{2} \\ \mathcal{L}(x, B) & \text{if } \frac{A+B}{2} \leq \hat{\vartheta} \leq B \end{cases} \tag{A.3}$$

where $\hat{\vartheta} = \frac{x}{N}$ the best estimate to the true value of ϑ. The maximum of likelihood ratio F is given by

$$F(x, A, B, N) = \frac{\max_{\vartheta \in \mathcal{H}_0} \mathcal{L}(x, \vartheta)}{\max_{\vartheta \in \mathcal{H}_1} \mathcal{L}(x, \vartheta)} = \begin{cases} \frac{\mathcal{L}(x, A)}{\mathcal{L}(x, \hat{\vartheta})} & \text{if } \hat{\vartheta} < A \\ \frac{\mathcal{L}(x, \hat{\vartheta})}{\mathcal{L}(x, A)} & \text{if } A \leq \hat{\vartheta} \leq \frac{A+B}{2} \\ \frac{\mathcal{L}(x, \hat{\vartheta})}{\mathcal{L}(x, B)} & \text{if } \frac{A+B}{2} \leq \hat{\vartheta} \leq B \\ \frac{\mathcal{L}(x, B)}{\mathcal{L}(x, \hat{\vartheta})} & \text{if } \hat{\vartheta} > B \end{cases} \tag{A.4}$$

In our case, we have $\hat{\vartheta} = 0.358 \geq 0.348 \equiv B$, we can then calculate the value the function F takes:

$$F(x, A, B, N) = \left(\frac{B}{\hat{\vartheta}}\right)^x \left(\frac{1-B}{1-\hat{\vartheta}}\right)^{N-x} = 0.81. \tag{A.5}$$

We have now to compare this result to a value which will help us to discriminate between acceptance or not of $\mathcal{H}_0$. We define a function $T(x, A, B, N, \alpha)$ which tell us if we accept $\mathcal{H}_0$ with

$$T(x, A, B, N, \alpha) = \begin{cases} 0 & \text{if } F(x, A, B, N) \geq \alpha \quad \text{``}\mathcal{H}_0 \text{ is true''} \\ 1 & \text{if } F(x, A, B, N) < \alpha \quad \text{``}\mathcal{H}_1 \text{ is true.''} \end{cases} \tag{A.6}$$

The idea is now to find a way to calculate

$$\sup_{\vartheta \in \mathcal{H}_1} \mathbb{P}_\vartheta \left\{ T(x, A, B, N, \alpha) = 0 \right\}, \tag{A.7}$$

the probability that we get wrong when $\mathcal{H}_1$ is effectively true. Using the binomial probability density function suitable for your problem, the relation (A.7) expresses like

$$G(A, B, N, \alpha) = \sup_{\vartheta \in \mathcal{H}_1} \left\{ \sum_{k=0}^{N} \left[1 - T(k, A, B, N, \alpha) \right] \vartheta^k (1 - \vartheta)^{N-k} \binom{N}{k} \right\}. \tag{A.8}$$

We can compute numerically the result of (A.8). For that we plot the function G and we look for the maximal value of α at the level $G = 0.005$. We get a value of $\alpha = 0.1$, and thus we have $F > \alpha$ implying that we cannot reject $\mathcal{H}_0$. Random statistics could explain the abundance of the Ho species for $T_{\text{dep}} = 10$ K. In this picture the Ho atoms do not explore the MgO surface: they better adsorb directly on the MgO if possible. Please note that the statistical test does not tell us what is happening on the surface when the Ho atoms impinge on. The statistical test just tell us that we cannot rule out the random statistics explanation, at least for the present number of counted adatoms.

A.2 Table of Ho species abundance for different deposition temperatures T_{dep}

		$T_{dep}=10$ K		$T_{dep}=20$ K		$T_{dep}=30$ K		$T_{dep}=50$ K		$T_{dep}=77$ K		$T_{dep}=125$ K	
		ϑ (%)	N	ϑ (%)	N	ϑ (%)	N	ϑ (%)	N	ϑ (%)	N	ϑ (%)	N
1 ML MgO	Ho^A	$35.8^{+1.6}_{-1.5}$	339	$13.2^{+1.0}_{-1.0}$	148	$1.8^{+0.6}_{-0.5}$	11	$2.7^{+1.1}_{-0.9}$	7	$0^{+4.9}_{-0}$	0	$0^{+2.5}_{-0}$	0
	Ho^B	$64.2^{+1.5}_{-1.6}$	608	$86.8^{+1.0}_{-1.0}$	977	$98.2^{+0.5}_{-0.6}$	610	$97.3^{+0.9}_{-1.1}$	252	$100^{+0}_{-4.9}$	10	$100^{+0}_{-2.5}$	20
2 ML MgO	Ho^A	$91.5^{+1.6}_{-1.8}$	260	$87.6^{+1.3}_{-1.4}$	535	$5.2^{+1.0}_{-0.9}$	29	$8.1^{+2.0}_{-1.8}$	17	0^{+1}_{-0}	0	0^{+15}_{-0}	0
	Ho^B	$8.5^{+1.8}_{-1.6}$	24	$12.4^{+1.4}_{-1.3}$	76	$94.8^{+0.9}_{-1.0}$	526	$91.9^{+1.8}_{-2.0}$	192	100^{+0}_{-1}	49	100^{+0}_{-15}	3
3 ML MgO	Ho^A	—	—	$86.4^{+6.2}_{-8.4}$	19	0^{+8}_{-0}	0	—	—	$0^{+6.1}_{-0}$	0	—	—
	Ho^B	—	—	$13.6^{+8.4}_{-6.2}$	3	100^{+0}_{-8}	6	—	—	$100^{+0}_{-6.1}$	8	—	—

Table A.1 – Number N of Ho^A and Ho^B adatoms counted on 1, 2 and 3 ML MgO over many STM images, for samples prepared at different T_{dep}, and the correspondent abundances ϑ. Data for $T_{dep}=10$ K is the same as the one presented in Tab. 3.1. Between 20 K $\leq T_{dep} \leq$ 30 K, the Ho^A and Ho^B population tendency is inverted for 2 ML MgO and more. (—) means that no data has been measured.

B | Coloring the STM images

One particularity of this thesis manuscript is, to my mind, the abundance of the STM images. These carry physical information in three directions (X-, Y- and Z- dimensions), this is why they are represented mostly as 3D topographic images. The STM image width and height directly inform on the size of the objects (X- and Y- dimensions), but one can also use color-coding in the images such that it carries vertical information (Z-dimension). Most of the STM images presented in this manuscript are accompanied with the color-table encoding the physical height (mostly in picometer) of the objects; color-table for one image is pretty straightforward to implement. Nevertheless, it happens that in some situations one is interested in having the same color-table for two (or more) independent STM images, *i.e.*, that the same absolute height on each of the two (or more) images is represented by exactly the same color, and this becomes tricky specially if both images do not span the same physical Z-range. After having looked into possibly existing software solutions for this task, I decided to develop my own code to create lookup-table that have been used to color all the STM images I presented during my thesis experience. My solution, although this is perhaps not the best, combines the use of ImageJ [131] and Igor Pro softwares [132]. The workflow is the following:

1. Open the STM image(s) with ImageJ, make all the standard treatment required (like plane subtraction) and export it as a **text image**. Exporting in this format creates simply a text file with as many rows and columns than the STM image pixels width and height number. The values of this text file contains the physical Z-value.

2. Open the Igor Pro software and run the *LutGenerator*(k) macro. The argument k of this macro has to be the number of images for which one wants a common lookup-table (up to 4).

3. In the *LutGenerator* panel, load the STM image(s) within the text file.

4. Move the cursors in the panel to tune the appearance of the color-table.

5. When finished, one can save the color-table as a text lookup-table directly usable in ImageJ. Directly after that, the macro pops-up for saving all the parameters needed to recreate this color-table.

6. In ImageJ, simply drag the lookup-table on the image of interest. The color-table is applied to the right image.

In case we want to color multiple images, one can save each lookup-table specific to the individual images, but also the full global color-table. In this case, the lookup-table of the individual images will be a subset of the global lookup-table. Examples of these are found in this thesis, for example Figs. 3.5, 3.4, 3.8, 3.22 or 3.25.

The Igor Pro macro was designed for a very personal use. Therefore for it to work, some data-waves have to be present in the experiment. The best way of using this kind of macro is to have an Igor Pro file uniquely dedicated to this task, that will be left on the group server, or to Marina Pivetta. Nevertheless, I will transpose hereafter the macro code, which is a combination of multiple functions definitions. The lines ending with the following character "↓" specify a line carriage-return in the present document that is avoided in the Igor Pro code; sometimes the code lines are wider that the present document page.

```
#pragma rtGlobals=3 // Use modern global access method and strict ↓
wave access.

Function Initialisation(num)
    Variable num
    Make/O/N=(256,3) Spectre, Spectre_1, Spectre_2, Spectre_3, Spectre_4
    Variable a, b
    if(num == 1)
        wave wave0 = $"ImageText_to_LUT10"
        SetScale/I x WaveMin(wave0),WaveMax(wave0),"pm", Spectre
        SetScale/I x WaveMin(wave0),WaveMax(wave0),"pm", Spectre_1
    elseif(num == 2)
        wave wave0 = $"ImageText_to_LUT10"
        wave wave1 = $"ImageText_to_LUT20"
        SetScale/I x min(WaveMin(wave0), WaveMin(wave1)), ↓
            max(WaveMax(wave0), WaveMax(wave1)),"pm", Spectre
        SetScale/I x WaveMin(wave0),WaveMax(wave0),"pm", Spectre_1
        SetScale/I x WaveMin(wave1),WaveMax(wave1),"pm", Spectre_2
    elseif(num == 3)
        wave wave0 = $"ImageText_to_LUT10"
        wave wave1 = $"ImageText_to_LUT20"
        wave wave2 = $"ImageText_to_LUT30"
        SetScale/I x min(min(WaveMin(wave0), WaveMin(wave1)), ↓
                WaveMin(wave2)), max(max(WaveMax(wave0), WaveMax(wave1)), ↓
                WaveMax(wave2)), "pm", Spectre
```

```
        SetScale/I x WaveMin(wave0),WaveMax(wave0),"pm", Spectre_1
        SetScale/I x WaveMin(wave1),WaveMax(wave1),"pm", Spectre_2
        SetScale/I x WaveMin(wave2),WaveMax(wave2),"pm", Spectre_3
    elseif(num == 4)
        wave wave0 = $"ImageText_to_LUT10"
        wave wave1 = $"ImageText_to_LUT20"
        wave wave2 = $"ImageText_to_LUT30"
        wave wave3 = $"ImageText_to_LUT40"
        SetScale/I x min(min(min(WaveMin(wave0), WaveMin(wave1)), ↓
                WaveMin(wave2)), WaveMin(wave3)), max(max(max(WaveMax(wave0), ↓
                WaveMax(wave1)), WaveMax(wave2)), WaveMax(wave3)), ↓
                "pm", Spectre
        SetScale/I x WaveMin(wave0),WaveMax(wave0),"pm", Spectre_1
        SetScale/I x WaveMin(wave1),WaveMax(wave1),"pm", Spectre_2
        SetScale/I x WaveMin(wave2),WaveMax(wave2),"pm", Spectre_3
        SetScale/I x WaveMin(wave3),WaveMax(wave3),"pm", Spectre_4
    endif
    Wave Apercu
    Apercu[][] = (DimSize(Spectre, 0)*DimDelta(Spectre, 0))/ ↓
        (DimSize(Apercu, 0)-1)*p + DimOffset(Spectre, 0)
End

Window LutGenerator(NumImages) : Panel
    Variable NumImages
    Parametres[16] = NumImages
    PauseUpdate; Silent 1       // building window...
    //Taille de la fenêtre
    if(NumImages == 1)
        NewPanel/K=1/W=(10, 50, 1022, 862) as "LutGenerator_1Im"
    endif
    if(NumImages == 2)
        NewPanel/K=1/W=(10, 50, 1524, 862) as "LutGenerator_2Im"
    endif
    if(NumImages == 3)
        NewPanel/K=1/W=(10, 50, 1022, 950) as "LutGenerator_3Im"
    endif
    if(NumImages >= 4)
        NewPanel/K=1/W=(10, 50, 1022, 950) as "LutGenerator_4Im"
    endif

    ShowTools/A
```

```
//Ajout des commandes
//Gauche
Slider GrayLinLoc,pos=0,0,size=150,45,proc=SliderProc
Slider GrayLinLoc,limits=0,100,0.1,value= Parametres[2],vert= 0, ↓
    ticks= 20
SetVariable SetGrayLinLoc,pos=160,0,size=120,19,proc=UpdateSlider, ↓
    title="Gray/"
SetVariable SetGrayLinLoc,fSize=12,limits=0,100,0.1, ↓
    value= Parametres[2]
//
Slider Loc1,pos=0,50,size=150,45,proc=SliderProc
Slider Loc1,limits=0,100,0.1,value= Parametres[4],vert= 0,ticks= 20
SetVariable SetLoc1,pos=160,50,size=120,19,proc=UpdateSlider, ↓
    title="Loc 1"
SetVariable SetLoc1,fSize=12,limits=0,100,0.1,value= Parametres[4]
//
Slider Loc2,pos=0,100,size=150,45,proc=SliderProc
Slider Loc2,limits=0,100,0.1,value= Parametres[5],vert= 0,ticks= 20
SetVariable SetLoc2,pos=160,100,size=120,19,proc=UpdateSlider, ↓
    title="Loc 2"
SetVariable SetLoc2,fSize=12,limits=0,100,0.1,value= Parametres[5]
//
Slider Loc3,pos=0,150,size=150,45,proc=SliderProc
Slider Loc3,limits=0,100,0.1,value= Parametres[6],vert= 0,ticks= 20
SetVariable SetLoc3,pos=160,150,size=120,19,proc=UpdateSlider, ↓
    title="Loc 3"
SetVariable SetLoc3,fSize=12,limits=0,100,0.1,value= Parametres[6]
//
Slider Loc4,pos=0,200,size=150,45,proc=SliderProc
Slider Loc4,limits=0,100,0.1,value= Parametres[7],vert= 0,ticks= 20
SetVariable SetLoc4,pos=160,200,size=120,19,proc=UpdateSlider, ↓
    title="Loc 4"
SetVariable SetLoc4,fSize=12,limits=0,100,0.1,value= Parametres[7]
//
Slider Loc5,pos=0,250,size=150,45,proc=SliderProc
Slider Loc5,limits=0,100,0.1,value= Parametres[8],vert= 0,ticks= 20
SetVariable SetLoc5,pos=160,250,size=120,19,proc=UpdateSlider, ↓
    title="Loc 5"
SetVariable SetLoc5,fSize=12,limits=0,100,0.1,value= Parametres[8]
//Milieu
Slider ShadeLeft,pos=300,0,size=150,45,proc=SliderProc
Slider ShadeLeft,limits=0,100,0.1,value= Parametres[3],vert= 0, ↓
```

```
      ticks= 20
SetVariable SetShadeLeft,pos=460,0,size=120,19,proc=UpdateSlider, ↓
   title="\\W648"
SetVariable SetShadeLeft,fSize=12,limits=0,100,0.1,value= Parametres[3]
//
Slider ShadeRight,pos=300,50,size=150,45,proc=SliderProc
Slider ShadeRight,limits=0,100,0.1,value= Parametres[9],vert= 0, ↓
   ticks= 20
SetVariable SetShadeRight,pos=460,50,size=120,19,proc=UpdateSlider, ↓
   title="\\W645"
SetVariable SetShadeRight,fSize=12,limits=0,100,0.1,value= Parametres[9]
//
Slider GrayLinL,pos=300,100,size=150,45,proc=SliderProc
Slider GrayLinL,limits=0,1,0.01,value= Parametres[10],vert= 0,ticks= 3
SetVariable SetGrayLinL,pos=460,100,size=120,19,proc=UpdateSlider, ↓
   title="GrayL"
SetVariable SetGrayLinL,fSize=12,limits=0,1,0.01,value= Parametres[10]
//
Slider GrayLinR,pos=300,150,size=150,45,proc=SliderProc
Slider GrayLinR,limits=0,1,0.01,value= Parametres[11],vert= 0,ticks= 3
SetVariable SetGrayLinR,pos=460,150,size=120,19,proc=UpdateSlider, ↓
   title="GrayR"
SetVariable SetGrayLinR,fSize=12,limits=0,1,0.01,value= Parametres[11]
//
Slider GrayE,pos=300,200,size=150,45,proc=SliderProc
Slider GrayE,limits=0,1,0.01,value= Parametres[12],vert= 0,ticks= 3
SetVariable SetGrayE,pos=460,200,size=120,19,proc=UpdateSlider, ↓
   title="GrayE"
SetVariable SetGrayE,fSize=12,limits=0,1,0.01,value= Parametres[12]
//
Slider Purple,pos=300,250,size=150,47,proc=SliderProc
Slider Purple,limits=-1,1,0.01,value= log(Parametres[17]),vert= 0
Slider Purple,userTicks=TicksVal,TickText
SetVariable SetPurple,pos=460,250,size=120,19,proc=UpdateSlider, ↓
   title="GamG"
SetVariable SetPurple,fSize=12,limits=0.1,10,0.01,value= Parametres[17]
//Droite
Slider Gam,pos=600,0,size=150,47,proc=SliderProc
Slider Gam,limits=-1,1,0.01,value= log(Parametres[14]),vert= 0, ↓
   userTicks=TicksVal,TickText
SetVariable SetGam,pos=760,0,size=120,19,proc=UpdateSlider, ↓
   title="Gamma"
```

```
SetVariable SetGam,fSize=12,limits=0.1,10,0.01,value= Parametres[14]
//
Slider Light,pos=600,50,size=150,45,proc=SliderProc
Slider Light,limits=0,1,0.01,value= Parametres[15],vert= 0,ticks= 3
SetVariable SetLight,pos=760,50,size=120,19,proc=UpdateSlider, ↓
    title="Light"
SetVariable SetLight,fSize=12,limits=0,1,0.01,value= Parametres[15]
//Boutons de chargement des images et de sauvegarde des LUT
if(NumImages >= 2)
    Button LUTSaver0,pos=890,25,size=100,20,proc=SaveLUT, ↓
        title="Save Glob LUT"
endif
if(NumImages >= 1)
    Button ImageLoader1,pos=600,100,size=150,20,proc=LoadImage, ↓
        title="Load Image 1"
    Button LUTSaver1,pos=800,100,size=150,20,proc=SaveLUT, ↓
        title="Save LUT 1"
endif
if(NumImages >=2)
Button ImageLoader2,pos=600,150,size=150,20,proc=LoadImage, ↓
    title="Load Image 2"
Button LUTSaver2,pos=800,150,size=150,20,proc=SaveLUT, ↓
    title="Save LUT 2"
endif
if(NumImages >= 3)
    Button ImageLoader3,pos=600,200,size=150,20,proc=LoadImage, ↓
        title="Load Image 3"
    Button LUTSaver3,pos=800,200,size=150,20,proc=SaveLUT, ↓
        title="Save LUT 3"
endif
if(NumImages >=4)
Button ImageLoader4,pos=600,250,size=150,20,proc=LoadImage, ↓
    title="Load Image 4"
Button LUTSaver4,pos=800,250,size=150,20,proc=SaveLUT, ↓
    title="Save LUT 4"
endif
//Construction des sous-fenêtres

//Petit graph avec la LUT
if(NumImages == 1)
    Display/W=(512,300,1012,556)/HOST=#  Spectre[*][0],Spectre[*][1], ↓
        Spectre[*][2]
```

```
endif
if(NumImages == 2)
    Display/W=(1024,300,1524,556)/HOST=#  Spectre[*][0],Spectre[*][1], ↓
        Spectre[*][2]
endif
if(NumImages == 3)
    Display/W=(600,300,1012,600)/HOST=#  Spectre[*][0],Spectre[*][1], ↓
        Spectre[*][2]
endif
if(NumImages >= 4)
    Display/W=(600,300,1012,600)/HOST=#  Spectre[*][0],Spectre[*][1], ↓
        Spectre[*][2]
endif
AppendImage/T Apercu
ModifyImage Apercu cindex= Spectre16bit
ModifyGraph margin(left)=14,margin(bottom)=14,margin(top)=28, ↓
    margin(right)=14
ModifyGraph rgb(Spectre#1)=(0,65535,0),rgb(Spectre#2)=(0,0,65535)
ModifyGraph tick=3
ModifyGraph mirror(left)=2,mirror(bottom)=0,mirror(top)=0
ModifyGraph nticks(left)=6,nticks(top)=6
ModifyGraph minor(left)=1,minor(top)=1
ModifyGraph noLabel=2
ModifyGraph fSize(left)=9,fSize(top)=9
ModifyGraph standoff(left)=0,standoff(top)=0
ModifyGraph tkLblRot(left)=90
ModifyGraph btLen(left)=3,btLen(top)=3
ModifyGraph tlOffset(left)=-2,tlOffset(top)=-2
SetAxis/R left 0,255
ModifyGraph margin=3
RenameWindow #,LUT
SetActiveSubwindow ##

//Lumière
if(NumImages == 1)
    Display/W=(512,556,1012,812)/HOST=#  Lumiere
endif
if(NumImages == 2)
    Display/W=(1024,556,1524,812)/HOST=#  Lumiere
endif
if(NumImages == 3)
    Display/W=(600,600,1012,900)/HOST=#  Lumiere
```

```
    endif
if(NumImages >= 4)
    Display/W=(600,600,1012,900)/HOST=#  Lumiere
endif
ModifyGraph grid(left)=1
ModifyGraph tick(left)=2,tick(bottom)=3
ModifyGraph mirror=1
ModifyGraph noLabel(bottom)=2
ModifyGraph standoff=0
ModifyGraph manTick(left)=0,1,0,0,manMinor(left)=9,2
SetAxis left 0,1
TextBox/C/N=text0/F=0/A=MC/X=0/Y=40 "Lumière"
ModifyGraph margin=3
RenameWindow #,Lumiere
SetActiveSubwindow ##

//Image 1
if(NumImages == 1)
    Display/W=(0,300,512,812)/HOST=#
endif
if(NumImages == 2)
    Display/W=(0,300,512,812)/HOST=#
endif
if(NumImages == 3)
    Display/W=(0,300,300,600)/HOST=#
endif
if(NumImages >= 4)
    Display/W=(0,300,300,600)/HOST=#
endif
AppendImage/T ImageText_to_LUT10
ModifyImage ImageText_to_LUT10 cindex= Spectre16bit
ModifyGraph margin(left)=14,margin(bottom)=14,margin(top)=14, ↓
    margin(right)=14,width=Aspect,1
ModifyGraph tick=3
ModifyGraph mirror=0
ModifyGraph nticks=10
ModifyGraph minor=1
ModifyGraph noLabel=2
ModifyGraph fSize=9
ModifyGraph standoff=0
ModifyGraph tkLblRot(left)=90
ModifyGraph btLen=3
```

```
ModifyGraph tlOffset=-2
SetAxis/A/R left
ModifyGraph margin=3
ModifyGraph swapXY=1
RenameWindow #,Image1
SetActiveSubwindow ##

//Image 2
if(NumImages == 2)
   Display/W=(512,300,1024,812)/HOST=#
endif
if(NumImages == 3)
   Display/W=(300,300,600,600)/HOST=#
endif
if(NumImages >= 4)
   Display/W=(300,300,600,600)/HOST=#
endif
if(NumImages >= 2)
   AppendImage/T ImageText_to_LUT20
   ModifyImage ImageText_to_LUT20 cindex= Spectre16bit
   ModifyGraph margin(left)=14,margin(bottom)=14,margin(top)=14, ↓
      margin(right)=14,width=Aspect,1
   ModifyGraph tick=3
   ModifyGraph mirror=0
   ModifyGraph nticks=10
   ModifyGraph minor=1
   ModifyGraph noLabel=2
   ModifyGraph fSize=9
   ModifyGraph standoff=0
   ModifyGraph tkLblRot(left)=90
   ModifyGraph btLen=3
   ModifyGraph tlOffset=-2
   SetAxis/A/R left
   ModifyGraph margin=3
   ModifyGraph swapXY=1
   RenameWindow #,Image2
   SetActiveSubwindow ##
endif

//Image 3
if(NumImages == 3)
   Display/W=(0,600,300,900)/HOST=#
```

```
      endif
   if(NumImages >= 4)
      Display/W=(0,600,300,900)/HOST=#
   endif
   if(NumImages >= 3)
      AppendImage/T ImageText_to_LUT30
      ModifyImage ImageText_to_LUT30 cindex= Spectre16bit
      ModifyGraph margin(left)=14,margin(bottom)=14,margin(top)=14, ↓
         margin(right)=14,width=Aspect,1
      ModifyGraph tick=3
      ModifyGraph mirror=0
      ModifyGraph nticks=10
      ModifyGraph minor=1
      ModifyGraph noLabel=2
      ModifyGraph fSize=9
      ModifyGraph standoff=0
      ModifyGraph tkLblRot(left)=90
      ModifyGraph btLen=3
      ModifyGraph tlOffset=-2
      SetAxis/A/R left
      ModifyGraph margin=3
      ModifyGraph swapXY=1
      RenameWindow #,Image3
      SetActiveSubwindow ##
   endif

   //Image 4
   if(NumImages >= 4)
      Display/W=(300,600,600,900)/HOST=#
      AppendImage/T ImageText_to_LUT40
      ModifyImage ImageText_to_LUT40 cindex= Spectre16bit
      ModifyGraph margin(left)=14,margin(bottom)=14,margin(top)=14, ↓
         margin(right)=14,width=Aspect,1
      ModifyGraph tick=3
      ModifyGraph mirror=0
      ModifyGraph nticks=10
      ModifyGraph minor=1
      ModifyGraph noLabel=2
      ModifyGraph fSize=9
      ModifyGraph standoff=0
      ModifyGraph tkLblRot(left)=90
      ModifyGraph btLen=3
```

```
        ModifyGraph tlOffset=-2
        SetAxis/A/R left
        ModifyGraph margin=3
        ModifyGraph swapXY=1
        RenameWindow #,Image4
        SetActiveSubwindow ##
    endif
EndMacro

Function SliderProc(ctrlName,sliderValue,event) : SliderControl
    String ctrlName
    Variable sliderValue
    Variable event   // bit field: bit 0: value set, 1: mouse down, ↓
        2: mouse up, 3: mouse moved
    wave Parametres

    if(event %& 0x1)   // bit 0, value set
        if(!cmpstr(ctrlName, "Loc1"))
            if(sliderValue <= Parametres[2])
                Parametres[2] = sliderValue
                Parametres[4] = sliderValue
            elseif(sliderValue >= Parametres[5])
                Parametres[5] = sliderValue
                Parametres[4] = sliderValue
            else
                Parametres[4] = sliderValue
            endif
        elseif(!cmpstr(ctrlName, "Loc2"))
            if(sliderValue <= Parametres[4])
                Parametres[4] = sliderValue
                Parametres[5] = sliderValue
            elseif(sliderValue >= Parametres[6])
                Parametres[6] = sliderValue
                Parametres[5] = sliderValue
            else
                Parametres[5] = sliderValue
            endif
        elseif(!cmpstr(ctrlName,"Loc3"))
            if(sliderValue <= Parametres[5])
                Parametres[5] = sliderValue
                Parametres[6] = sliderValue
            elseif(sliderValue >= Parametres[7])
```

```
            Parametres[7] = sliderValue
            Parametres[6] = sliderValue
        else
            Parametres[6] = sliderValue
        endif
    elseif(!cmpstr(ctrlName, "Loc4"))
        if(sliderValue <= Parametres[6])
            Parametres[6] = sliderValue
            Parametres[7] = sliderValue
        elseif(sliderValue >= Parametres[8])
            Parametres[8] = sliderValue
            Parametres[7] = sliderValue
        else
            Parametres[7] = sliderValue
        endif
    elseif(!cmpstr(ctrlName, "Loc5"))
        if(sliderValue <= Parametres[7])
            Parametres[7] = sliderValue
            Parametres[8] = sliderValue
        else
            Parametres[8] = sliderValue
        endif
    elseif(!cmpstr(ctrlName, "GrayLinLoc"))
        if(sliderValue >= Parametres[4])
            Parametres[2] = sliderValue
            Parametres[4] = sliderValue
        elseif(sliderValue >= Parametres[3])
            Parametres[3] = sliderValue
            Parametres[2] = sliderValue
        else
            Parametres[2] = sliderValue
        endif
    elseif(!cmpstr(ctrlName, "ShadeLeft"))
        if(sliderValue <= Parametres[2])
            Parametres[2] = sliderValue
            Parametres[3] = sliderValue
        elseif(sliderValue >= Parametres[9])
            Parametres[9] = sliderValue
            Parametres[3] = sliderValue
        else
            Parametres[3] = sliderValue
        endif
```

```
        elseif(!cmpstr(ctrlName, "ShadeRight"))
           if(sliderValue <= Parametres[3])
              Parametres[3] = sliderValue
              Parametres[9] = sliderValue
           else
              Parametres[9] = sliderValue
           endif
        elseif(!cmpstr(ctrlName, "GrayLinL"))
           Parametres[10] = sliderValue
        elseif(!cmpstr(ctrlName, "GrayLinR"))
           Parametres[11] = sliderValue
        elseif(!cmpstr(ctrlName, "GrayE"))
           Parametres[12] = sliderValue
        elseif(!cmpstr(ctrlName, "Purple"))
           Parametres[17] = 0.01*round(10^sliderValue*100)
        elseif(!cmpstr(ctrlName, "Gam"))
           Parametres[14] = 0.01*round(10^sliderValue*100)
        elseif(!cmpstr(ctrlName, "Light"))
           Parametres[15] = sliderValue
        endif
     endif

     MakeLut(Parametres[16])

     return 0
End

Function UpdateSlider(ctrlName,varNum,varStr,varName) : SetVariableControl
     String ctrlName
     Variable varNum
     String varStr
     String varName
     String tmp = ctrlName[3,strlen(ctrlName)-1]
     wave Parametres

     if(cmpstr(tmp, "Gam") != 0)
        Slider $tmp, value=varNum
     elseif(!cmpstr(tmp, "Gam"))
        Slider $tmp, value = log(varNum)
     endif

     MakeLut(Parametres[16])
```

```
End

Function LoadImage(ctrlName) : ButtonControl
    String ctrlName
    String fileFilters = "Image Files (*.txt):.txt;"
    Variable refnum
    wave Parametres
    String name = "ImageText_to_LUT"+ctrlName[strlen(ctrlName)-1]
    Open/D/R/F=fileFilters/M="Select the image" refnum
    LoadWave/G/M/D/N=$name/O S_fileName
    MakeLut(Parametres[16])
End

Function SaveLUT(ctrlName) : ButtonControl
    String ctrlName
    Variable refnum
    wave Parametres, DesiredColors, Spectre, Spectre_1, Spectre_2, ↓
        Spectre_3, Spectre_4
    Variable num = str2num(ctrlName[strlen(ctrlName)-1])
    if(num==1)
        Save/G/I/F Spectre_1 as "LUT1.lut"
        if(Parametres[16] == 1)
            Save/T/O Parametres, DesiredColors as "Parametres.txt"
        endif
    elseif(num==2)
        Save/G/I/F Spectre_2 as "LUT2.lut"
    elseif(num==3)
        Save/G/I/F Spectre_3 as "LUT3.lut"
    elseif(num==4)
        Save/G/I/F Spectre_4 as "LUT4.lut"
    elseif(num ==0)
        Save/G/I/F Spectre as "LUT_Globale.lut"
        Save/T/O Parametres as "Parametres.txt"
    endif
End

Function MakeLut(numImages)
    Variable numImages
    Initialisation(numImages)
    wave Spectre, Spectre_1, Spectre_2, Spectre_3, Spectre_4
    //l = left end                    r = right end
    //sl = end of shading left       sr = end of shading right
```

```
   //ll = end of linear grayscale region (left side)
   //1, 2, 3, 4 et 5  sont les positions ou il y a changement de ↓
      couleur de base
   Variable sl, sr, s1, s2, s3, s4, s5, ssl, ssr, sll
   Variable pl, pr, p1, p2, p3, p4, p5, psl, psr, pll
   Variable xl, xr, x1, x2, x3, x4, x5, xsl, xsr, xll
   Variable colorll, colorlr, colorr, speedgreen, gam, gam2, ↓
      numpoints, light
   wave Parametres, DesiredColors
//----------------------
   sl = 0;           sr = 1;
   sll = Parametres[2]/100
   ssl= Parametres[3]/100;
   s1 = Parametres[4]/100;       s2 = Parametres[5]/100; ↓
   s3 = Parametres[6]/100;       s4 = Parametres[7]/100; ↓
   s5 = Parametres[8]/100;
   ssr =Parametres[9]/100

   colorll = Parametres[10]
   colorlr = Parametres[11]
   colorr = Parametres[12]
   light = Parametres[15]

   speedgreen = Parametres[13]
   gam=Parametres[14]
   gam2 = Parametres[17]
//----------------------
   numpoints = DimSize(Spectre, 0)-1
   pl = 0;       pr =  numpoints
   pll = round(sll*numpoints)
   psl = round(ssl*numpoints)
   p1 = round(s1*numpoints);     p2 = round(s2*numpoints); ↓
   p3 = round(s3*numpoints);     p4 = round(s4*numpoints); ↓
   p5 = round(s5*numpoints)
   psr = round(ssr*numpoints)

   xl = DimOffset(Spectre, 0) + pl *DimDelta(Spectre,0);
   xr =  DimOffset(Spectre, 0) + pr *DimDelta(Spectre,0);
   xll = DimOffset(Spectre, 0) + pll *DimDelta(Spectre,0);
   xsl = DimOffset(Spectre, 0) + psl *DimDelta(Spectre,0);
   x1 = DimOffset(Spectre, 0) + p1 *DimDelta(Spectre,0);
   x2 = DimOffset(Spectre, 0) + p2 *DimDelta(Spectre,0);
```

```
   x3 = DimOffset(Spectre, 0) + p3 *DimDelta(Spectre,0);
   x4 = DimOffset(Spectre, 0) + p4 *DimDelta(Spectre,0);
   x5 = DimOffset(Spectre, 0) + p5 *DimDelta(Spectre,0);
   xsr = DimOffset(Spectre, 0) + psr *DimDelta(Spectre,0);

//-----------------------
   Duplicate/O DesiredColors, DesiredColors01
   DesiredColors01 /= 255;

   Spectre[pl, pll][] = (colorll^(1/gam2) - (p-pl)/(pll-pl) * ↓
      (colorll^(1/gam2)-colorlr^(1/gam2)))^gam2
   Spectre[pll+1, p1-1][] =   Spectre[pll][q] - (p-pll)/(p1-pll)* ↓
      (Spectre[pll][q]-DesiredColors01[0][q])
   Spectre[p1, p2-1][] =  DesiredColors01[0][q] - (p-p1)/(p2-p1)* ↓
      (DesiredColors01[0][q]-DesiredColors01[1][q])
   Spectre[p2, p3-1][] =  DesiredColors01[1][q] - (p-p2)/(p3-p2)* ↓
      (DesiredColors01[1][q]-DesiredColors01[2][q])
   Spectre[p3, p4-1][] =  DesiredColors01[2][q] - (p-p3)/(p4-p3)* ↓
      (DesiredColors01[2][q]-DesiredColors01[3][q])
   Spectre[p4, p5-1][] =  DesiredColors01[3][q] - (p-p4)/(p5-p4)* ↓
      (DesiredColors01[3][q]-DesiredColors01[4][q])
   if(p5 != pr)
      Spectre[p5, pr][] =  DesiredColors01[4][q] - (p-p5)/(pr-p5)* ↓
         (DesiredColors01[4][q]-colorr)
   else
      Spectre[pr][] = DesiredColors01[4][q]
   endif

   //if(pll<=p1 && p1<=p2 && p2<=p3 && p3<=p4 && p4<=p5 && p5<=pr)
   ApplyGamma(Spectre, gam, pll, p1)//Pour avoir des transitions de ↓
      couleurs plus sympathiques
   ApplyGamma(Spectre, gam, p1, p2)
   ApplyGamma(Spectre, gam, p2, p3)
   ApplyGamma(Spectre, gam, p3, p4)
   ApplyGamma(Spectre, gam, p4, p5)
   ApplyGamma(Spectre, gam, p5, pr)
   //endif

   Duplicate/O Spectre, Lumiere
   Redimension/N=(-1) Lumiere

   //Pour régler un peu la lumière partout
```

```
Lumiere[pl, pll]      =     1
Lumiere[pll+1, psl] =     Lumiere[pll] +(light-Lumiere[pll])* ↓
    (p-pll-1)/(psl-pll-1)
Lumiere[psl, psr]    =     light
Lumiere[psr, pr]     =     psr >= pr ? light : light-(light-colorr)* ↓
    (p-psr)/(pr-psr)

//Pour avoir tout entre 0 et 255
Spectre[][] = round(Spectre[p][q]*Lumiere[p]*255)
Duplicate/O Spectre, Spectre16bit
//Pour avoir tout entre 0 et 65535
Spectre16bit[][] = round(Spectre[p][q]*65535/255)

//Génération des spectre pour les image (dépendant de ↓
    l'étendue maximale)
wave ImageLimits, temp, temp_2
Duplicate/O Spectre, temp
Redimension/N=-1 temp

Variable i=0
if(numImages >= 1)
   Duplicate/O Spectre_1, temp_
   Redimension/N=-1  temp_
   for(i=0; i<=2; i+=1)
      temp[] = Spectre[p][i]
      Interpolate2/T=1/N=(numpnts(temp))/I=3/Y=temp_ temp
      Spectre_1[][i] = temp_[p]
   endfor
endif
if(numImages >= 2)
   Duplicate/O Spectre_2, temp_
   Redimension/N=-1  temp_
   for(i=0; i<=2; i+=1)
      temp[] = Spectre[p][i]
      Interpolate2/T=1/N=(numpnts(temp))/I=3/Y=temp_ temp
      Spectre_2[][i] = temp_[p]
   endfor
endif
if(numImages >= 3)
   Duplicate/O Spectre_3, temp_
   Redimension/N=-1  temp_
   for(i=0; i<=2; i+=1)
```

```
            temp[] = Spectre[p][i]
            Interpolate2/T=1/N=(numpnts(temp))/I=3/Y=temp_ temp
            Spectre_3[][i] = temp_[p]
        endfor
    endif
    if(numImages == 4)
        Duplicate/O Spectre_4, temp_
        Redimension/N=-1  temp_
        for(i=0; i<=2; i+=1)
            temp[] = Spectre[p][i]
            Interpolate2/T=1/N=(numpnts(temp))/I=3/Y=temp_ temp
            Spectre_4[][i] = temp_[p]
        endfor
    endif

End

Function ApplyGamma(waveSpectre, gammaValue, xstart, xend)
    wave waveSpectre
    variable gammaValue, xstart, xend

    variable valMin, valMax
    duplicate/R=[xstart, xend]/O/FREE waveSpectre, wave0
    redimension/N=-1 wave0

    wave0 = waveSpectre[xstart+p][0]
    valMin = wavemin(wave0)
    valMax = wavemax(wave0)
    if(valMin != valMax)
        wave0 = (((wave0[p]-valMin)/(valMax-valMin))^gammaValue)* ↓
            (valMax-valMin) + valMin;
    endif
    waveSpectre[xstart, xend][0] = wave0[p-xstart]

    wave0 = waveSpectre[xstart+p][1]
    valMin = wavemin(wave0)
    valMax = wavemax(wave0)
    if(valMin != valMax)
        wave0 = (((wave0[p]-valMin)/(valMax-valMin))^gammaValue)* ↓
            (valMax-valMin) + valMin;
    endif
    waveSpectre[xstart, xend][1] = wave0[p-xstart]
```

```
    wave0 = waveSpectre[xstart+p][2]
    valMin = wavemin(wave0)
    valMax = wavemax(wave0)
    if(valMin != valMax)
        wave0 = (((wave0[p]-valMin)/(valMax-valMin))^gammaValue)* ↓
            (valMax-valMin) + valMin;
    endif
    waveSpectre[xstart, xend][2] = wave0[p-xstart]
End
```

Bibliography

[1] E. Schrödinger, "Quantisierung als Eigenwertproblem", Ann. Phys.-Berlin **384**, 361 (1926).

[2] J. Klein, A. Léger, M. Belin, D. Défourneau and M. J. L. Sangster, "Inelastic-Electron-Tunneling Spectroscopy of Metal-Insulator-Metal Junctions", Phys. Rev. B **7**, 2336 (1973).

[3] J. Lambe and R. C. Jaklevic, "Molecular Vibration Spectra by Inelastic Electron Tunneling", Phys. Rev. **165**, 821 (1968).

[4] S. C. Wang and G. Ehrlich, "Self-adsorption sites on a close-packed surface: Ir on Ir(111)", Phys. Rev. Lett. **62**, 2297 (1989).

[5] E. W. Müller, "Resolution of the Atomic Structure of a Metal Surface by the Field Ion Microscope", J. Appl. Phys. **27**, 474 (1956).

[6] E. W. Müller, "Feldemission", Ergeb. Exakten Naturwiss. **27**, 290 (1953).

[7] G. Antczak and G. Ehrlich, *Surface Diffusion: Metals, Metal Atoms, and Clusters*, Cambridge University Press (2010).

[8] R. Young, J. Ward and F. Scire, "Observation of Metal-Vacuum-Metal Tunneling, Field Emission, and the Transition Region", Phys. Rev. Lett. **27**, 922 (1971).

[9] R. D. Young, "Surface microtopography", Pysics Today **24**, 42 (1971).

[10] R. Young, J. Ward and F. Scire, "The Topografiner: An Instrument for Measuring Surface Microtopography", Rev. Sci. Instrum. **43**, 999 (1972).

[11] R. H. Fowler and L. Nordheim, "Electron Emission in Intense Electric Fields", P. Roy. Soc. A-Math. Phy. **119**, 173 (1928).

[12] G. Binnig and H. Rohrer, "Scanning tunneling microscopy", Helv. Phys. Acta **55**, 726 (1982).

[13] G. Binnig, H. Rohrer, C. Gerber and E. Weibel, "Tunneling through a controllable vacuum gap", Appl. Phys. Lett. **40**, 178 (1982).

[14] G. Binnig, H. Rohrer, C. Gerber and E. Weibel, "Surface Studies by Scanning Tunneling Microscopy", Phys. Rev. Lett. **49**, 57 (1982).

[15] G. Binnig and H. Rohrer, "Scanning tunneling microscopy", Surf. Sci. **126**, 236 (1983).

[16] G. Binnig and H. Rohrer, "Scanning tunneling microscopy—from birth to adolescence", Rev. Mod. Phys. **59**, 615 (1987).

[17] J. Tersoff and D. R. Hamann, "Theory and Application for the Scanning Tunneling Microscope", Phys. Rev. Lett. **50**, 1998 (1983).

[18] J. Tersoff and D. R. Hamann, "Theory of the scanning tunneling microscope", Phys. Rev. B **31**, 805 (1985).

[19] J. Tersoff, "Method for the calculation of scanning tunneling microscope images and spectra", Phys. Rev. B **40**, 11990 (1989).

[20] N. D. Lang, "Theory of Single-Atom lmaging in the Scanning Tunneling Microscope", Comments Cond. Mat. Phys. **14**, 253 (1989).

[21] N. D. Lang, "Theory of Single-Atom Imaging in the Scanning Tunneling Microscope", Phys. Rev. Lett. **56**, 1164 (1986).

[22] N. D. Lang, "Spectroscopy of single atoms in the scanning tunneling microscope", Phys. Rev. B **34**, 5947 (1986).

[23] F. Besenbacher, "Scanning tunnelling microscopy studies of metal surfaces", Rep. Prog. Phys. **59**, 1737 (1996).

[24] T. E. Feuchtwang and P. H. Cutler, "Tunneling and Scanning Tunnel Microscopy: a Critical Review", Phys. Scripta **35**, 132 (1987).

[25] G. Meyer, L. Bartels, S. Zöphel and K. Rieder, "Lateral manipulation of adatoms and native substrate atoms with the low-temperature scanning tunneling microscope", Appl. Phys. A **68**, 125 (1999).

[26] M. F. Crommie, C. P. Lutz and D. M. Eigler, "Confinement of Electrons to Quantum Corrals on a Metal Surface", Science **262**, 218 (1993).

[27] L. J. Lauhon and W. Ho, "Single-molecule vibrational spectroscopy and microscopy: CO on Cu(001) and Cu(110)", Phys. Rev. B **60**, R8525 (1999).

[28] B. C. Stipe, M. A. Rezaei and W. Ho, "Single-Molecule Vibrational Spectroscopy and Microscopy", Science **280**, 1732 (1998).

[29] J. Li, W.-D. Schneider, R. Berndt and S. Crampin, "Electron Confinement to Nanoscale Ag Islands on Ag(111): A Quantitative Study", Phys. Rev. Lett. **80**, 3332 (1998).

[30] M. F. Crommie, C. P. Lutz and D. M. Eigler, "Imaging standing waves in a two-dimensional electron gas", Nature **363**, 524 (1993).

[31] L. Bartels, G. Meyer and K.-H. Rieder, "Controlled vertical manipulation of single CO molecules with the scanning tunneling microscope: A route to chemical contrast", Appl. Phys. Lett. **71**, 213 (1997).

[32] L. Pleth Nielsen, F. Besenbacher, I. Stensgaard, E. Laegsgaard, C. Engdahl, P. Stoltze, K. W. Jacobsen and J. K. Nørskov, "Initial growth of Au on Ni(110): Surface alloying of immiscible metals", Phys. Rev. Lett. **71**, 754 (1993).

[33] H. Brune, J. Wintterlin, G. Ertl and R. J. Behm, "Direct Imaging of Adsorption Sites and Local Electronic Bond Effects on a Metal Surface: C/Al(111)", Europhys. Lett. **13**, 123 (1990).

[34] R. Temirov, S. Soubatch, O. Neucheva, A. C. Lassise and F. S. Tautz, "A novel method achieving ultra-high geometrical resolution in scanning tunnelling microscopy", New J. Phys. **10**, 053012 (2008).

[35] M. Kleiber, M. Bode, R. Ravlić and R. Wiesendanger, "Topology-Induced Spin Frustrations at the Cr(001) Surface Studied by Spin-Polarized Scanning Tunneling Spectroscopy", Phys. Rev. Lett. **85**, 4606 (2000).

[36] R. Wiesendanger, "Spin mapping at the nanoscale and atomic scale", Rev. Mod. Phys. **81**, 1495 (2009).

[37] F. D. Natterer, K. Yang, W. Paul, P. Willke, T. Choi, T. Greber, A. J. Heinrich and C. P. Lutz, "Reading and Writing Single-Atom Magnets", Nature **543**, 226 (2017).

[38] S. Baumann, W. Paul, T. Choi, C. P. Lutz, A. Ardavan and A. J. Heinrich, "Electron paramagnetic resonance of individual atoms on a surface", Science **350**, 417 (2015).

[39] H. Brune, "In the wake of collision", Science **350**, 1321 (2015).

[40] H. Brune, *Adsorbed Layers on Surfaces. Part 1: Adsorption on Surfaces and Surface Diffusion of Adsorbates*, chap. Metals on metals, pp. 217–258, Springer Berlin Heidelberg, Berlin, Heidelberg (2001).

[41] C. J. Chen, *Introduction to Scanning Tunneling Microscopy*, Oxford University Press, United Kingdom (1993).

[42] B. Voigtländer, *Scanning Probe Microscopy - Atomic Force Microscopy and Scanning Tunneling Microscopy*, Springer Berlin Heidelberg, Berlin, Heidelberg (2015).

[43] J. Bardeen, "Tunnelling from a Many-Particle Point of View", Phys. Rev. Lett. **6**, 57 (1961).

[44] A. Selloni, P. Carnevali, E. Tosatti and C. D. Chen, "Voltage-dependent scanning-tunneling microscopy of a crystal surface: Graphite", Phys. Rev. B **31**, 2602 (1985).

[45] A. Malashevich, E. I. Altman and S. Ismail-Beigi, "Imaging the buried MgO/Ag interface: Formation mechanism of the STM contrast", Phys. Rev. B **90**, 165426 (2014).

[46] M. Ternes, "Scanning Tunneling Spectroscopy at the Single Atom Scale", Ph.D. thesis, Ecole Polytechnique Fédérale de Lausanne, Faculté des Sciences de Base (2006).

[47] A. Baratoff and B. N. J. Persson, "Theory of the local tunneling spectrum of a vibrating adsorbate", J. Vac. Sci. Technol. A **6**, 331 (1988).

[48] I. G. Rau, S. Baumann, S. Rusponi, F. Donati, S. Stepanow, L. Gragnaniello, J. Dreiser, C. Piamonteze, F. Nolting, S. Gangopadhyay, O. R. Albertini, R. M. Macfarlane, C. P. Lutz, B. A. Jones, P. Gambardella, A. J. Heinrich and H. Brune, "Reaching the magnetic anisotropy limit of a $3d$ metal atom", Science **344**, 988 (2014).

[49] S. Li, A. Yu, F. Toledo, Z. Han, H. Wang, H. Y. He, R. Wu and W. Ho, "Rotational and Vibrational Excitations of a Hydrogen Molecule Trapped within a Nanocavity of Tunable Dimension", Phys. Rev. Lett. **111**, 146102 (2013).

[50] F. Donati, Q. Dubout, G. Autès, F. Patthey, F. Calleja, P. Gambardella, O. V. Yazyev and H. Brune, "Magnetic Moment and Anisotropy of Individual Co Atoms on Graphene", Phys. Rev. Lett. **111**, 236801 (2013).

[51] A. Halbritter, P. Makk, S. Csonka and G. Mihály, "Huge negative differential conductance in Au-H_2 molecular nanojunctions", Phys. Rev. B **77**, 075402 (2008).

[52] J. A. Gupta, C. P. Lutz, A. J. Heinrich and D. M. Eigler, "Strongly coverage-dependent excitations of adsorbed molecular hydrogen", Phys. Rev. B **71**, 115416 (2005).

[53] S. Schintke, S. Messerli, M. Pivetta, F. Patthey, L. Libioulle, M. Stengel, A. De Vita and W.-D. Schneider, "Insulator at the Ultrathin Limit: MgO on Ag(001)", Phys. Rev. Lett. **87**, 276801 (2001).

[54] H.-C. Ploigt, C. Brun, M. Pivetta, F. Patthey and W.-D. Schneider, "Local work function changes determined by field emission resonances: NaCl/Ag(100)", Phys. Rev. B **76**, 195404 (2007).

[55] v. W. Nernst and F. A. Lindemann, "Untersuchungen über die spezifische Wärme bei tiefen Temperaturen. V.", Preuss. Akad. d. Wiss **22**, 494 (1911).

[56] A. Eucken, "Die molekularwarme des wasserstoffs bei tiefen temperaturen", Preuss. Akad. d. Wiss **6**, 141 (1912).

[57] This specific resource is available at the following ULR: http://www.biodiversitylibrary.org/page/40736505#page/165/mode/1up.

[58] D. M. Dennison, "Wave Mechanics and Rotation of Homopolar Molecules", Nature **119**, 316 (1927).

[59] D. M. Dennison, "A Note on the Specific Heat of the Hydrogen Molecule", Proc. R. Soc. A **115**, 483 (1927).

[60] A. Farkas, *Orthohydrogen, Parahydrogen and Heavy Hydrogen*, The Cambridge Series of Physical Chemistry, Cambridge University Press (1935).

[61] F. Reif, *Fundamentals of STATISTICAL AND THERMAL PHYSICS*, McGraw-Hill Book (1985).

[62] K. Fukutani and T. Sugimoto, "Physisorption and ortho–para conversion of molecular hydrogen on solid surfaces", Progr. Surf. Sci. **88**, 279 (2013).

[63] E. Ilisca, "Ortho-para conversion of hydrogen molecules physisorbed on surfaces", Prog. Surf. Sci. **41**, 217 (1992).

[64] P. Avouris, D. Schmeisser and J. E. Demuth, "Observation of Rotational excitations of H_2 Adsorbed on Ag Surfaces", Phys. Rev. Lett. **48**, 199 (1982).

[65] S. Andersson and J. Harris, "Observation of Rotational Transitions for H_2, D_2, and HD Adsorbed on Cu(100)", Phys. Rev. Lett. **48**, 545 (1982).

[66] K. Svensson and S. Andersson, "Fast *Ortho-Para* conversion of H_2 adsorbed at copper surface step atoms", Phys. Rev. Lett. **98**, 096105 (2007).

[67] S. Andersson and K. Svensson, "Electron-Induced Desorption of Physisorbed H_2 via Resonance Vibrational Excitation", Phys. Rev. Lett. **102**, 156104 (2009).

[68] F. D. Natterer, F. Patthey and H. Brune, "Distinction of Nuclear Spin States with the Scanning Tunneling Microscope", Phys. Rev. Lett. **111**, 175303 (2013).

[69] F. D. Natterer, F. Patthey and H. Brune, "Resonant-Enhanced Spectroscopy of Molecular Rotations with a Scanning Tunneling Microscope", ACS Nano **8**, 7099 (2014).

[70] T. Sugimoto and K. Fukutani, "Effects of Rotational-Symmetry Breaking on Physisorption of Ortho- and Para-H_2 on Ag(111)", Phys. Rev. Lett. **112**, 146101 (2014).

[71] M. Sicot, O. Kurnosikov, O. A. O. Adam, H. J. M. Swagten and B. Koopmans, "Stm-induced desorption of hydrogen from Co nanoislands", Phys. Rev. B **77**, 035417 (2008).

[72] A. J. Therrien, A. Pronschinske, C. J. Murphy, E. A. Lewis, M. L. Liriano, M. D. Marcinkowski and E. C. H. Sykes, "Collective effects in physisorbed molecular hydrogen on Ni/Au(111)", Phys. Rev. B **92**, 161407 (2015).

[73] J. Seguin and J. Suzanne, "A LEED study of physisorbed hydrogen on graphite", Surf. Sci. **118**, L241 (1982).

[74] M. Nielsen, J. P. McTague and W. Ellenson, "Adsorbed Layers of D_2, H_2, O_2, and ^{3}He on Graphite studied by Neutron Scattering", J. Phys. Colloques **38**, C4–10 (1977).

Bibliography

[75] V. L. P. Frank, H. J. Lauter and P. Leiderer, "Phonons in the Commensurate Monolayer of D_2 on graphite", Phys. Rev. Lett. **61**, 436 (1988).

[76] R. Palmer and R. Willis, "Rotational states of physisorbed hydrogen on graphite", Surf. Sci. **179**, L1 (1987).

[77] F. Brunet, R. Schaub, S. Fédrigo, R. Monot, J. Buttet and W. Harbich, "Rare gases physisorbed on Pt(111): a low-temperature STM investigation", Surf. Sci. **512**, 201 (2002).

[78] A. J. Heinrich, J. A. Gupta, C. P. Lutz and D. M. Eigler, "Single-Atom Spin-Flip Spectroscopy", Science **306**, 466 (2004).

[79] A. F. Otte, M. Ternes, K. von Bergmann, S. Loth, H. Brune, C. P. Lutz, C. F. Hirjibehedin and A. J. Heinrich, "The role of magnetic anisotropy in the Kondo effect", Nat. Phys. **4**, 847 (2008).

[80] F. Donati, S. Rusponi, S. Stepanow, C. Wäckerlin, A. Singha, L. Persichetti, R. Baltic, K. Diller, F. Patthey, E. Fernandes, J. Dreiser, Ž. Šljivančanin, K. Kummer, C. Nistor, P. Gambardella and H. Brune, "Magnetic remanence in single atoms", Science **352**, 318 (2016).

[81] W. Paul, K. Yang, S. Baumann, N. Romming, T. Choi, C. P. Lutz and A. J. Heinrich, "Control of the millisecond spin lifetime of an electrically probed atom", Nat. Phys. **13**, 403 (2017).

[82] J. Repp, G. Meyer, F. E. Olsson and M. Persson, "Controlling the Charge State of Individual Gold Adatoms", Science **305**, 493 (2004).

[83] F. E. Olsson, S. Paavilainen, M. Persson, J. Repp and G. Meyer, "Multiple Charge States of Ag Atoms on Ultrathin NaCl Films", Phys. Rev. Lett. **98**, 176803 (2007).

[84] W. Steurer, J. Repp, L. Gross, I. Scivetti, M. Persson and G. Meyer, "Manipulation of the Charge State of Single Au Atoms on Insulating Multilayer Films", Phys. Rev. Lett. **114**, 036801 (2015).

[85] A. S. Wörz, K. Judai, S. Abbet, J. M. Antonietti, U. Heiz, A. D. Vitto, L. Giordano and G. Pacchioni, "Chemistry on single atoms: key factors for the acetylene trimerization on MgO-supported Rh, Pd, and Ag atoms", Chem. Phys. Lett. **399**, 266 (2004).

[86] C. Hübner, B. Baxevanis, A. A. Khajetoorians and D. Pfannkuche, "Symmetry effects on the spin switching of adatoms", Physical Review B **90**, 155134 (2014).

[87] J. Repp, G. Meyer, K. H. Rieder and P. Hyldgaard, "Site Determination and Thermally Assisted Tunneling in Homogenous Nucleation", Phys. Rev. Lett. **91**, 206102 (2003).

[88] T. Eelbo, M. Waśniowska, M. Gyamfi, S. Forti, U. Starke and R. Wiesendanger, "Influence of the degree of decoupling of graphene on the properties of transition metal adatoms", Phys. Rev. B **87**, 205443 (2013).

[89] K. Honkala and H. Häkkinen, "Au Adsorption on Regular and Defected Thin MgO(100) Films Supported by Mo", J. Phys. Chem. C **111**, 4319 (2007).

[90] G. Pacchioni, L. Giordano and M. Baistrocchi, "Charging of Metal Atoms on Ultrathin MgO/Mo(100) Films", Phys. Rev. Lett. **94**, 226104 (2005).

[91] M. Yulikov, M. Sterrer, M. Heyde, H.-P. Rust, T. Risse, H.-J. Freund, G. Pacchioni and A. Scagnelli, "Binding of Single Gold Atoms on Thin MgO(001) Films", Phys. Rev. Lett. **96**, 146804 (2006).

[92] E. Fernandes, F. Donati, F. Patthey, S. Stavrić, Ž. Šljivančanin and H. Brune, "Adsorption sites of individual metal atoms on ultrathin MgO(100) films", Phys. Rev. B **96**, 045419 (2017).

[93] J. Pal, M. Smerieri, E. Celasco, L. Savio, L. Vattuone and M. Rocca, "Morphology of Monolayer MgO Films on Ag(100): Switching from Corrugated Islands to Extended Flat Terraces", Phys. Rev. Lett. **112**, 126102 (2014).

[94] J. Pal, M. Smerieri, E. Celasco, L. Savio, L. Vattuone, R. Ferrando, S. Tosoni, L. Giordano, G. Pacchioni and M. Rocca, "How Growing Conditions and Interfacial Oxygen Affect the Final Morphology of MgO/Ag(100) Films", J. Phys. Chem. C **118**, 26091 (2014).

[95] J. Wollschläger, J. Viernow, C. Tegenkamp, D. Erdös, K. M. Schröder and H. Pfnür, "Stoichiometry and morphology of MgO films grown reactively on Ag(100)", Appl. Surf. Sci. **142**, 129 (1999).

[96] S. Baumann, I. G. Rau, S. Loth, C. P. Lutz and A. J. Heinrich, "Measuring the Three-Dimensional Structure of Ultrathin Insulating Films at the Atomic Scale", ACS Nano **8**, 1739 (2014).

[97] M. Sterrer, T. Risse, M. Heyde, H.-P. Rust and H.-J. Freund, "Crossover from Three-Dimensional to Two-Dimensional Geometries of Au Nanostructures on Thin MgO(001) Films: A Confirmation of Theoretical Predictions", Phys. Rev. Lett. **98**, 206103 (2007).

[98] N. Lopez and S. Valeri, "MgO/Ag(100) interface structure and STM images from first principles", Phys. Rev. B **70**, 125428 (2004).

[99] H. Y. T. Chen and G. Pacchioni, "Properties of two-dimensional insulators: a DFT study of Co adsorption on NaCl and MgO ultrathin films", Phys. Chem. Chem. Phys. **16**, 21838 (2014).

[100] S. Stankic, M. Sterrer, P. Hofmann, J. Bernardi, O. Diwald and E. Knözinger, "Novel Optical Surface Properties of Ca_2^+-Doped MgO Nanocrystals", Nano Lett. **5**, 1889 (2005).

[101] P. W. Tasker, E. Colbourn and W. MacKrodt, "Segregation of Isovalent Impurity Cations at the Surfaces of MgO and CaO", J. Am. Ceram. Soc. **68**, 74 (1985).

Bibliography

[102] R. C. McCune and P. Wynblatt, "Calcium Segregation to a Magnesium Oxide (100) Surface", J. Am. Ceram. Soc. **66**, 111 (1983).

[103] P. Hofmann, "Herstellung und Charakterisierung thermish stabiler CaO-Oberflächen auf hochdispersen MgO/CaO-Mischoxiden", Ph.D. thesis, Technischen Universität Wien (1997).

[104] F. Natterer, F. Patthey and H. Brune, "Quantifying residual hydrogen adsorption in low-temperature STMs", Surf. Sci. **615**, 80 (2013).

[105] D. Z. Gao, M. B. Watkins and A. L. Shluger, "Transient Mobility Mechanisms of Deposited Metal Atoms on Insulating Surfaces: Pd on MgO(100)", J. Phys. Chem. C **116**, 14471 (2012).

[106] O. Bünermann, H. Jiang, Y. Dorenkamp, A. Kandratsenka, S. Janke, D. J. Auerbach and A. M. Wodtke, "Observation of electron-hole pair excitation in hydrogen atom-surface scattering reveals the mechanism of adsorption", Science **350**, 1346 (2015).

[107] M. Smerieri, J. Pal, L. Savio, L. Vattuone, R. Ferrando, S. Tosoni, L. Giordano, G. Pacchioni and M. Rocca, "Spontaneous Oxidation of Ni Nanoclusters on MgO Monolayers Induced by Segregation of Interfacial Oxygen", J. Phys. Chem. Lett. **6**, 3104 (2015).

[108] S. Baumann, "Investigation of the unusual magnetic properties of Fe and Co on MgO with high spatial, energy and temporal resolution", Ph.D. thesis, University of Basel, Faculty of Science (2015).

[109] S. Baumann, F. Donati, S. Stepanow, S. Rusponi, W. Paul, S. Gangopadhyay, I. G. Rau, G. E. Pacchioni, L. Gragnaniello, M. Pivetta, J. Dreiser, C. Piamonteze, C. P. Lutz, R. M. Macfarlane, B. A. Jones, P. Gambardella, A. J. Heinrich and H. Brune, "Origin of Perpendicular Magnetic Anisotropy and Large Orbital Moment in Fe Atoms on MgO", Phys. Rev. Lett. **115**, 237202 (2015).

[110] B. D. Yu, "*Ab initio* study of the adsorption of Fe atoms on a defective MgO(001) surface: Blind adsorption", Phys. Rev. B **71**, 193403 (2005).

[111] M. Sterrer, T. Risse, U. Martinez Pozzoni, L. Giordano, M. Heyde, H.-P. Rust, G. Pacchioni and H.-J. Freund, "Control of the Charge State of Metal Atoms on Thin MgO Films", Phys. Rev. Lett. **98**, 096107 (2007).

[112] V. Simic-Milosevic, M. Heyde, N. Nilius, T. König, H.-P. Rust, M. Sterrer, T. Risse, H.-J. Freund, L. Giordano and G. Pacchioni, "Au dimers on Thin MgO(001) Films: Flat and Charged or Upright and Neutral?", J. Am. Chem. Soc. **130**, 7814 (2008).

[113] N. Knorr, H. Brune, M. Epple, A. Hirstein, M. A. Schneider and K. Kern, "Long-range adsorbate interactions mediated by a two-dimensional electron gas", Phys. Rev. B **65**, 115420 (2002).

[114] G. Pacchioni and H. Freund, "Electron Transfer at Oxide Surfaces. The MgO Paradigm: from Defects to Ultrathin Films", Chemical Reviews **113**, 4035 (2013).

[115] Aparajita Singha, private communication. HoCo dimers show an inelastic step at an energy of 19.7 ± 0.2 meV.

[116] V. Zhdanov, "Arrhenius parameters for rate processes on solid surfaces", Surf. Sci. Rep. **12**, 185 (1991).

[117] F. Silly, M. Pivetta, M. Ternes, F. Patthey, J. P. Pelz and W.-D. Schneider, "Coverage-dependent self-organization: from individual adatoms to adatom superlattices", New J. Phys. **6**, 1 (2004).

[118] H. Brune, "Microscopic view of epitaxial metal growth: nucleation and aggregation", Surf. Sci. Rep. **31**, 125 (1998).

[119] David Z. Gao, private communication. In presence of multiple local minimas, the transient mobility would not select the most favorable adsorption site, but better populate them all.

[120] S. Homma, K. Okada and H. Matsuda, "Theory of Rotational Excitations in Solid Ortho-Hydrogen", Prog. Theor. Phys. **38**, 767 (1967).

[121] I. F. Silvera, "The solid molecular hydrogens in the condensed phase: Fundamentals and static properties", Rev. Mod. Phys. **52**, 393 (1980).

[122] A. J. Berlinsky and A. B. Harris, "Two-Libron Spectrum of Solid H_2 and D_2", Phys. Rev. B **4**, 2808 (1971).

[123] H. Stein, H. Stiller and R. Stockmeyer, "Phonons, Librons, and the Rotational State J = 1 in HCP and FCC Solid Hydrogen by Neutron Spectroscopy", J. Chem. Phys. **57**, 1726 (1972).

[124] C. F. Coll, A. B. Harris and A. J. Berlinsky, "Observation of Libron-Libron Interactions in Solid Hydrogen", Phys. Rev. Lett. **25**, 858 (1970).

[125] W. N. Hardy, I. F. Silvera and J. P. McTague, "Libron Spectra of Oriented Crystals of Paradeuterium and Orthohydrogen in the Ordered State", Phys. Rev. Lett. **26**, 127 (1971).

[126] B. N. J. Persson, "Monte Carlo calculations of adsorbate structures and the role of the vibrational entropy in phase transitions at surfaces", Phys. Rev. B **40**, 7115 (1989).

[127] A. Grossmann, W. Erley and H. Ibach, "Entropy-controlled site occupation of CO adsorbed on Ni(100)", Appl. Phys. A **57**, 499 (1993).

[128] A. Grossmann, W. Erley and H. Ibach, "Occupation of adsorption sites controlled by phonon entropy", Phys. Rev. Lett. **71**, 2078 (1993).

[129] H. Ibach, *Physics of Surfaces and Interfaces*, Springer-Verlag Berlin Heidelberg (2006).

Bibliography

[130] F. James, *Statistical Methods in Experimental Physics*, World Scientific Publishing Co. Pte. Ldt., 2nd ed. (2014).

[131] Wayne Rasband, National Institutes of Health, https://imagej.nih.gov/ij/.

[132] Igor Pro software is edited and sold by Wavemetrics compagny, https://www.wavemetrics.com/.

Curriculum Vitae

Edgar Fernandes
Rue Centrale 26
1022 Chavannes-
    près-Renens

Phone : +41 79 8255227
E-mail : `fernandes_edgar@hotmail.com`
Nationality: Portuguese, Swiss

Education

2013–2017	**Research and teaching assistant at the Laboratory of Nanostructures at Surfaces** Ecole Polytechnique Fédérale de Lausanne
2011–2013	**Master degree in Physics** Ecole Polytechnique Fédérale de Lausanne
2006–2013	**Bachelor degree in Physics** Ecole Polytechnique Fédérale de Lausanne

Professional experience

2017 (3 months)	**Scientific collaborator** Ecole Polytechnique Fédérale de Lausanne

Publications

E. Fernandes, F. Donati, F. Patthey, S. Stavrić, Ž. Šljivančanin and H. Brune, "Adsorption sites of individual metal atoms on ultrathin MgO(100) films", Phys. Rev. B **96**, 045419 (2017).

F. Donati, S. Rusponi, S. Stepanow, C. Wäckerlin, A. Singha, L. Persichetti, R. Baltic, K. Diller, F. Patthey, **E. Fernandes**, J. Dreiser, Ž. Šljivančanin, K. Kummer, C. Nistor, P. Gambardella and H. Brune, "Magnetic remanence in single atoms", Science **352**, 318 (2016).

M. Pivetta, G. E. Pacchioni, **E. Fernandes** and H. Brune, "Temperature-dependent self-assembly of NC–Ph$_5$–CN molecules on Cu(111)", J. Chem. Phys **142**, 101928 (2015).

Teaching

Lab work assistant
Travaux pratiques de physique II.
Supervision up to four groups of two students on historical experiments related with the establishment of modern theories of physics. These cover electromagnetism, solid state physics and thermodynamics.

Awards and distinctions

Trends in NanoTechnology 2016   Best Poster Prizes – presented by Ph.D. Students
"Experimental Determination of the Adsorption Sites of Individual Metal Atoms on MgO(100) Thin Films"

SAOG Poster Prize 2015   1st Poster Prize
"Rotational excitation spectroscopy of homonuclear diatomic molecules via STM"